CRANFIELD UNIVERSITY

WEI MA

FRACTURE TOUGHNESS CHARACTERIZATION OF THIN Ti/SiC COMPOSITES

SCHOOL OF ENGINEERING

MSc THESIS
Academic Year: 2010 - 2011

Supervisor: Prof. Rade Vignjevic
December 2011

CRANFIELD UNIVERSITY

SCHOOL OF ENGINEERING

MSc THESIS

Academic Year 2010 - 2011

Wei Ma

FRACTURE TOUGHNESS CHARACTERIZATION OF THIN Ti/SiC COMPOSITES

Supervisor: Prof. Rade Vignjevic

December 2011

ABSTRACT

Titanium based alloys reinforced uniaxially with silicon carbide fibres (Ti/SiC) are advanced and innovative materials for aerospace vehicles. To avoid potential problems, these new materials should be extensively tested and analyzed before application.

This research focuses on experimental fracture toughness study on 0.5 mm thick Ti/SiC composite materials for aerospace applications. The fracture toughness tests are mainly based on BS 7448 with some modifications for transversely isotropic behaviour of the composite materials.

By loading on specimens in the direction perpendicular to the fibre axis, three critical values of fracture toughness parameters characterizing fracture resistance of material, plane strain fracture toughness K_{Ic}, critical crack tip opening displacement $\mathrm{CTOD_c}$ and critical $\mathcal{J}$-integral $\mathcal{J}_{Ic}$ are measured for two kinds of titanium alloy specimens and three kinds of Ti/SiC composites specimens.

The values of K_Q obtained from the fracture toughness tests are not valid K_{Ic} for these materials, since the thickness of specimens is insufficient to satisfy the minimum thickness criterion; however, the results could be used as particular critical fracture toughness parameter for 0.5 mm thick structures of the materials. The valid values of $\mathcal{J}_{Ic}$ and $\mathrm{CTOD_c}$ could be used as fracture toughness parameters for all thickness of structures of the materials. The results also show that: fracture toughness of the titanium alloys decreases dramatically after being unidirectional reinforced with SiC fibre, which is mainly triggered by poor fibre/matrix bonding condition. Moreover, Ti-Al3-V2.5 reinforced with 25% volume fraction SiC fibre performs better than the other two composites in fracture resistance.

Keywords: Ti/SiC composites; facture toughness tests; fibre direction perpendicular to the loading direction; 0.5 mm thick; K_{Ic}, $\mathrm{CTOD_c}$, $\mathcal{J}_{Ic}$.

ACKNOWLEDGEMENTS

I would like to thank my supervisor Prof. Rade Vignjevic, for his guidance and advice throughout the thesis, and Dr. James Campbell for his support and advice during the research. And I also appreciate Reaction Engines Limited for offering such a good subject and all the specimens for my research.

I also would like to thank my boss and colleagues in COMAC for their financial and spiritual support. I also appreciate the support and understanding from my wife Peipei Lei.

Last but not least, I would like to thank Qiang Fu and Daqing Yang for their always kind helps. Whenever I was confused, they always gave me some reasonable suggestions.

TABLE OF CONTENTS

LIST OF FIGURES

LIST OF TABLES

NOTATION

a_0:	Average original crack length
Δa:	Average stable crack extension.
B:	Specimen thickness
c	Volume fraction
C:	Stiffness matrix
E:	Young’s modulus
E'	‘Apparent’ Young’s modulus in the accounted direction in the plane strain case
F:	Particular value of applied force
$\mathrm{F}_{\mathrm{max}}$:	Maximum force in a K_{Ic} determination
G:	Shear modulus
$\mathcal{J}$:	Experimental equivalent of crack tip $\mathcal{J}$-intergral
$\mathcal{J}_{Ic}$:	Critical $\mathcal{J}$ at the onset of brittle crack extension or pop-in when Δa is less than 0.2 mm.
$\mathcal{J}_Q$:	Provisional value of $\mathcal{J}_{Ic}$
K:	Stress intensity factor
K_{Ic}:	Plane strain fracture toughness
K_Q:	Provisional value of K_{Ic}
S:	Compliance matrix

$\mathcal{G}$: Energy release rate

$\mathcal{G}_{Ic}$: Critical energy release rate

$\mathrm{U_P}$: Plastic component of area under plot of force versus load-line displacement

V: Displacement

W: Effective width of test specimen

δ: Crack tip opening displacement (CTOD)

δ_5 Schwalbe's crack-tip opening displacement

υ: Poisson' ratio

ε: Strain

σ: Stress

σ_{ys}: 0.2% yield strength at room temperature

ξ: Reinforcement factor

$\mathrm{CTOD_c}$: Critical crack tip opening displacement

Subscripts

1: Local 1 direction

2: Local 2 direction

3: Local 3 direction

12: Local 12 plane

13: Local 13 plane

23: Local 23 plane

f: Fibre

m: Matrix

x: Global x direction

y: Global y direction

z: Global z direction

yz: Global yz plane

pl: Plastic component

el: Elastic component

1 Introduction

Fracture has been a problem faced by human ever since the emergence of man-made structures. Moreover, the problem is worsening due to the increasing complexity of technology.

One of the most famous failures is the brittle fracture of the Liberty ships during the World War Ⅱ. These ships used a revolutionary fabricating procedure, had all-welded hulls. During World War Ⅱ, out of roughly 2700 Liberty ships built, approximately 400 sustained fracture, 20 ships suffered catastrophic failure and 10 ships broke in two [1] (see Fig 1-1). There have also been catastrophic accidents in aerospace. In 1992, a Boeing 747-200 engine separated from its pylon near Amsterdam, due to fatigue and fracture of components connecting the pylon to the wing.

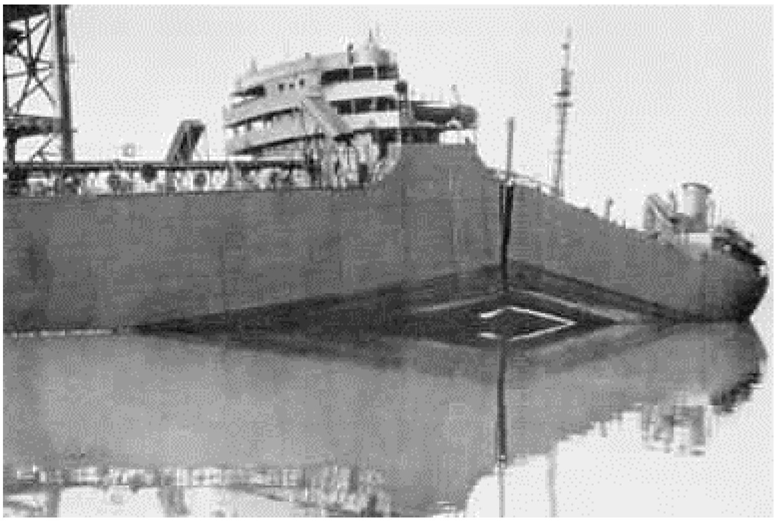

Fig 1-1 Liberty ship fracture (from http://www-mdp.eng.cam.ac.uk)

A study estimated that the annual loss due to fracture in the U.S. was $119 billion in 1971, which was 4% of the gross national product [2]. This study also estimated that the annual loss could have been reduced by $35 billion if fracture mechanics technology were applied.

Existing procedures and knowledge are helpful to avoid most failures. Today most steel ships are welded, but similar problems are avoided because of lessons learned from the Liberty ships.

However, it is much more difficult to prevent failures when new designs are introduced, especially for new materials. New materials can offer tremendous advantages, but also introduce potential problems. Therefore, new designs and new materials should be extensively tested and analyzed before application.

Titanium based alloys reinforced uniaxially with silicon carbide fibres are advanced composite materials, which combine high strength, stiffness and usable temperature range with low density. Ti/SiC composites are promising materials for gas turbine engines and super-sonic aircrafts. Reaction Engines Limited has designed a spaceplane, SKYLON, the fuselage of which is expected to be Ti/SiC space frame. To minimize the structure weight, the Ti/SiC components would be very thin (0.5 mm).

However, the behaviour of the Ti/SiC composites in the direction transverse to the fibre axis is one of the most potential risks for applications. The risk is induced by relatively high fabricating process induced thermal residual stress and weak interface between fibre and matrix [3]. Components may contain some internal defects and surface imperfections due to manufacture, assembly and maintenance as well as operation. When a crack reaches a certain critical length, even if the stress is much less than that would normally cause yield or failure, it can propagate catastrophically.

To ensure the safe application of 0.5 mm thick Ti/SiC composites, various experiments and analysis should be conducted to identify the properties of this material, especially the fracture toughness parameters which characterize the crack resistance. Fig 1-2 illustrates the relationships between fracture toughness, applied stress and flaw size. The stress and flaw size are the driving force for fracture; fracture toughness is the inherent resistance of a material to crack propagation. Fracture occurs when the driving force reaches or exceeds the material’s resistance [1]. The fracture mechanics approaches to structural design, material selection and failure assessment are all based on the knowledge of the material fracture toughness.

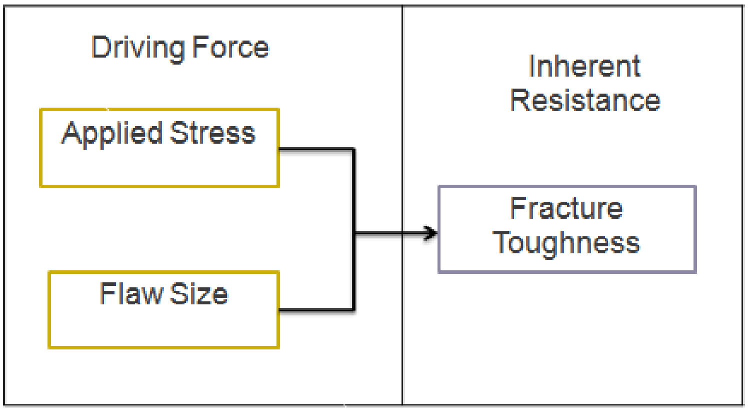

Fig 1-2 Relationship between the three critical variables in fracture mechanics [1]

Therefore, in this research, three kinds of precracked 0.5 mm thick Ti/SiC composites specimens are tested under tensile loading transverse to fibre direction to obtain the initial values of fracture toughness parameters in the direction perpendicular to the fibre axis. The validity of the results of the fracture toughness parameters have to be analyzed, since the thickness of the specimens is insufficient to satisfy the thickness criteria.

1.1 Thesis Objectives

This research aims to obtain the initial values of fracture toughness parameters of 0.5 mm thick Ti/SiC composite in the transverse direction by testing on specimens, which will help to ensure the safety of applications of 0.5 mm thick Ti/SiC composite.

The main objectives of the research are listed as follows:

(1) Learn basic mechanics of fibrous composites.

(2) Test on specimens to obtain values of fracture toughness parameters: plane strain fracture toughness K_{Ic}, critical crack tip opening displacement $\mathrm{CTOD_c}$ and critical $\mathcal{J}$-integral $\mathcal{J}_{Ic}$.

(3) Analyze the validity and application of the test results.

1.2 Thesis Structure

The thesis is organized in the following order:

(1) Chapter 1 introduces the problem; Chapter 2 presents a literature review on Ti/SiC composite, mechanics of fibrous composites and fracture mechanics.
(2) Experiments are described in Chapter 3.
(3) Results are presented, analyzed and discussed in Chapter 4.
(4) Research conclusions are detailed in Chapter 5; Chapter 6 offers some suggestions for future work.

2 Literature Review

An overview of the available literature on relative fields was carried out to support the research. Ti/SiC composites are advanced and promising materials for their outstanding properties. Mechanics of fibrous composite provides the fundamental information and formulations of fibrous composites, including engineering properties, elastic properties and failure predictions. Fracture mechanics is one of the most important approaches to evaluate the damage tolerance of failure behaviour of structures. BS 7448 and ASTM E 1820 are the most widely used standards for fracture mechanics toughness tests [1]. Finally, anti-buckling plates are used when testing on thin specimens.

2.1 Ti/SiC Composite

2.1.1 General

A composite is a material comprised of two or more physically and chemically distinct parts. Fibrous composite material comprises fibre and matrix, and its properties depend upon the choice of fibre and matrix. A wide variety of fibres and matrix are now available for use in advanced composites [4].

Nowadays, fibrous composites are preferable material choices for designers; the most cited advantage of fibrous composites is their specific stiffness and high specific strength as compared with traditional engineering materials [5, 6, 7]. Especially in the aerospace industry, where weight critically affects fuel consumption, performance and payload, the search for lighter, stiffer, and stronger materials is ongoing.

Titanium (Ti) based alloy matrix has higher transverse strength and toughness even at high temperatures; the yield strength and ultimate tensile strength of some titanium alloys are around 1100 and 1200 MPa, respectively [8].The relatively low density of titanium alloy also makes it an attractive matrix choice for composite materials.

Silicon carbide (SiC) fibre has excellent strength and stiffness at room temperature; it can maintain strength and stiffness for extended times even at extremely high temperatures; SiC fibre also exhibits exceptional wear and corrosion resistance capability. All these excellent characters are owing to its chemical composition, crystal line structure, small crystal size, and very low oxygen content.

Compared with monolithic titanium alloys, titanium matrix composites not only offer 40% more stiffness, but also save 25% weight [9]. Thus, titanium based alloys reinforced uniaxially with silicon carbide fibres are obviously innovative materials for aerospace vehicles. Fig 2-1 shows a military jet engine designed by MTU Aero Engines Co, which aimed to improve current compressor design [10]. The blade ring design dramatically saves weight compared to the blade disk, but the replacement of disk can only be realized by fibre reinforced titanium alloy for the mechanical loading where the atmosphere temperature exceeds 600℃. [11]

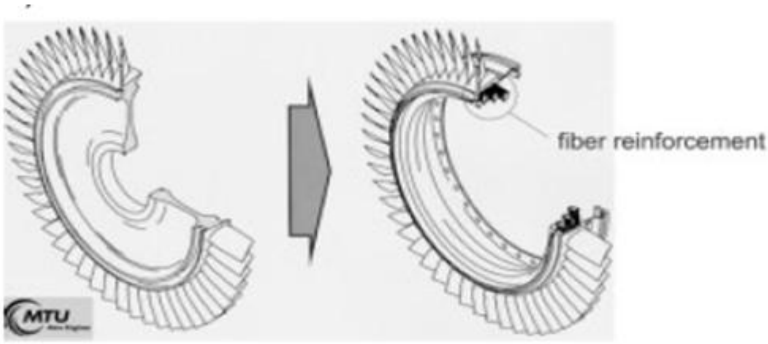

Fig 2-1 Design of blade ring by MTU Aero Engines Co [10]

However, the improvement in the direction transverse to the fibre axis is limited, since it is significantly influenced by the fibre/matrix bonding strength. A comparison of behaviours of single layer Ti-6Al-4V/SiC composite specimens at three thicknesses under remote transverse tensile loading is demonstrated in Fig 2-2 [12]. The initial slope of the curves for all the specimens was almost the same, but with increasing load, a discontinuous increase in stress occurred at point ‘A’ where the stress was much lower than the yield strength of titanium matrix, this had been correlated to fibre/matrix interface debonding [13]. For the thin specimen (230 µm), it exhibited significant discontinuous increase in stress and great reduction in stiffness, and failed rapidly with increasing loading. Therefore, the stress at debonding point ‘A’ could be assumed as the yield strength of the thin specimen.

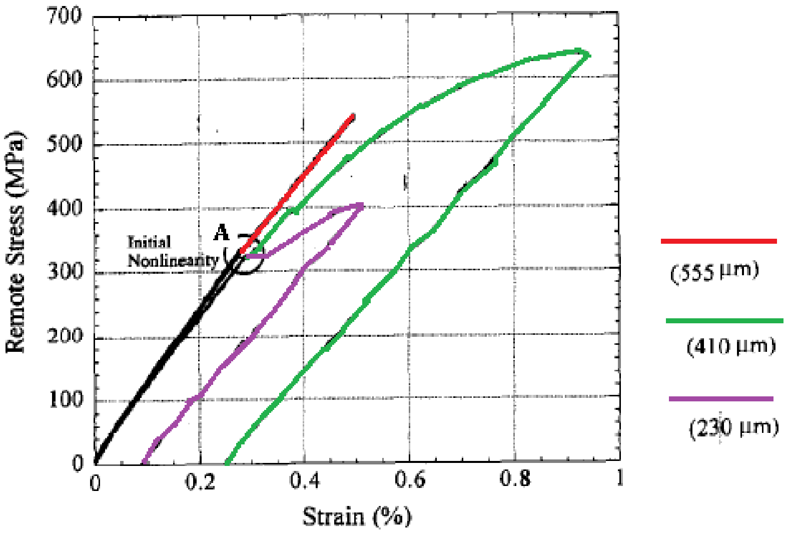

Fig 2-2 Stress-strain curves for three Ti-6Al-4V/SiC specimens with different thickness [12]

2.1.2 Ti/SiC Fabrication Process

Nowadays, there are three favoured methods to fabricate Titanium Matrix Composites (TMC), shown in Fig 2-3: the foil-fibre-foil (FFF) technique, the mono tape (MT) technique and the matrix-coated fibre (MCF) technique [10].

Foil-fibre-foil (FFF) fabrication technique: fibres are placed between foils and stacked to a multilayer arrangement, and then the layers are consolidated at high temperature and pressure. This method, though simple and the cheap, has a major technical disadvantage: it is difficult to distribute the fibres homogeneously, for the fibres can easily shift during the fabrication process, and this strongly influences the properties of the composites.

The Mono tape (MT) fabrication technique makes some progress in homogeneous fibre distribution. First, fibre reinforced tapes are produced; then the tapes are stacked or bundled to a multilayer arrangement; at last the layers are consolidated at high temperatures and pressure.

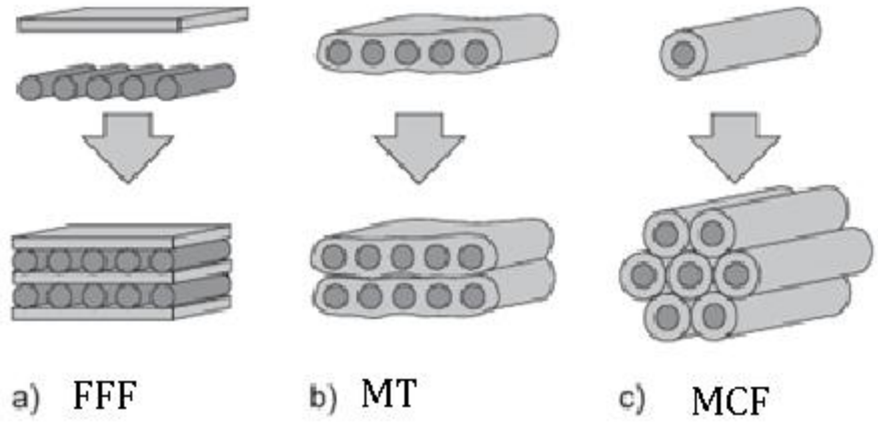

Fig 2-3 Titanium matrix composites(TMC) fabrication technique [10]

Matrix-coated fibre (MCF) is the most costly method so far, which helps to fabricate the composites with optimum fibre distribution. The first step is to product homogeneously matrix coated fibres; in the second step, the fibres are bundled or arranged in a multilayer manner, and finally pressed at high temperatures and high pressures.

For all three fabrication processes, the materials are consolidated in vacuum at about 950℃ under 30 MPa. Different coefficients of thermal expansion between the titanium matrix and fibres could induce residual stress after cooling down, the residual stress would provide radial compressive stresses at the interface, and the typical value of residual stress for Ti-6Al-4V is about -300MPa [12]. The residual stress would be helpful for improving bonding strength, but it might also induce crack in the matrix [13]. Moreover, to avoid chemical reaction between the fibre and the matrix, a carbon protective layer (shown in Fig 2-4) is applied. During consolidation, it is unavoidable that chemical reaction occurs between titanium matrix and carbon coating layer. The fibre/matrix bonding strength is significantly influenced by the composition and microstructure of the interface, and the residual stresses at the interface [3, 13, 14].

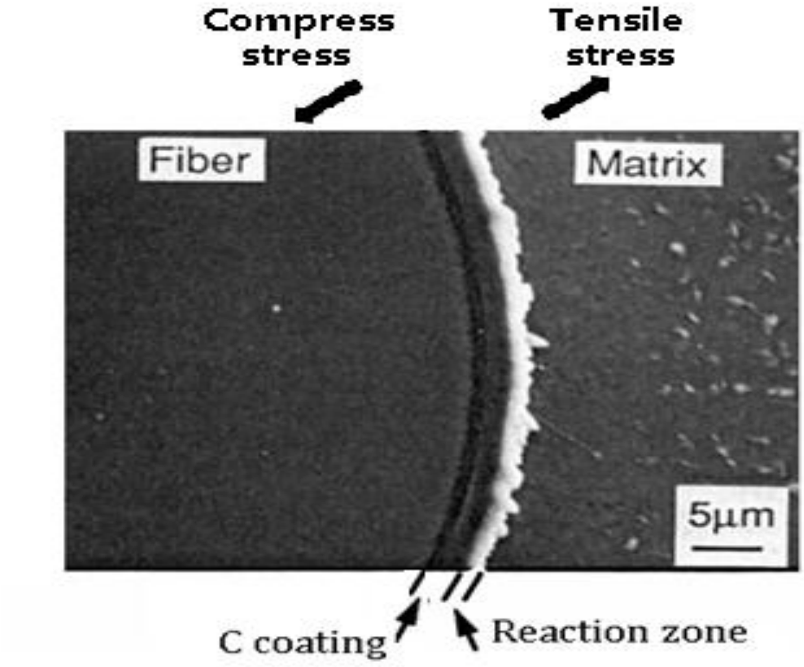

Fig 2-4 Micrograph of the interfacial region [15]

2.1.3 Previous Investigations on Ti/SiC

To safely apply Ti/SiC composites in aerospace applications, a large number of experiments and models have been conducted to investigate the limitations of these composites, which are induced by the presence of the brittle SiC fibres, and to analyze the micro-level failure mechanisms under different loading conditions.

2.1.3.1 Investigations on Smooth Materials

Experimental investigations have shown that matrix [16], fibre [17], and interface [16] behaviour remarkably influence the tensile strength of smooth Ti/SiC composite specimens. The stiffness of titanium matrix is much less than that of fibres, so fibres take most of loads in the fibre direction, the strength characteristics of the fibre is efficiently utilized. The behavior of titanium matrix composite in the transverse direction is significantly influenced by the strength of matrix, residual stress and fibre/matrix interface strength. For Ti-6Al-4v reinforced with 34% SiC composite, the plastic deformation of matrix initiates at 1275 MPa of external tensile load in the fibre direction, which is much greater than the yield strength of the matrix alloy [46]; the matrix yielding starts at about 330 MPa of external transverse tensile stress and the plastic deformation propagates in the matrix gradually [46], which is normally less than half of the yield strength of titanium matrix.

Models have been developed to reveal the relationship between the composite microstructure and constituent properties to the tensile stress-strain curve [18]. An investigation of the ultimate tensile strength and fracture strain of a fibre reinforced titanium matrix composite has been conducted by C.H. Weber, as well as comparisons between two micromechanical models and experimental measurements [19]. The tensile strength of titanium composites can be more accurately predicted by modifying the conventional rule of mixture with interfacial mechanical properties [15].

2.1.3.2 Failure Mechanism and Modes

Investigations on failure mechanisms and failure modes of titanium matrix composite also have been carried out.

Due to the difference of stiffness between the matrix and the fibres, the stress in the matrix is different from that in the fibres under loading in the fibre direction, which will induce a shear stress along the interface. When the shear stress reaches the interfacial bonding strength, the interface will fail and relative sliding between the matrix and the fibre will occur. The interfacial bonding strength is influenced by two factors [14]: (1) chemical bonding which is determined by the nature of the interfacial reaction between fibre and matrix; (2) mechanical residual stress which is mainly induced by the difference of coefficients of thermal expansion or the volume change of titanium matrix caused by phase transformation during fabricating.

When the composite is under transverse tensile loading, there are two types of local stresses at the fibre/matrix interface that act to debond the interface (shown in Fig 2-5) [12]: (1) normal radial tension with the maximum value at $\theta = 0^{\circ}$; (2) tangential shear stress with the maximum value at $\theta = 45^{\circ}$. So, generally there are two modes of interface failure [13]: normal separation and tangential shear sliding, usually the interface failure is a combination of these two failure modes. Therefore, two bonding failure criteria have been developed.

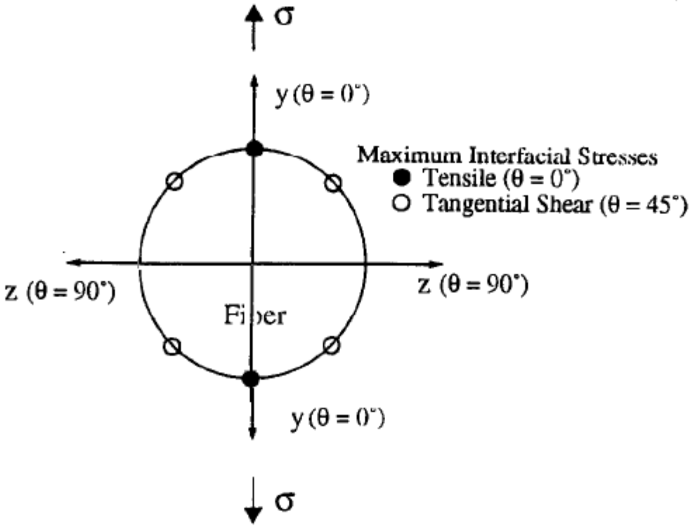

Fig 2-5 Diagram of maximum interfacial stress

In reference 17, after comparing the Ti-6A1-4V/ SCS-6 samples with the same Ti-alloy matrix reinforced with other SiC fibres samples, the results show that the average shear stress obtained by fragmentation test is much higher than from push-out tests; and it can also be found from micrographs that there is little continuous shear crack along the interface but radial crack damage to the coating.

C. González’s model can accurately predict the average composite strength and damage extent, if the failure is caused by the nucleation of a cluster containing two neighbour broken fibres [20].

2.1.3.3 Fracture Toughness of Titanium Matrix Composite

There are also some investigations have been carried out experimentally and numerically on the fracture characteristics of titanium matrix composites.

The fracture behaviour of Ti-6Al-4V/SiC is studied between 20℃ and 500℃, the research finds that [25]: (1) the critical energy release rate keeps relatively constant ($94.5 \pm 10\ \mathrm{kJ/m^2}$) in the whole temperature range, while the toughness decreases linearly from $78\ \mathrm{MPa}\sqrt{\mathrm{m}}$ at 20℃ to $44\ \mathrm{MPa}\sqrt{\mathrm{m}}$ at 550℃; (2) the fractured specimen indicates that the failure is caused by a single crack perpendicular to the fibre from the notch root, fibre bridging and pull-out in the crack also occur. The stress distributions in bridging fibres and in the matrix ahead of the crack have been accurately measured for fatigue cracked Ti-6Al-4V/SiC composites [46].

Finite element methods have also been presented to evaluate the interfacial fracture toughness of titanium matrix composites. Reference 47 shows that the interfacial fracture toughness of titanium matrix composites increases with increasing peak load and decreases with increasing frictional force; this research also indicates that the energy release rate of Timetal-834/SiC composites increases at the supported end and the decrease at the loading end [47].

Further efforts have already been made from the aspect of microstructure characteristics to predict the service life of components made of titanium matrix composites [21].

2.1.3.4 Summary

Most of the investigations and models concentrate on the behaviour of smooth specimens; relatively fewer investigations have been carried out to gain the understanding of the fracture characteristics of Ti/SiC material, especially for the composite materials with 0.5 mm thickness in this thesis.

In the following, the basic knowledge of mechanics of fibrous composites is studied; fracture mechanical methods are introduced to reveal the material's inherent resistance to crack growth.

2.2 Basic Mechanics of Fibrous Composites

Well established theories exist on mechanics of fibrous composites, including the stress-strain relationships at the level of lamina and laminate, the relationships between the engineering constants and the compliance coefficients, as well as failure mechanisms and theories of composites. All these theories pave the way for the application and development of fibrous composites. The equations in this chapter were mainly referred to reference 4.

2.2.1 General Elastic Relationships of Fibrous Composites

The elastic relationship between stress and strain for fibrous composite materials is referred to as Hooke's Law. The general relationship between stresses and strain is

$$\sigma_i = C_{ij}\varepsilon_j \qquad [2.1]$$

$$\text{or,} \quad \varepsilon_i = S_{ij}\sigma_j \qquad [2.2]$$

Where:

The coefficients S_{ij} are compliance coefficients, the coefficients C_{ij} are stiffness coefficients.

The compliance matrix is the inverse of the stiffness matrix, $[S_{ij}] = [C_{ij}]^{-1}$; ε_i is strain tensor; σ_j is stress tensor;

The stiffness matrix of orthotropic material is:

$$[\mathrm{C_{ij}}] = \begin{bmatrix} \mathrm{C}_{11} & \mathrm{C}_{12} & \mathrm{C}_{13} & 0 & 0 & 0 \\ \mathrm{C}_{12} & \mathrm{C}_{22} & \mathrm{C}_{23} & 0 & 0 & 0 \\ \mathrm{C}_{13} & \mathrm{C}_{23} & \mathrm{C}_{33} & 0 & 0 & 0 \\ 0 & 0 & 0 & \mathrm{C}_{44} & 0 & 0 \\ 0 & 0 & 0 & 0 & \mathrm{C}_{55} & 0 \\ 0 & 0 & 0 & 0 & 0 & \mathrm{C}_{66} \end{bmatrix} \qquad [2.3]$$

The compliance matrix of orthotropic material is:

$$[\mathrm{S_{ij}}] = \begin{bmatrix} \mathrm{S}_{11} & \mathrm{S}_{12} & \mathrm{S}_{13} & 0 & 0 & 0 \\ \mathrm{S}_{12} & \mathrm{S}_{22} & \mathrm{S}_{23} & 0 & 0 & 0 \\ \mathrm{S}_{13} & \mathrm{S}_{23} & \mathrm{S}_{33} & 0 & 0 & 0 \\ 0 & 0 & 0 & \mathrm{S}_{44} & 0 & 0 \\ 0 & 0 & 0 & 0 & \mathrm{S}_{55} & 0 \\ 0 & 0 & 0 & 0 & 0 & \mathrm{S}_{66} \end{bmatrix} \qquad [2.4]$$

The relationships between the engineering constants and the compliance coefficients are [4]:

$$\mathrm{S}_{11} = \frac{1}{\mathrm{E}_1}; \quad \mathrm{S}_{12} = \frac{-\upsilon_{12}}{\mathrm{E}_1} = \frac{-\upsilon_{21}}{\mathrm{E}_2}; \quad \mathrm{S}_{13} = \frac{-\upsilon_{13}}{\mathrm{E}_1} = \frac{-\upsilon_{31}}{\mathrm{E}_3};$$

$$\mathrm{S}_{22} = \frac{1}{\mathrm{E}_2}; \quad \mathrm{S}_{23} = \frac{-\upsilon_{23}}{\mathrm{E}_2} = \frac{-\upsilon_{32}}{\mathrm{E}_3}; \quad \mathrm{S}_{33} = \frac{1}{\mathrm{E}_3}; \qquad [2.5]$$

$$\mathrm{S}_{44} = \frac{1}{\mathrm{G}_{23}}; \quad \mathrm{S}_{55} = \frac{1}{\mathrm{G}_{13}}; \quad \mathrm{S}_{66} = \frac{1}{\mathrm{G}_{12}};$$

Where:

E=Young’s modulus; υ=Poisson’s ratio; G=Shear modulus.

A unidirectional fibrous composite exhibits isotropic property in the plane transverse to the fibres. Thus, the compliance matrix can be simplified to:

$$[\mathrm{S_{ij}}] = \begin{bmatrix} \mathrm{S}_{11} & \mathrm{S}_{12} & \mathrm{S}_{12} & 0 & 0 & 0 \\ \mathrm{S}_{12} & \mathrm{S}_{22} & \mathrm{S}_{23} & 0 & 0 & 0 \\ \mathrm{S}_{12} & \mathrm{S}_{23} & \mathrm{S}_{22} & 0 & 0 & 0 \\ 0 & 0 & 0 & \mathrm{S}_{44} & 0 & 0 \\ 0 & 0 & 0 & 0 & \mathrm{S}_{66} & 0 \\ 0 & 0 & 0 & 0 & 0 & \mathrm{S}_{66} \end{bmatrix} \qquad [2.6]$$

The principal material (1-2-3) coordinate system and global (x-y-z) coordinate system are shown in Fig 2-6, the two coordinate systems share the same z-(3) axis and the x-axis rotates a positive counter clockwise angle θ to the 1-axis.

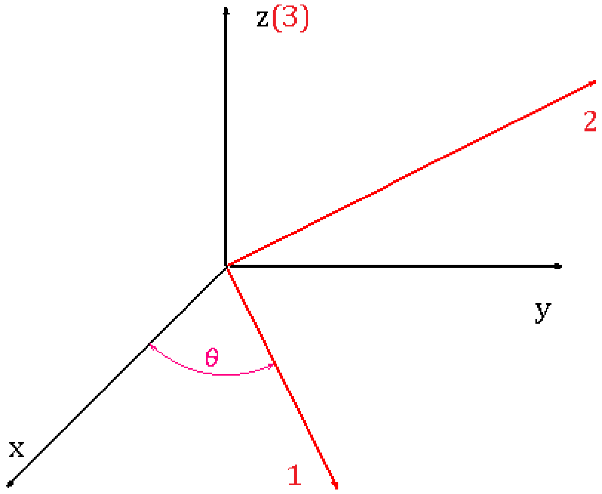

Fig 2-6 Relationship between principal material coordinate system and global coordinate system

Transformation matrix $[T_1]$ is defined for the transformation of stress, so the relationship between stresses in the principal material and global coordinates can be expressed as [4]；

$$\{\sigma\}_1 = [T_1]\{\sigma\}_x \quad [2.7]$$

Where:

$$[T_1] = \begin{bmatrix} m^2 & n^2 & 0 & 0 & 0 & 2mn \\ n^2 & m^2 & 0 & 0 & 0 & -2mn \\ 0 & 0 & 1 & 0 & 0 & 0 \\ 0 & 0 & 0 & m & -n & 0 \\ 0 & 0 & 0 & n & m & 0 \\ -mn & mn & 0 & 0 & 0 & m^2 - n^2 \end{bmatrix} \quad [2.8]$$

And $m=\cos\theta$, $n=\sin\theta$; θ is defined in Fig 2-6.

Transformation matrix $[T_2]$ is defined for the transformation of strain, so the relationship between strains in the principal material and global coordinates can be expressed as [4]；

$$\{\varepsilon\}_1 = [T_2]\{\varepsilon\}_x \quad [2.9]$$

Where:

$$[T_2] = \begin{bmatrix} m^2 & n^2 & 0 & 0 & 0 & mn \\ n^2 & m^2 & 0 & 0 & 0 & -mn \\ 0 & 0 & 1 & 0 & 0 & 0 \\ 0 & 0 & 0 & m & -n & 0 \\ 0 & 0 & 0 & n & m & 0 \\ -2mn & 2mn & 0 & 0 & 0 & m^2 - n^2 \end{bmatrix} \quad [2.10]$$

So, the elastic relationship of composite in global coordinates can be expressed as:

$$\{\sigma\}_x = [\bar{C}]\{\varepsilon\}_x \quad [2.11]$$

Where:

$[\bar{C}]$ is the transformed stiffness matrix, $[\bar{C}] = [T_1]^{-1}[C][T_2]$.

2.2.2 Single Lamina Elastic Relationships

For a single lamina with unidirectional fibre orientation θ relative to the global coordinates (Fig 2-7), the stress-strain relationship is

$$\begin{Bmatrix} \sigma_x \\ \sigma_y \\ \sigma_z \\ \tau_{yz} \\ \tau_{zx} \\ \tau_{xy} \end{Bmatrix} = \begin{bmatrix} \bar{C}_{11} & \bar{C}_{12} & \bar{C}_{13} & 0 & 0 & \bar{C}_{16} \\ \bar{C}_{12} & \bar{C}_{22} & \bar{C}_{23} & 0 & 0 & \bar{C}_{26} \\ \bar{C}_{13} & \bar{C}_{23} & \bar{C}_{33} & 0 & 0 & \bar{C}_{36} \\ 0 & 0 & 0 & \bar{C}_{44} & \bar{C}_{45} & 0 \\ 0 & 0 & 0 & \bar{C}_{45} & \bar{C}_{55} & 0 \\ \bar{C}_{16} & \bar{C}_{26} & \bar{C}_{36} & 0 & 0 & \bar{C}_{66} \end{bmatrix} \begin{Bmatrix} \varepsilon_x \\ \varepsilon_x \\ \varepsilon_x \\ \gamma_{yz} \\ \gamma_{zx} \\ \gamma_{xy} \end{Bmatrix} \quad [2.12]$$

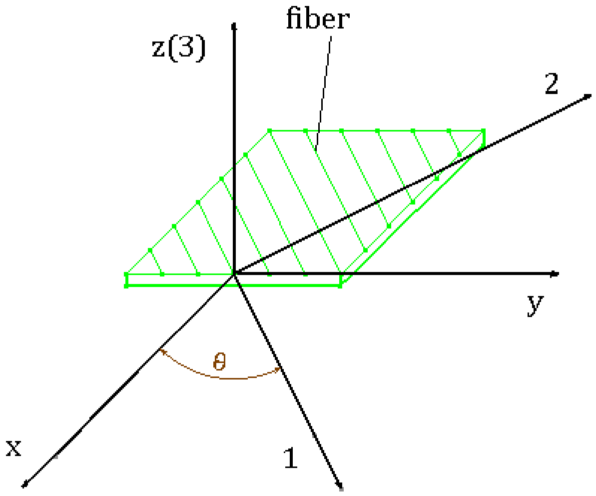

Fig 2-7 Single lamina in global and principal coordinates

For the plane stress condition, all the out-of-plane components of stress are zero；

$$\sigma z = \tau_{yz} = \tau_{zx} = 0 \qquad [2.13]$$

So, the plane stress constitutive equation in global coordinates is expressed as

$$\begin{Bmatrix} \sigma_x \\ \sigma_y \\ \tau_{xy} \end{Bmatrix} = [\bar{Q}] \begin{Bmatrix} \varepsilon_x \\ \varepsilon_y \\ \gamma_{xy} \end{Bmatrix} \qquad [2.14]$$

Where:

$[\bar{Q}]$ is the reduced transformed stiffness matrix,

$$[\bar{Q}] = \begin{bmatrix} m^2 & n^2 & 2mn \\ n^2 & m^2 & -2mn \\ -mn & mn & m^2-n^2 \end{bmatrix}^{-1} \begin{bmatrix} C_{11} & C_{12} & 0 \\ C_{21} & C_{22} & 0 \\ 0 & 0 & C_{66} \end{bmatrix} \begin{bmatrix} m^2 & n^2 & mn \\ n^2 & m^2 & -mn \\ -2mn & 2mn & m^2-n^2 \end{bmatrix};$$

2.2.3 Linear Elastic Response of Laminated Composites

A serial of equations have been developed to describe the linear elastic response of a laminated composite subjected to in-plane forces and bending moments. These equations are based on the following assumptions [4];

(1) Each layer is isotropic, orthotropic or transversely isotropic.
(2) Each layer is in a state of plane stress.
(3) The bonding condition between each layer is perfect.
(4) For each layer, deformation normal to midplane does not change length.

A schematically presentation of a laminate deformation is show in Fig 2-8. The origin of the coordinate system is located on the laminate midplane. Under in-plane forces and bending moments, the displacements of the laminate are small, the displacements of point ‘O’ (on the midplane) is (u^0, v^0, w^0), the displacements of point ‘A’ is (u, v, w).

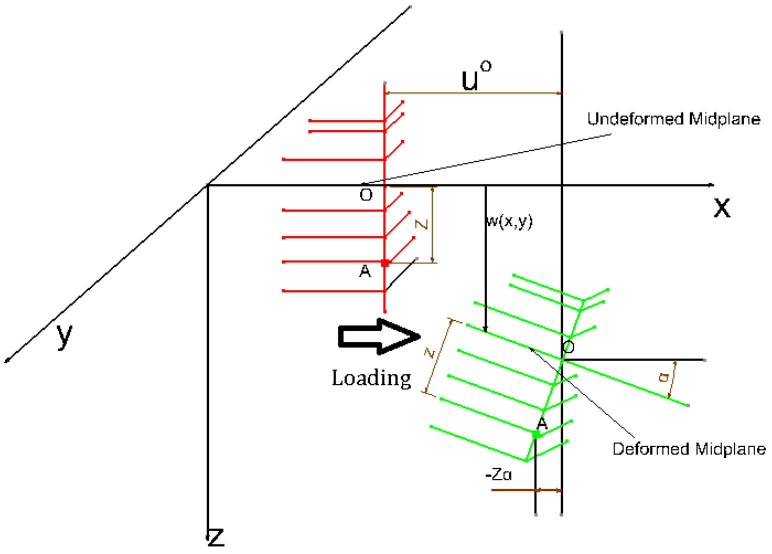

Fig 2-8 Laminate deformed under loading [4]

The total x-displacement of point ‘A’, in Fig 2-8, can be written as the sum of the x-displacement of point ‘O’ and the displacement due to rotation [4]. So,

$$u = u^0 - z\tan\alpha = u^0 - z\alpha = u^0 - z\frac{\partial w}{\partial x} \quad [2.15]$$

Where:

u and u^0 are the x-displacement of point ‘A’ and point ‘O’.

z is the distance between point ‘A’ and point ‘O’.

α is the rotation angle of midplane at point ‘O’, since α is small, $\tan\alpha=\frac{\partial w}{\partial x}\approx\alpha$.

Likewise, the total y-displacement of point ‘A’, in Fig 2-8, can be written as the sum of the y-displacement of point ‘O’ and the displacement due to rotation. So,

$$v = v^0 - z\frac{\partial w}{\partial y} \quad [2.16]$$

According to the assumption (4), the deformation normal to midplane does not change length, so the total z-displacement of point ‘A’, in Fig 2-8, equals to the z-displacement of point ‘O’.

$$w(x,y) = w^0(x,y) \quad [2.17]$$

Therefore, the strains can be expressed as:

$$\varepsilon_x = \frac{\partial u}{\partial x} = \frac{\partial(u^0 - z\frac{\partial w}{\partial x})}{\partial x} = \varepsilon_x^0 + z\kappa_x$$

$$\varepsilon_y = \frac{\partial v}{\partial y} = \frac{\partial(v^0 - z\frac{\partial w}{\partial y})}{\partial y} = \varepsilon_y^0 + z\kappa_y \qquad [2.18]$$

$$\gamma_{xy} = \left(\frac{\partial u}{\partial y} + \frac{\partial v}{\partial x}\right) = \frac{\partial u^0}{\partial y} + \frac{\partial v^0}{\partial x} - 2z\frac{\partial^2 w}{\partial x\,\partial y} = \gamma_{xy}^0 + z\kappa_{xy}$$

Where:

$$\text{The curvatures } \{\kappa\} = \begin{Bmatrix} -\frac{\partial^2 w}{\partial x^2} \\ -\frac{\partial^2 w}{\partial y^2} \\ -2\frac{\partial^2 w}{\partial x\,\partial y} \end{Bmatrix} \qquad [2.19]$$

So, the equation 2.18 can be rewritten as

$$\{\varepsilon\} = \{\varepsilon\}^0 + z\{\kappa\} \quad [2.20]$$

The Equation 2.20 indicates that the total strains in global coordinates, $\{\varepsilon\}$, at any z-location in the laminate can be expressed in terms of the midplane strains

$\{\varepsilon\}^0$, and the curvatures $\{\mathscr{k}\}$. The equation 2.20 is the fundamental equation to describe the linear elastic response of a laminated composite.

By applying Hooke's Law, the stresses at any z-location can be written as:

$$\{\sigma\} = [\bar{Q}]^k\{\varepsilon\} = [\bar{Q}]^k\{\varepsilon\}^0 + [\bar{Q}]^k z\{\mathscr{k}\} \quad [2.21]$$

Where:

$[\bar{Q}]^k$ is reduced transformed stiffness of the *k*th layer corresponding to the z-location.

So, the stresses at any z-location can be expressed in terms of the midplane strains $\{\varepsilon\}^0$, and the curvatures $\{\mathscr{k}\}$.

For the *k*th layer with thickness of $(z_k - z_{k-1})$, the in-plane forces through-thickness of a layer can be described as:

$$\{N\}^k = \int_{z_{k-1}}^{z_k}\{\sigma\}dz = [\bar{Q}]^k\{\varepsilon\}^0(z_k - z_{k-1}) + \frac{1}{2}[\bar{Q}]^k\{\mathscr{k}\}(z_k^2 - z_{k-1}^2) \quad [2.22]$$

Therefore, the in-plane force for the laminate with H layers can be expressed as the sum of the in-plane forces through-thickness of each layer.

$$\{N\} = \sum_{k=1}^{H}\{N\}^k = [A]\{\varepsilon\}^0 + [B]\{\mathscr{k}\} \quad [2.23]$$

Where:

$[A]$ is the in-plane stiffness, $[A] = \sum_{k=1}^{H}[\bar{Q}]^k\,(z_k - z_{k-1})$;

$[B]$ is the bending-stretching coupling, $[B] = \frac{1}{2}\sum_{k=1}^{H}[\bar{Q}]^k(z_k^2 - z_{k-1}^2)$;

$[\bar{Q}]^k$ is the reduced transformed stiffness of the *k*th layer, which varies with orientation of each layer.

For the *k*th layer with thickness of $(z_k - z_{k-1})$, the moments through-thickness of a layer can be described as:

$$\{\mathrm{M}\}^{k} = \int_{z_{k-1}}^{z_k}\{\sigma\}\mathrm{z}\mathrm{dz} = \frac{1}{2}[\overline{\mathrm{Q}}]^{k}\{\varepsilon\}^{0}(\mathrm{z}_{k}^{2} - \mathrm{z}_{k-1}^{2}) + \frac{1}{3}[\overline{\mathrm{Q}}]^{k}\{\mathscr{k}\}(\mathrm{z}_{k}^{3} - \mathrm{z}_{k-1}^{3}) \quad [2.24]$$

Therefore, the moments for the laminate with H layers can be expressed as the sum of the moments through-thickness of each layer.

$$\{\mathrm{M}\} = \textstyle\sum_{\mathrm{k}=1}^{\mathrm{H}}\{\mathrm{M}\}^{k} = [\mathrm{B}]\{\varepsilon\}^{0} + [\mathrm{D}]\{\mathscr{k}\} \quad [2.25]$$

Where:

$[\mathrm{B}]$ is the bending-stretching coupling, $[\mathrm{B}] = \frac{1}{2}\sum_{k=1}^{\mathrm{H}}[\overline{\mathrm{Q}}]^{k}(\mathrm{z}_{k}^{2} - \mathrm{z}_{k-1}^{2})$.

$[\mathrm{D}] = \frac{1}{3}\sum_{k=1}^{\mathrm{H}}[\overline{\mathrm{Q}}]^{k}(\mathrm{z}_{k}^{3} - \mathrm{z}_{k-1}^{3})$.

Combining Equation 2.23 and Equation 2.25, the equation for a laminate under in-plane force and bending moments can be written as:

$$\begin{Bmatrix}\mathrm{N}\\ \mathrm{M}\end{Bmatrix} = \begin{bmatrix}\mathrm{A} & \mathrm{B}\\ \mathrm{B} & \mathrm{D}\end{bmatrix}\begin{Bmatrix}\varepsilon^{0}\\ \mathscr{k}\end{Bmatrix} \quad [2.26]$$

So, if the forces $\{\mathrm{N}\}$ and moments $\{\mathrm{M}\}$ are given, the midplane strains and curvatures can be written as [4]:

$$\begin{Bmatrix}\varepsilon^{0}\\ \mathscr{k}\end{Bmatrix} = \begin{bmatrix}\mathrm{A}' & \mathrm{B}'\\ \mathrm{C}' & \mathrm{D}'\end{bmatrix}\begin{Bmatrix}\mathrm{N}\\ \mathrm{M}\end{Bmatrix} \quad [2.27]$$

Where:

$[\mathrm{A}'] = [\mathrm{A}']^{-1} + [\mathrm{A}']^{-1}[\mathrm{B}][\mathrm{D}^{*}]^{-1}[\mathrm{B}][\mathrm{A}']^{-1}$; $[\mathrm{B}'] = -[\mathrm{A}']^{-1}[\mathrm{B}][\mathrm{D}^{*}]^{-1}$; $[\mathrm{C}'] = [\mathrm{B}']^{\mathrm{T}}$; $[\mathrm{D}'] = [\mathrm{D}^{*}]^{-1}$; $[\mathrm{D}^{*}] = [\mathrm{D}] - [\mathrm{B}][\mathrm{A}']^{-1}[\mathrm{B}]$.

Combining Equation 2.21 and Equation 2.27, the stresses of a lamina at any z-location in a laminate with given forces and moments can be written as:

$$\{\sigma\}^{k} = [\overline{\mathrm{Q}}]^{k}[[\mathrm{A}']\{\mathrm{N}\} + [\mathrm{B}']\{\mathrm{M}\} + \mathrm{z}([\mathrm{C}']\{\mathrm{N}\} + [\mathrm{D}']\{\mathrm{M}\})] \quad [2.28]$$

For a symmetric laminate, $[\mathrm{B}]=0$, the Equation 2.28 reduces to

$$\{\sigma\}^{k} = [\overline{\mathrm{Q}}]^{k}([\mathrm{A}]^{-1}\{\mathrm{N}\} + \mathrm{z}[\mathrm{D}]^{-1}\{\mathrm{M}\}) \quad [2.29]$$

The maximum stress for a given layer can be determined by the stresses distribution Equation 2.28, which would be helpful to predict the failure for the laminate.

2.2.4 Halpin-Tsai Equations

The engineering properties of composite material are determined by the properties, proportions and geometry of the matrix and the reinforcement. The Halpin-Tsai equations [22], which assume that fibre and matrix are perfectly bonded, are a set of mathematical models to predict the engineering properties of a unidirectional composite material. These equations are based on more realistic fibre distribution [23], thus they are curve fitted to exact elasticity solutions and confirmed by experimental measurements.

Longitudinal Young's Modulus: $\mathrm{E_1} = c_\mathrm{f}\mathrm{E_f} + c_\mathrm{m}\mathrm{E_m}$; [2.30-1]

Major Poisson's Ratio: $\vartheta_{12} = c_\mathrm{f}\vartheta_\mathrm{f} + c_\mathrm{m}\vartheta_\mathrm{m}$; [2.30-2]

Transverse Young's Modulus: $\mathrm{E_2} = \frac{1+\xi\eta c_\mathrm{f}}{1-\eta c_\mathrm{f}}\mathrm{E_m}$ [2.30-3]

Major Shear modulus: $\mathrm{G_{12}} = \frac{1+\xi\eta c_\mathrm{f}}{1-\eta c_\mathrm{f}}\mathrm{G_m}$; [2.30-4]

Where:

E=Young's modulus; Subscript 'm'=matrix; Subscript 'f'=fibre; ϑ=Poisson's ratio; *c* =volume fraction;

η=function of the ratio of the relevant fibre and matrix modulus and of the reinforcement factor ξ, $\eta = \frac{\frac{\mathrm{M_f}}{\mathrm{M_m}}-1}{\frac{\mathrm{M_f}}{\mathrm{M_m}}+\xi}$ [2.30-5];

$\mathrm{M_f}$=fibre values of $\mathrm{E_2}$ and $\mathrm{G_{12}}$; $\mathrm{M_m}$= matrix values of $\mathrm{E_2}$ and $\mathrm{G_{12}}$; ξ=reinforcement factor for $\mathrm{E_2}$ and $\mathrm{G_{12}}$;

The reinforcement factor ξ is determined by fibre geometry, packing arrangement and load condition. Two wildly used ξ values are shown in Fig 2-9 and Fig 2-10.

Fig 2-9 shows the reinforcement factor ξ values for calculation of E_2, G_{12} when circular fibres are arranged in square array.

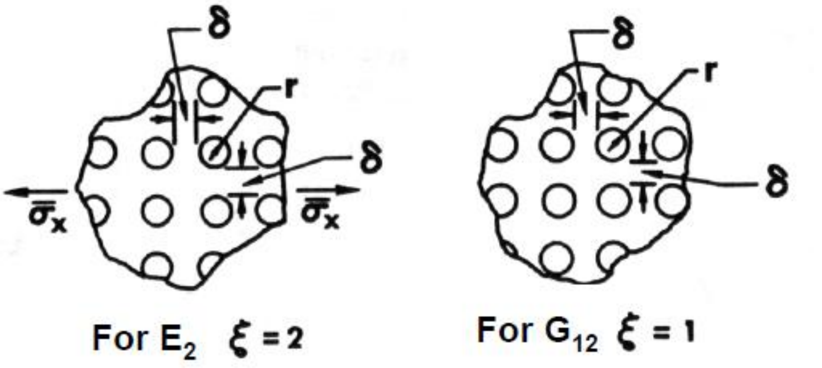

Fig 2-9 Reinforcement factor ξ for circular fibres in square array [22]

Fig 2-10 demonstrates reinforcement factor ξ values for calculation of E_2, G_{12} when rectangular cross-section fibres are arranged in diamond array.

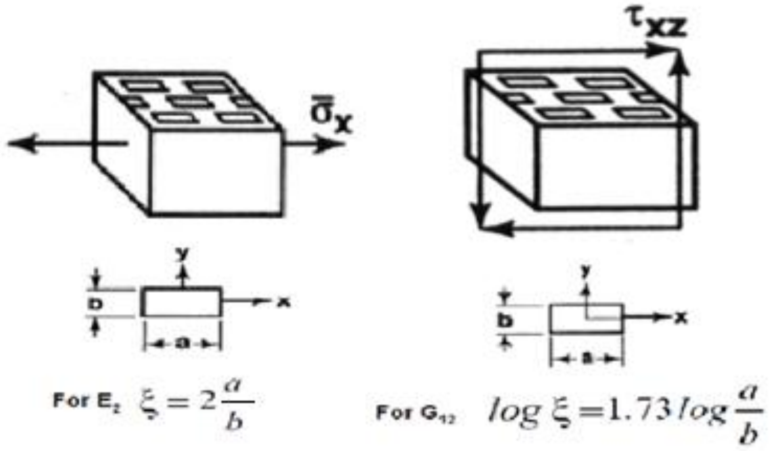

Fig 2-10 Reinforcement factor ξ for circular fibres in square array [22]

2.2.5 Failure Mechanisms and Theories of Fibrous Composites

To safely apply fibrous composites, the fundamental micro-level failure mechanisms were studied, failure theories at the level of lamina were also developed.

Fibrous composite materials fail in a variety of mechanisms, such as, fibre fracture, matrix cracking, fibre pullout, fibre buckling, fibre/matrix debonding and delaminations [4]. The failure mechanisms are not only affected by the strength of the fibres and the matrix, but also by the load direction and fibre/matrix bonding condition. Fig 2-11 illustrates some failure mechanisms occur under tensile loading, Fig 2-12 shows some failure mechanisms under compressive loading. The bonding condition effects on failure mechanisms are shown in Fig 2-13.

Fig 2-11 (a) illustrates the failure mechanisms of a unidirectional reinforced metal matrix lamina under tensile load along the fibre direction. For most of metal matrix composites, the breaking strain of fibre ε_f is much smaller than that of matrix ε_m [20], fibre takes most of the load before failure. With the increase of load, fibres fracture first, then the load transfers to the bonding area and matrix, matrix and the bonding strength cannot take the extra load, fibre/matrix debonding and fibre pullout occur, matrix fractures. Fig 2-11 (b) is a scanning electron micrograph of lateral fracture surface [25], it can be found failure mechanisms in it, including fibre fracture, matrix fracture, fibre/matrix debonding and fibre pullout.

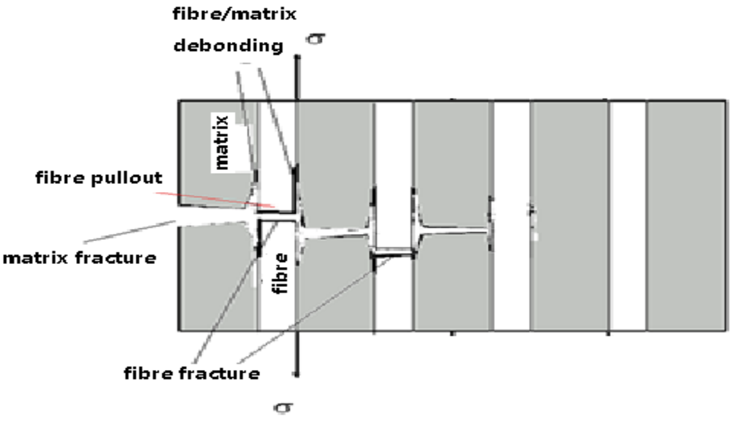

(a)

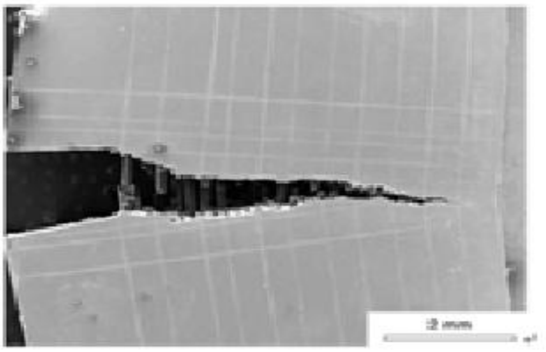

(b) [25]

Fig 2-11 Failure mechanisms under tensile loading

For fibre reinforced composites, the failure behaviour under compressive loading is significantly different from under tensile loading. The major failure mode under compressive loading is fibre buckling and matrix shear failure. Fibre buckling tends to occur when the composite is under longitudinal compressive loading. In Fig 2-12 (a) [26] fibre buckling behaviour is schematically shown under longitudinal compressive loading, poor alignment of fibres or fibre with initial curvature would result in easy buckling under compressive loading. For transverse compressive loading, matrix shear fracture and fibre/matrix debonding are most likely to occur, which are shown in Fig 2-12 (b).

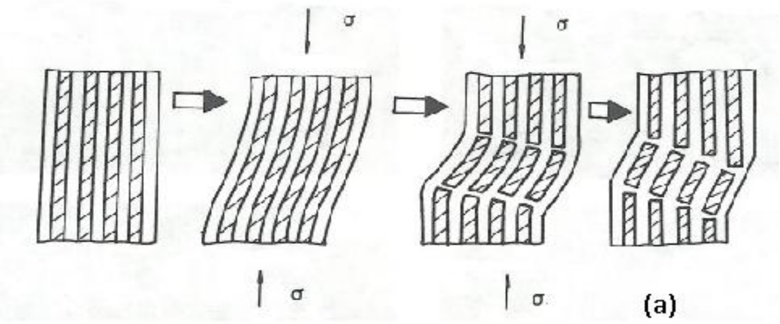

[26]

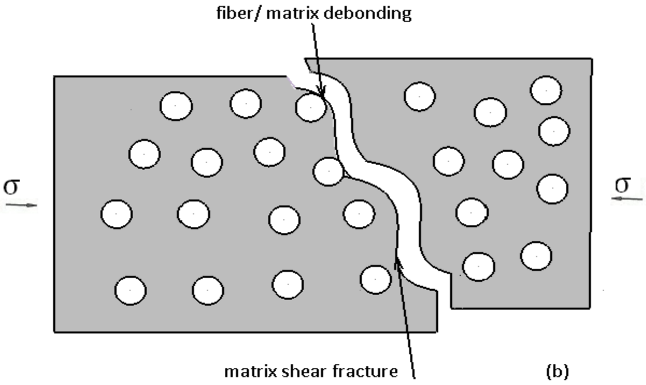

Fig 2-12 Failure mechanisms under compressive loading

The fibre/matrix bonding condition also influences the failure mechanisms of composites. Fig 2-13 shows a set of composites with different bonding conditions under transverse tensile loading. In the case of poor bonding (Fig 2-13(a)), fibre completely separates from matrix; for intermediate bonding shown in Fig 2-13 (b), both matrix fracture and fibre/matrix debonding occur; an extremely good fibre/matrix bonding could lead to longitudinal fracture of matrix (Fig 2-13 (c)).

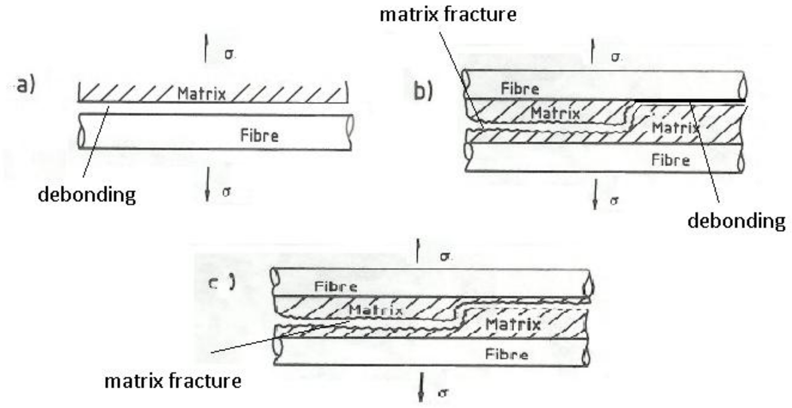

Fig 2-13 Bonding condition effects on Failure mechanisms under transverse tensile loading

Several failure theories have been developed to predict failure of fibre reinforced layers. The failure theories are generally based on the normal and shear strengths of a unidirectional lamina. The maximum stress theory and the maximum strain theory are based upon the physics of failure mechanisms. Tsai-

Hill failure theory and Tsai-Wu failure theory provide mathematical expressions which attempt to provide better corrections between experiments and physical failure theories [4].

The maximum stress failure theory assumes that failure occurs when any individual stress component along the principal material axis exceeds its respective limiting values. The maximum strain failure theory assumes that failure occurs when any individual strain component along the principal material axis overcomes that of the ultimate strain in that direction.

The two theories give different results, because the local strains in a lamina include the Poisson’s ratio. For both the maximum stress failure theory and the maximum strain failure theory, any component of stress or strain does not interact with each other. Experimental observations showed that interactions among the components can influence the failure of the material [27]. Therefore, some interaction theories were developed; Tsai-Hill failure theory and The Tsai-Wu failure theory are considered representative and widely used [28].

For fibre reinforced composites, Tsai-Hill failure theory assumes that the failure of each layer occurs when the value of TH (Equation 2.31) is equal to or greater than one [4].

$$\mathrm{TH} = \mathrm{A}_1\sigma_1^2 + \mathrm{A}_2\sigma_2^2 - \mathrm{A}_3\sigma_1\sigma_2 + \mathrm{A}_4\tau_{12}^2 \qquad [2.31]$$

Where:

σ_1, σ_2, τ_{12} are the applied stresses;

$\mathrm{A}_1 = \mathrm{A}_3 = ((\sigma_1)_{\mathrm{ult}})^{-2}$,$\mathrm{A}_2 = ((\sigma_2)_{\mathrm{ult}})^{-2}$, $\mathrm{A}_4 = ((\tau_{12})_{\mathrm{ult}})^{-2}$. $(\sigma_1)_{\mathrm{ult}}$, $(\sigma_2)_{\mathrm{ult}}$ and $(\tau_{12})_{\mathrm{ult}}$ are the uniaxial material strength parameters parallel and perpendicular to fibres, and in shear.

For fibre reinforced composites, the Tsai-Wu failure theory assumes that the failure of each layer occurs when the value of TW (Equation 2.32) is equal to or greater than one [4].

$$\mathrm{TW} = \mathrm{R}_1\sigma_1 + \mathrm{R}_{11}\sigma_1^2 + \mathrm{R}_2\sigma_2 + \mathrm{R}_{22}\sigma_2^2 + \mathrm{R}_6\tau_{12} + \mathrm{R}_{66}\tau_{12}^2 + 2\mathrm{R}_{12}\sigma_1\sigma_2 \quad [2.32[$$

Where:

$$\mathrm{R}_1 = \frac{1}{(\sigma_1^{\mathrm{T}})_{\mathrm{ult}}} - \frac{1}{(\sigma_1^{\mathrm{C}})_{\mathrm{ult}}};\ \mathrm{R}_2 = \frac{1}{(\sigma_2^{\mathrm{T}})_{\mathrm{ult}}} - \frac{1}{(\sigma_2^{\mathrm{C}})_{\mathrm{ult}}};\ \mathrm{R}_6 = \frac{1}{(\tau_{12}^{\mathrm{T}})_{\mathrm{ult}}} - \frac{1}{(\tau_{12}^{\mathrm{C}})_{\mathrm{ult}}} = 0;$$

$$\mathrm{R}_{11} = \frac{1}{(\sigma_1^{\mathrm{T}})_{\mathrm{ult}}(\sigma_1^{\mathrm{C}})_{\mathrm{ult}}};\ \mathrm{R}_{22} = \frac{1}{(\sigma_2^{\mathrm{T}})_{\mathrm{ult}}(\sigma_2^{\mathrm{C}})_{\mathrm{ult}}};\ \mathrm{R}_{66} = \frac{1}{(\tau_{12}^{\mathrm{T}})_{\mathrm{ult}}(\tau_{12}^{\mathrm{C}})_{\mathrm{ult}}};$$

$$\mathrm{R}_{12} = \frac{1}{2\sigma_e^2}[1 - (\mathrm{R}_1 + \mathrm{R}_2)\sigma_e - (\mathrm{R}_{11} + \mathrm{R}_{22})\sigma_e^2];$$

$(\sigma_1^{\mathrm{T}})_{\mathrm{ult}}$, $(\sigma_2^{\mathrm{T}})_{\mathrm{ult}}$, $(\tau_{12}^{\mathrm{T}})_{\mathrm{ult}}$ and $(\sigma_1^{\mathrm{C}})_{\mathrm{ult}}$, $(\sigma_2^{\mathrm{C}})_{\mathrm{ult}}$, $(\tau_{12}^{\mathrm{C}})_{\mathrm{ult}}$ are the quantities of lamina longitudinal, transverse and shear strengths in tension and compression, respectively.

σ_e is the equal tensile load along the longitudinal and transverse direction, at which the lamina fails.

σ_1, σ_2, τ_{12} are the applied stresses.

Unlike the maximum strain and maximum stress failure theories, the Tsai-Hill failure theory and Tsai-Wu failure theory consider the interaction among the stress components. The Tsai-Hill failure theory does not distinguish between the compressive strengths and tensile strengths in its equation, which leads to underestimating the failure stress, because generally the transverse tensile strength is much less than its transverse compressive strength [29].

The maximum stress and strain failure theories are more applicable when brittle behavior is predominant; whereas, the Tsai-Hill and Tsai-Wu failure theories are more applicable when ductile behaviour under shear or compression loading is predominant [28]. Metal matrix composite materials usually exhibit between brittle and ductile, thus it is better to combine failure criteria and choose the most conservative envelope to predict failure of composites.

2.3 Fracture Mechanics

2.3.1 Basic Modes of Fracture

There are three basic modes of fracture subjected to three different loadings, shown in Fig 2-14.

- Mode Ⅰ - Opening mode (tensile stress normal to the plane of the crack);
- Mode Ⅱ－ Sliding mode (in-plane shear parallel to the crack);
- Mode Ⅲ－ Tearing mode (out of plane shear normal to the crack).

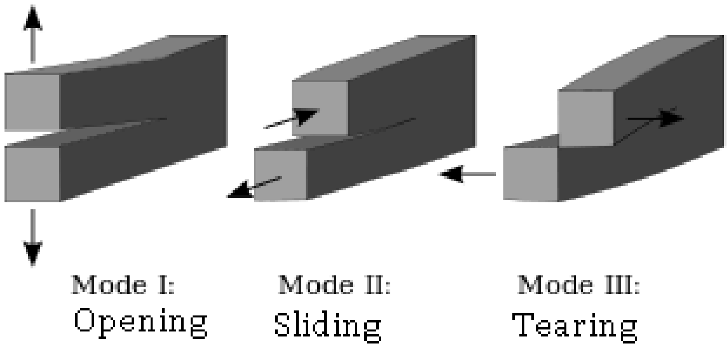

Fig 2-14 Basic modes of fracture [1]

This thesis focuses on the Mode Ⅰ fracture, which is the most important mode, since it is the predominant mode in many practical cases [30]. All the fracture toughness parameters obtained from tests in this thesis are based on the assumption of Mode Ⅰ fracture.

The equations in this chapter were mainly referred to reference 1 and reference 30.

2.3.2 Development of Fracture Mechanics

A.A. Griffith is the commonly accepted first pioneer to successfully analyze fracture-dominant problems. In the 1920s, he formulated the now well-known concept that an existing crack will propagate if the total energy of the system is thereby lowered [30]. He further introduced an energy balance approach that has become one of the most famous achievements in materials science. His theory has made it possible to estimate the theoretical strength of brittle materials and supply the correct relationship between fracture strength and crack size.

In the 1950s, Irwin modified and developed the energy approach: the strain energy release rate $\mathcal{G}$ is defined as the energy available per increment of crack extension and per unit thickness for a linear elastic material [30]. When $\mathcal{G}$ reaches the critical strain energy release rate $\mathcal{G}_c$, fracture occurs. For an infinite plate with a crack under a remote tensile stress, shown in Fig 2-15, $\mathcal{G}$ is

$$\mathcal{G} = \frac{\pi\sigma^2 a}{\mathbf{E'}} \quad [2.33]$$

Where:

$\mathrm{E'}$ is 'apparent' elastic modulus: for plane stress, $\mathrm{E'} = \mathrm{E}$; for plane strain, $\mathrm{E'} = \frac{\mathrm{E}}{1-\vartheta^2}$; E is the Young's modulus,

ϑ is the Poisson's ratio; σ is the applied stress; 2a is the crack length.

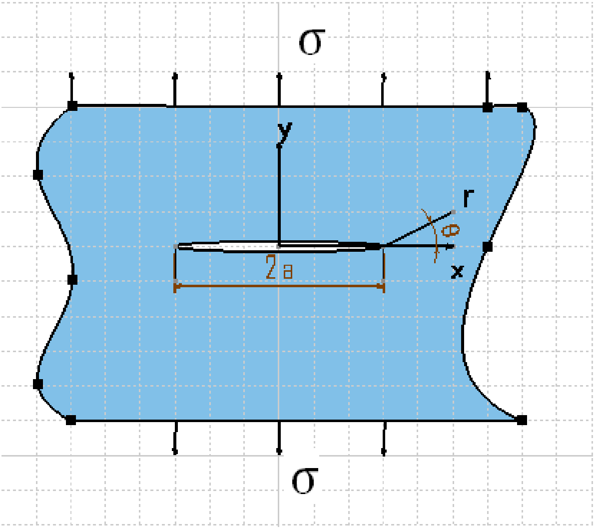

Fig 2-15 A through-thickness crack in a loaded infinite plate

Irwin also introduced the stress intensity approach (K). K is a quantity which gives the magnitude of elastic crack tip stress field. For an infinite plate with a crack under a remote tensile stress, Fig 2-16 shows the elastic stress components near the crack tip, the stress components are expressed as:

$$\sigma_x = \frac{K_1}{\sqrt{2\pi r}}\left(1 - \sin\left(\frac{\theta}{2}\right)\sin\left(\frac{3\theta}{2}\right)\right)\cos\frac{\theta}{2} \qquad [2.34]$$

$$\sigma_y = \frac{K_1}{\sqrt{2\pi r}}\left(1 + \sin\left(\frac{\theta}{2}\right)\sin\left(\frac{3\theta}{2}\right)\right)\cos\frac{\theta}{2} \qquad [2.35]$$

Where:

θ, r are defined as a polar coordinates near the crack tip; K_I is the stress intensity factor.

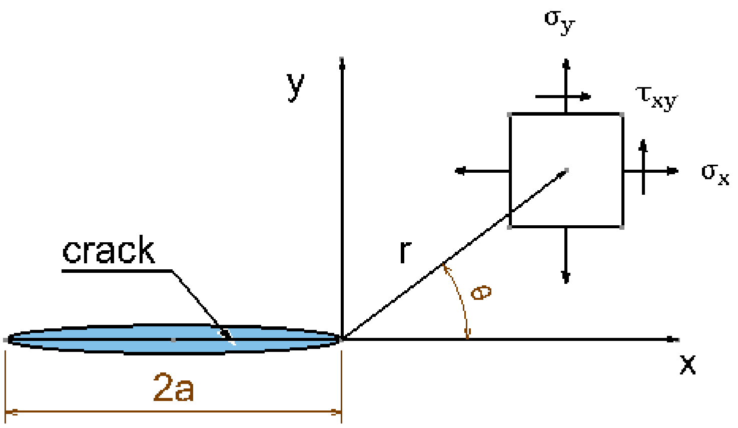

Fig 2-16 Definition of the coordinate axis ahead of a crack [1]

The equations show that the stress components are consisted of stress intensity factor K_I and geometry factor. The stress intensity factor K_I can be expressed as:

$$K_I = \sigma\sqrt{\pi a} \qquad [2.36]$$

Where:

σ is the applied remote tensile stress; a is the half crack length.

When fracture occurs, the stress intensity factor reaches its critical value, K_c, but this value is different for different thickness specimens of the same material, because the stress state near the crack changes with specimen thickness B until the thickness exceeds some minimum critical thickness. The effect of specimen thickness on stress state is shown in Fig 2-17 [31].

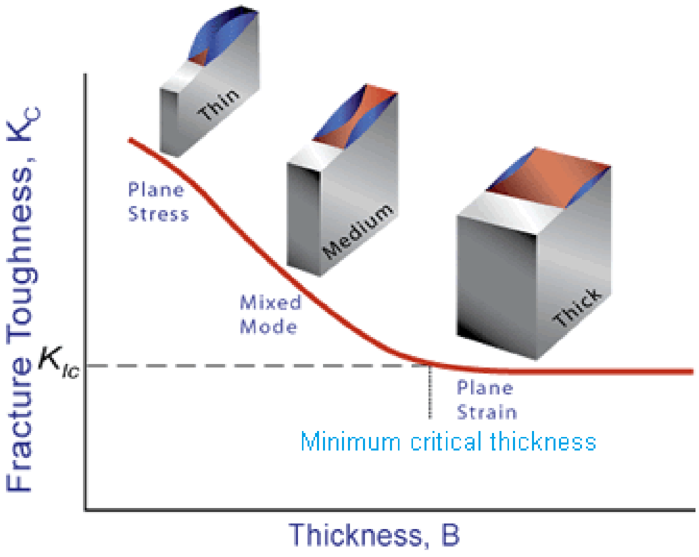

Fig 2-17 The effect of thickness on K_c and stress state [31]

Once the specimens thickness exceeds the minimum critical thickness, the critical stress intensity factor K_c, becomes relatively constant. This constant value is called plane strain fracture toughness K_{Ic}, a material property characterizes resistance to fracture.

Comparing Equation 2.33 and Equation 2.36, for linear elastic material, the relationship between K_I and $\mathcal{G}$ can be expressed as:

$$\mathcal{G} = \frac{K_I^2}{\mathrm{E}'} \quad [2.37]$$

This relationship is also valid for $\mathcal{G}_c$ and K_c.Thus, material property governing fracture may be described as a critical stress intensity factor K_c, or as a critical strain energy release rate $\mathcal{G}_c$. The equivalence of K and $\mathcal{G}$ paves the way for development of discipline of Linear Elastic Fracture Mechanics (LEFM). It supplies a method to determine what cracks or crack-like flaws are acceptable in a real structure under certain circumstance by testing on suitable geometry and loaded specimens.

Linear Elastic Fracture Mechanics (LEFM) can only be used to deal with limited crack tip plasticity [30]. However, Elastic-Plastic Fracture Mechanics (EPFM) significantly extends the description of fracture behaviour beyond the elastic part, combining elastic-plastic analyses and failure assessments.

In 1961, Wells derived another approach named crack tip opening displacement (CTOD), shown in Fig 2-18 , which focuses on the strains in the crack tip region instead of the stresses; it is plastic strain in the crack tip that controls fracture. This approach could be used to define the onset of fracture; therefore it can be used to qualify the materials for a certain application. In 1966, Burdekin and Stone, by applying the Dugdale strip yield model, provided the basic expression for CTOD for an infinite plate under a remote tensile load [30]

$$\delta_t = \frac{8\sigma_{ys}a}{\pi E'} \ln \sec \frac{\pi\sigma}{2\sigma_{ys}} \quad [2.38]$$

Where:

σ is the applied tensile stress; a is half crack length; $\mathbf{E}'$ is the 'apparent' elastic modulus; σ_{ys} is 0.2% yield strength.

If $\sigma/\sigma_{ys} \ll 1$, as the case for linear elastic fracture mechanics, then Equation 2.38 can be written as [30]:

$$\delta_t = \frac{\pi\sigma^2 a}{E'\sigma_{ys}} = \frac{K_1^2}{E'\sigma_{ys}} \qquad [2.39]$$

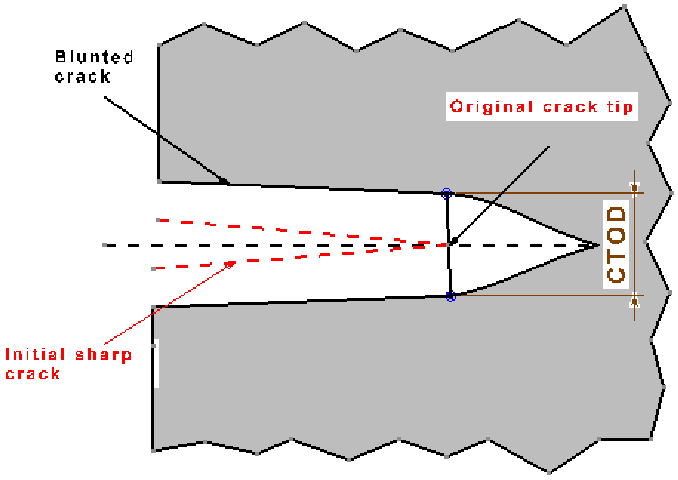

Fig 2-18 Crack tip opening displacement CTOD [30]

In 1968, Rice introduced another fracture parameter called $\mathcal{J}$-integral which enjoys great success. Rice formulated $\mathcal{J}$ as a path-independent line integral (see Appendix E), the value of $\mathcal{J}$ equals to the decrease in potential energy per increment of crack extension in linear or nonlinear elastic material [30].

$$\mathcal{J} = -\left(\frac{\partial U_p}{\partial a}\right) \quad [2.40]$$

Where:

U_p is the potential energy of the plate and the loading system.

Critical $\mathcal{J}$ can be used as a fracture toughness parameter both for linear elastic behaviour materials and elastic-plastic behaviour materials. For linear elastic case, by the definition, $\mathcal{J}$ is equal to $\mathcal{G}$,

$$\mathcal{J} = \mathcal{G} \quad [2.41]$$

Comparing Equation 2.37 and Equation 2.41, for liner elastic case, the relationship between K_I, $\mathcal{J}$ and $\mathcal{G}$ can be expressed as [30];

$$\mathcal{J} = \mathcal{G} = \frac{K_I^2}{E'} = \sigma_{ys}\delta_t \quad [2.42]$$

2.4 Fracture Toughness Tests

A fracture toughness test measures the resistance of a material to crack extension. The test may be illustrated with a single value of fracture toughness or a resistance curve [1].

A variety of organizations around the world have published standardized procedures for fracture toughness tests, including the American Society for Testing and Materials (ASTM), the British Standards Institution (BSI), and the International Institute of Standards (ISO). The procedures are broadly consistent with each other and differ only in minor details [1].

ASTM 1820 and BS 7448, which are widely applied for fracture toughness tests, combine different types of fracture toughness parameter evolutions into a single set of test rules to minimize the risk of invalid test results due to unexpected material behaviour [30].

There are three fracture toughness parameters that characterize the resistance of a material to crack extension: plane strain fracture toughness K_{Ic}, critical crack tip opening displacement $\mathrm{CTOD_c}$ and critical $\mathcal{J}$-integral $\mathcal{J}_{\mathrm{Ic}}$.

2.4.1 Plane Strain Fracture Toughness K_{Ic} Test

Stress intensity factor K may be a proper fracture parameter, if the behaviour of the material is in a linear elastic manner before failure. The stress intensity factor Equation 2.36 is strictly valid only for an infinite plate. The geometry of finite size specimens affects the crack tip stress field. So, the stress intensity factor equation has to be modified by the addition of correction factors to solve practical problems [30].

$$K_I = \mathrm{\sigma}\sqrt{\mathrm{\pi a_0}} \times f(\frac{\mathrm{a_0}}{\mathrm{W}}) \qquad [2.43]\ [30]$$

Where:

$f(\frac{a_0}{W})$ is a geometric correction factor, obtained by stress analysis; a_0 is the initial crack length, W is the specimen width, a_0 and W are illustrated in Fig 2-19 for a straight notched compact tension specimen.

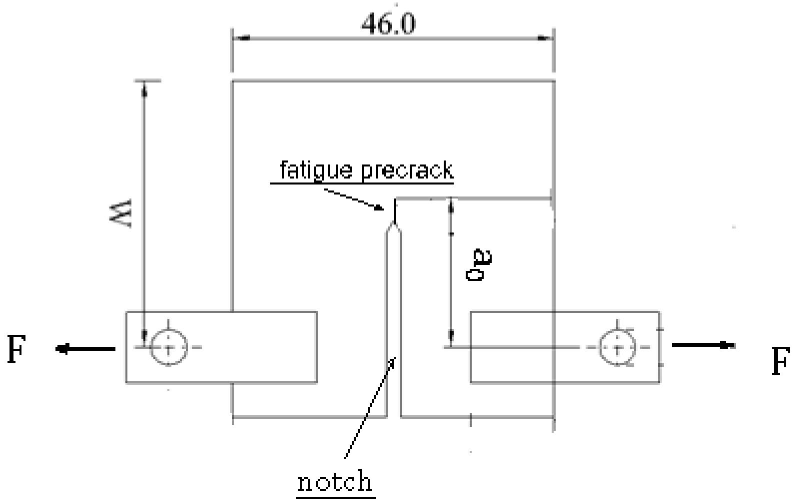

Fig 2-19 Geometry of a straight notched compact tension specimen

For compact tension specimen (CT), the stress intensity factor is:

$$K_I = \frac{F}{BW^{0.5}} \times f\left(\frac{a_0}{W}\right) \quad [2.44]\ [30]$$

Where:

a_0 is the initial crack length, W is the specimen width; B is the specimen thickness; F is the applied force, shown in Fig 2-19.

$f\left(\frac{a_0}{W}\right)$ is the geometric correction factor for straight notched compact tension specimens:

$$f(\frac{a_0}{W}) = \frac{\left(2+\frac{a_0}{W}\right)[0.886+4.64\frac{a_0}{W}-13.32\left(\frac{a_0}{W}\right)^2+14.72\left(\frac{a_0}{W}\right)^3-5.6\left(\frac{a_0}{W}\right)^4]}{(1-\frac{a_0}{W})^{1.5}} \quad [32]$$

After analysis of Load-Displacement record, a provisional critical stress intensity factor K_Q can be calculated. But the provisional value should be analyzed to ensure it is valid for plane strain fracture toughness K_{Ic}, which can be considered as a parameter characterizing the crack resistance of a material.

The validity criteria for plane strain fracture toughness K_{Ic} are [32]:

(1) The dimensions of the specimens a_0, B and (W-a_0), should be greater than the geometry factor 2.5$(\frac{K_Q}{\sigma_{\mathrm{ys}}})^2$.

Where:

K_Q is the provisional value of plane strain fracture toughness; σ_{ys} is 0.2% yield strength of the material.

This criterion is to ensure the stress state near crack tip is plane strain condition during testing.

(2) The original crack length should lie between the range $0.45 \leq \frac{\mathrm{a}_0}{\mathrm{W}} \leq 0.55$.

This criterion is to ensure the geometric correction factors are applicable.

(3) The ratio of $\mathrm{F}_{\mathrm{max}}/\mathrm{F}_{\mathrm{Q}}$ should be less than 1.10.

Where:

$\mathrm{F}_{\mathrm{max}}$ is the maximum applied force before fracture;

F_{Q} is the provisional force for the calculation of provisional plane-strain fracture toughness, the method to determine F_{Q} is illustrated in Appendix C.

This criterion is to ensure the specimen behaves considerably elastic, so that the test method is applicable.

(4) The plane of the fatigue precrack and 2% crack extension must always be within $\pm 10^{\circ}$ of the plane of the starter notch [33].

If a valid K_{Ic} value cannot be derived since the criteria are not met, the fracture toughness of the material could be interpreted by CTOD_c or $\mathcal{J}_{Ic}$.

2.4.2 Critical Crack Tip Opening Displacement CTOD_c Test

Critical crack tip opening displacement CTOD_c can be used to characterize the resistance of a material to crack initiation and early crack extension. It also serves as a basis for displacement controlled fracture criteria.

2.4.2.1 Standard Test Method

The standard test method is based on ASTM E 1820 and BS7448, and the principle is demonstrated as following:

For a traditional measurement method, it is impossible or difficult to directly measure $\mathrm{CTOD_c}$ at the actual crack tip; instead a clip gauge is used to measure the crack tip opening displacement $\mathrm{V_g}$ at or near the specimen surface.

A schematic Load-displacement curve 'OAF' is shown in Fig 2-20. A line through point 'F' with the same slope as the tangent of line 'OA' is drawn, the clip gauge displacement $\mathrm{V_g}$ is separated into an elastic part $\mathrm{V_{el}}$ and a plastic part $\mathrm{V_{pl}}$. Point 'F' is the onset of fracture, line 'OA' is the elastic load-displacement line.

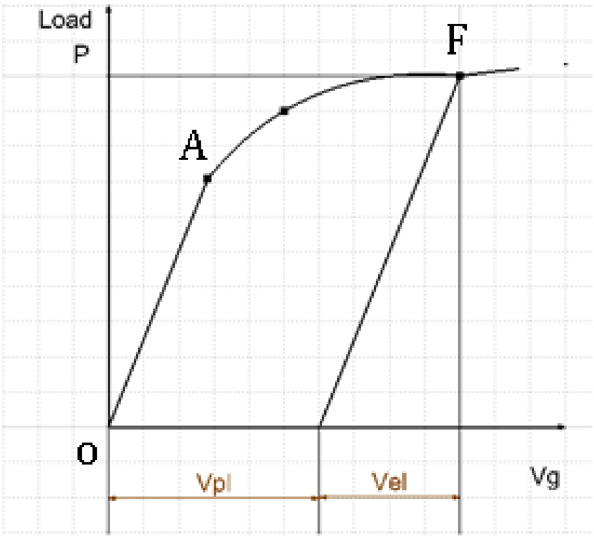

Fig 2-20 Separate $\mathrm{V_g}$ into elastic part $\mathrm{V_{el}}$ and a plastic part $\mathrm{V_{pl}}$

For finite plate, the elastic part $\mathrm{V_{el}}$ contribution to δ_t is:

$$\delta_{el} = \frac{\sigma^2 \pi a_0}{\lambda E' \sigma_{ys}} = \frac{K_I^2}{\lambda E' \sigma_{ys}} \quad [2.45]$$

Where:

λ is the stress state factor near the crack tip area, λ =2 for plane strain, or λ =1 for plane stress; E' is the 'apparent' elastic modulus; σ_{ys} is 0.2% yield strength of the material; K_I is the stress intensity factor.

Fig 2-21 shows the contribution of plastic part $\mathrm{V_{pl}}$ to δ_t, the ligament b=W-a_0 acts as a plastic hinge; this implies a rotation point within the ligament at some distance r· b. δ_{pl} can be expressed as:

$$\delta_{pl} = \frac{r \cdot b}{r \cdot b + a_0 + z} V_{pl} \quad [2.46]$$

Where:

z is distance corrects for the use of knife edges; V_{pl} is the plastic part of clip gauge displacement, defined in Fig 2-20;

r is the rotation factor, 0.46 for CT specimen [30]; b is the effective width, equals to (W-a_0).

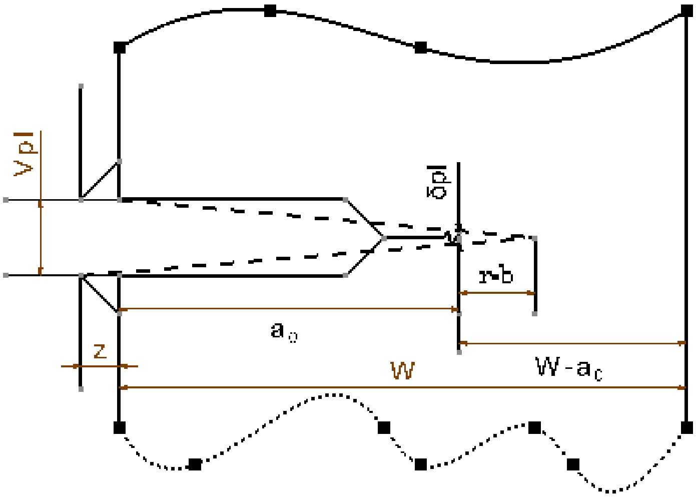

Fig 2-21 Relation between V_{pl} and δ_{pl} [30]

Therefore, according to load versus clip gauge displacement curve, combining Equation 2.45 and Equation 2.46, the equation to calculate δ_t is:

$$\delta_t = \delta_{el} + \delta_{pl} = \frac{K_I^2}{\lambda E' \sigma_{ys}} + \frac{r \cdot b}{r \cdot b + a_0 + z} V_{pl} \quad [2.47]$$

2.4.2.2 Schwalbe CTOD (δ_5)

Recently, with the development of measurement technology, δ_5 was introduced as an experimental method for measuring Crack Tip Opening Displacement (CTOD) [34]. Several experimental results have confirmed that δ_5 can be used as an operational testing method of CTOD [34].

By this method, CTOD is measured on one side surface of test specimens at points located 2.5 mm each side from the tip of the fatigue precrack or notch, so δ_5 is measured locally next to the crack tip.

2.4.3 Critical $\mathcal{J}$-integral $\mathcal{J}_{Ic}$ test

2.4.3.1. The Original $\mathcal{J}_{Ic}$ Test Method

The original $\mathcal{J}_{Ic}$ test method was published by Begley and Lands in 1971, the method is based on the definition of $\mathcal{J}$ as $-\frac{dU_p}{da}$;

$$\mathcal{J} = -\left(\frac{dU_p}{da}\right) = \left(\frac{d(F-U_1)}{da}\right) \quad [2.48]$$

Where:

U_p= the potential energy of the plate and loading system; U_1=the strain energy stored in the plate; F=the work done by external force;

For crack extension under fixed grip condition, the work performed by the loading system is zero, so

$$\mathcal{J} = -\left(\frac{dU_p}{da}\right)_{\mathbf{v}} = \left(\frac{d(F-U_1)}{da}\right) = -\left(\frac{dU_1}{da}\right)_{\mathbf{v}} \quad [2.49]$$

The original $\mathcal{J}_{Ic}$ test method requires graphical assessment of $-\left(\frac{dU_1}{da}\right)_{\mathbf{v}}$. The method is demonstrated as follow [30]:

(1) Tests are conducted on a number of precracked specimens with different crack lengths (a_1, a_2 and a_3), shadow areas under the load-displacement curves represent the energy per unit thickness, U_1 **(**see Fig 2-22).

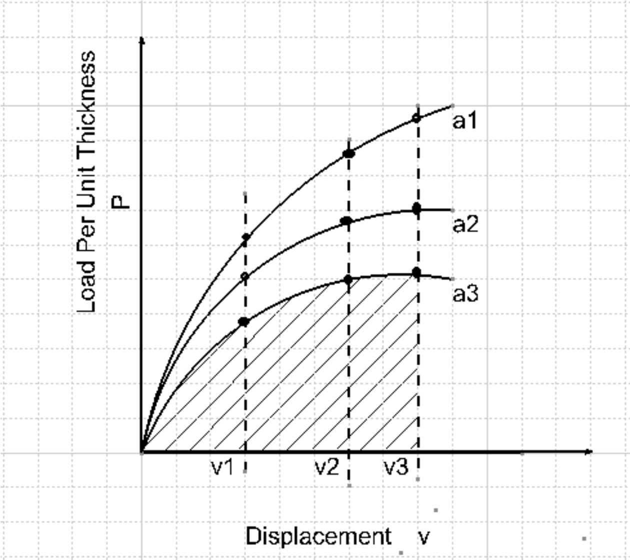

Fig 2-22 P-v curves for three specimens with different crack lengths

(2) Fig 2-23 shows that U_1 is plotted as a function of crack length for several constant displacements.

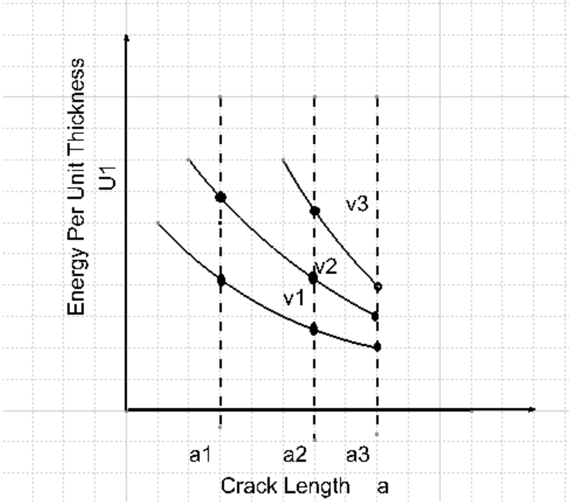

Fig 2-23 U_1-a curves for three specimens for constant displacements

(3) The negative slopes of the U_1-a curves, $-(\frac{\partial U_1}{\partial a})_v$, are plotted against displacement for each specimens with different crack length. According to

the definition of $\mathcal{J}$-integral, Fig 2-24 in fact gives the $\mathcal{J}-\mathrm{v}$ curve for particular crack lengths.

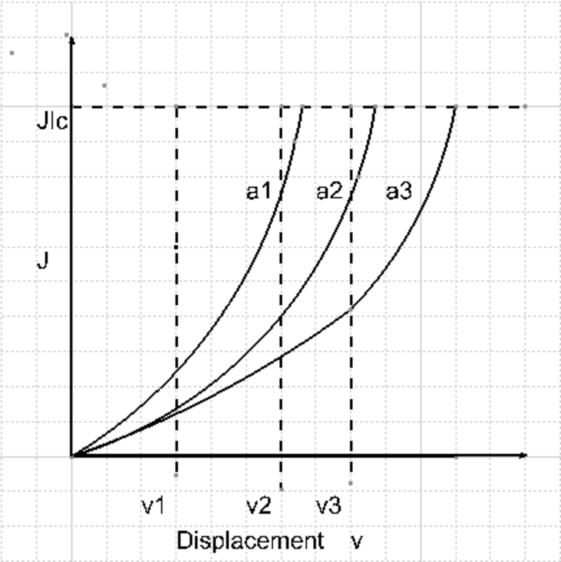

Fig 2-24 J-v curves and determination of $\mathcal{J}_{\mathrm{Ic}}$ for each specimen

(4) The displacement v at the onset of crack for each specimen can be obtained from the P-v curves (Fig 2-22), so the critical $\mathcal{J}$-integral, $\mathcal{J}_{Ic}$, can be obtained from the $\mathcal{J}-\mathrm{v}$ curve at the displacement of onset crack.

The graphical procedure requires extensive data processing and replotting to obtain the $\mathcal{J}-\mathrm{v}$ curve, and it is easy to introduce errors. However, this method directly uses the energy definition of $\mathcal{J}_{Ic}$, and remains as a reference to check more recent developments.

2.4.3.2. Current $\mathcal{J}_{Ic}$ Test Method

In 1973, Rice contributed simple expressions for $\mathcal{J}$ integral, so in certain cases, it is possible to determine $\mathcal{J}$ from the load displacement curve of a single specimen. Both ASTM E 1820 and BS 7448 supply the procedure to measure critical $\mathcal{J}$-integral, $\mathcal{J}_{Ic}$, at fracture instability or near the onset of ductile crack extension.

A schematic Load-displacement curve ‘OAF’ is shown in Fig 2-25. A line through point ‘F’ with the same slope as the tangent of line ‘OA’ is drawn, the displacement V is separated into an elastic part $\mathrm{V_{el}}$ and a plastic part $\mathrm{V_{pl}}$ as shown in Fig 2-25. Point 'F' is the onset of fracture, line 'OA' is the elastic load-displacement line.

$$\mathrm{V} = \mathrm{V_{pl}} + \mathrm{V_{el}} \quad [2.50]$$

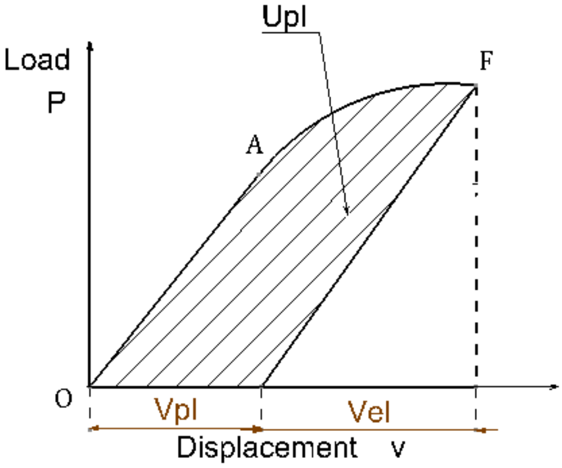

Fig 2-25 The plastic work $\mathrm{U_{pl}}$

Base on energy approach Rice formulated $\mathcal{J}$ as a path-independent line integral with the value equals to the decrease in potential energy per increment of crack extension [30]. So, $\mathcal{J}$-integral can be written as:

$$\mathcal{J} = \frac{1}{\mathrm{B}}\int_0^{\mathrm{P}}\left(\frac{\partial \mathrm{v}}{\partial \mathrm{a}}\right)_{\mathrm{P}} \mathrm{dP} = \frac{1}{\mathrm{B}}\int_0^{\mathrm{P}}\left(\frac{\partial \mathrm{v_{pl}}}{\partial \mathrm{a}}\right)_{\mathrm{P}} \mathrm{dP} + \frac{1}{\mathrm{B}}\int_0^{\mathrm{P}}\left(\frac{\partial \mathrm{v_{el}}}{\partial \mathrm{a}}\right)_{\mathrm{P}} \mathrm{dP} = \mathcal{J}_{\mathrm{pl}} + \mathcal{J}_{\mathrm{el}} \quad [2.51]$$

For the energy release rate definition of $\mathcal{J}$ and $\mathcal{G}$, combining Equation 2.37,

$$\mathcal{J}_{\mathrm{el}} = \mathcal{G} = \frac{K_I^2}{\mathrm{E}'} \quad [2.52]$$

Where:

K_I is the stress intensity factor which can be calculated using Equation 2.44.

For plastic part of $\mathcal{J}$ can be calculated by a simplified method:

$$\mathcal{J}_{\mathrm{pl}} = \frac{\eta U_{\mathrm{pl}}}{Bb} \quad [2.53]$$

Where:

η is plastic work factor, equals to 2.0 for bend specimen; equals to 2+0.522$(1 - \frac{a_0}{W})$ for compact specimen;

U_{pl} is the plastic work, equals to the shadow area under load-displacement curve, shown in Fig 2-25;

B is the thickness of the specimen; b is the effective width, equals to (W-a_0).

Therefore, combining Equation 2.51 and Equation 2.52, the equation to calculate $\mathcal{J}$ is:

$$\mathcal{J} = \mathcal{J}_{\mathrm{pl}} + \mathcal{J}_{\mathrm{el}} = \frac{K_1^2}{\mathbf{E'}} + \frac{\eta U_{\mathrm{pl}}}{Bb} \quad [2.54]$$

But the provisional value obtained from Equation 2.54 should be analyzed to ensure it is valid for critical $\mathcal{J}$-integral, $\mathcal{J}_{Ic}$, which can be considered as a parameter determining the crack resistance of a material.

Theoretical and experimental investigations have shown that the minimum critical thickness demand for valid $\mathcal{J}_{Ic}$ is [35]:

$$B_{\min} = 25\frac{\mathcal{J}_Q}{\sigma_{ys}} \qquad [2.55]$$

Where:

$\mathcal{J}_Q$= provisional value of critical $\mathcal{J}$-integral; σ_{ys} is 0.2% yield strength of the material;

Stress analysis has shown that the ductile initiation toughness would be independent of thickness as long as the plane strain state prevails in the centre of the specimen [35]. Therefore, the minimum critical thickness demands for valid $\mathcal{J}_{Ic}$ is much smaller than that for plane strain fracture toughness K_{Ic} for the same material.

2.5 Fracture Toughness Tests on Thin Specimens

Thin materials have wide applications such as pressure vessels, vehicles and aircrafts, so the fracture toughness on thin materials has to be tested. However, the thin specimens are subject to out-of-plane displacement, which leads to combined Mode Ⅰ and Mode Ⅲ displacement of the crack [1], as shown in Fig 2-26.

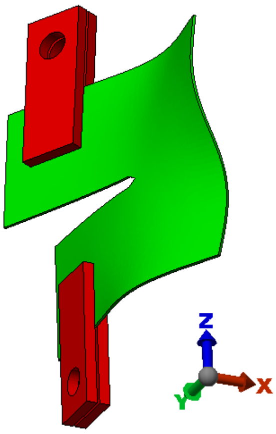

Fig 2-26 A typical out-of-plane buckling

Some efforts have been made to avoid buckle during the loading; one favourite approach is to fix plates on each side of the specimen to prevent out-of-plane displacement. Castrodeza et al. applied the anti-buckling plates to avoid the specimen buckling when testing on 1.42 mm thick CT specimens made of fibre metal composites [36]; A.R. Shahani applied the same method when testing on 1.25, 1.64 and 4.06 mm thick CT specimens [37]. The plates are shown in Fig 2-27 [37]. R.A. Mirshams used a specially designed fixture to hold thin samples for fracture toughness tests. The thicknesses of specimens were 0.22 mm for pure nano nickel and 0.35mm for carbon doped nano nickel. The special fixture is shown in Fig 2-28 [38].

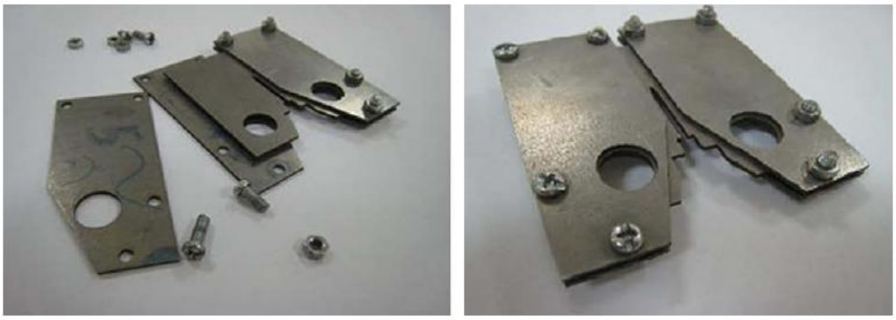

Fig 2-27 Anti-bulking plates around CT specimen [37]

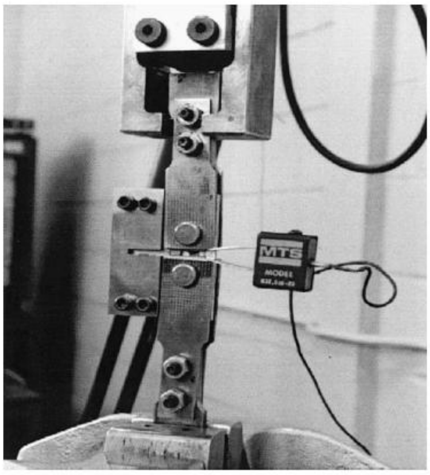

Fig 2-28 Special fixture and setup for thin sample [38]

3 Experimental Method

3.1 General

Up to now, there are no specific fracture toughness test standards for metal matrix composites (MMC), thus ASTM 1820 and BS 7448, which are supposed to be applied to metallic materials, are normally applied. These standard test procedures for the plane strain fracture toughness of metal materials are suitable for metal matrix composites [39]; the standard test procedures should be modified to obtain two widely accepted elastic-plastic parameters $\mathcal{J}$ -Integral and crack tip opening displacement CTOD [40].

Hence ASTM 1820 and BS 7448 were applied for all the fracture toughness tests in this thesis.

3.2 Specimen

3.2.1 Geometry and Materials

Middle tension (MT) specimen is a preferred choice for fracture toughness test for thin sheet material by ASTM, but the specimens in this thesis were sponsored by a British company, they had chosen straight notch compact tensile specimens (CT) for fracture toughness tests. To avoid crack and collapse of the edges of the holes when the clevis pins were through the thin composite material, 2 mm thick aluminium tabs were bonded to each side of the sample and the hole for the clevis pin was made in thicker ductile material. The sample geometry is shown in Fig 3-1.

The crack plane orientation was L-T [42] (see Appendix B). For all the composite specimens, titanium based alloys were reinforced uniaxially with silicon carbide fibres, and the crack propagation direction was parallel to the fibre direction.

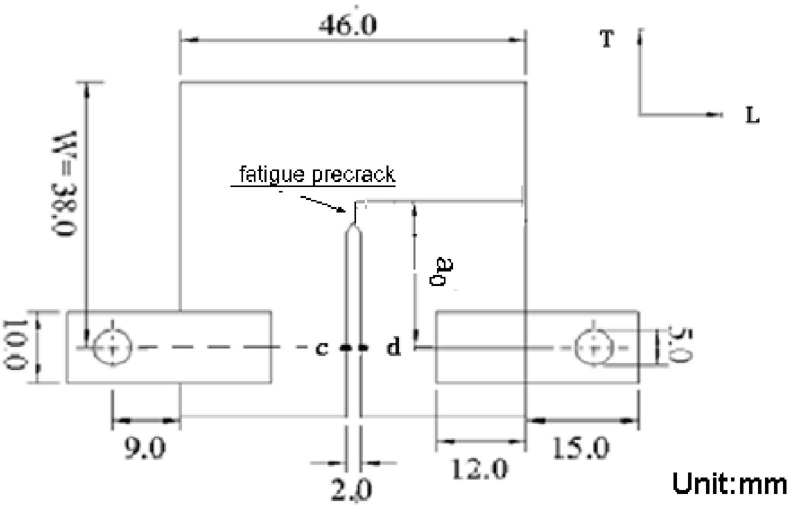

Fig 3-1 Fracture toughness test sample geometry

There were five types of materials: Tiβ21-S reinforced with high volume SiC fibre (series 2 and 3); Ti-Al3-V2.5 reinforced with low volume SiC fibre (series 5), β21-S+Ti_{cp} reinforced with medium volume SiC fibre (series 6), monolithic Tiβ21-S alloy (series 10) and Ti-Al3-V2.5 alloy (series 11).

All three kinds of composites with three fibre layers were fabricated by applying a foil-fibre-foil (FFF) technique. The thickness of each layer for the composites was within 150-186 μm. A representative cross-section image of Tiβ21-S/SiC (x 90) is shown in Fig 3-2, it shows that the circular fibres were arranged in an irregular hexagonal array.

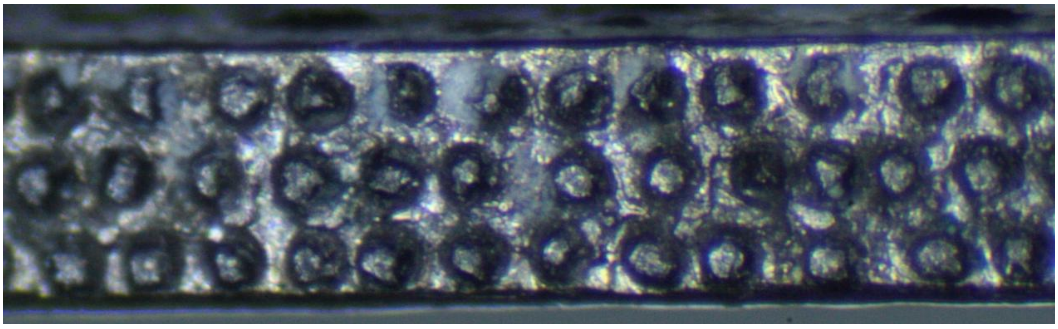

Fig 3-2 The cross-section surface image of the composite

The method to measure fibre volume fraction of the composites was shown as Equation 3.1, the fibre volume fraction of the composites were listed in Tab 3-1.

$$c_{\mathrm{f}} = \frac{\mathrm{N} \times \pi \times \mathrm{R}^2}{4 \times \mathrm{A}} \quad [3.1]$$

Where:

N: the number of fibres in a representative region of the surface of the composite.

R: the average diameter of the fibres.

A: the area of the chosen representative region.

Tab 3-1 Fibre volume fractions of the composites

Material	Tiβ21-S/SiC	Ti-Al3-V2.5/SiC	β21-S+Ti$_{cp}$/SiC
Fibre Volume Fraction	45%	25%	35%

The tensile properties of the matrix and fibre at room temperature are summarized in Tab 3-2；

Tab 3-2 Tensile properties of the matrix and fibre materials

Material	Young's modulus (GPa)	Poisson's ratio	Shear modulus (GPa)	0.2% Yield strength（MPa）
Tiβ-21	106.5	0.31	40.65	1100
Ti-Al3-V2.5	100	0.30	38.46	500
β21-S+Ti$_{cp}$	105	0.30	40.38	1000
SiC fibre [4]	400	0.25	160.00	3496

The engineering properties of the transversely isotropic composites can be expressed in terms of the properties of the matrix and reinforcing fibres together with their proportions and geometry. By applying the Halpin-Tsai equations (Equations 2.30), the composite properties were shown in Tab 3-3.

The fibre-matrix debonding strength of the composites was assumed to be the same as the fibre/matrix debonding strength of Ti-6Al-4V/SiC. Several researches reported that the fibre-matrix debonding strength of Ti-6Al-4V/SiC was approximately 330 MPa [3, 12]. The 2-axial 0.2% yield strength of the composites was shown in Tab 3-3.

Tab 3-3 Engineering constants of composite materials in material axial

Material	Longitudinal Modulus E_1 (GPa)	Major Poisson's Ratio ϑ_{12}	2-axial Modulus E_2 (GPa)	Major Shear modulus G_{12} (GPa)	2- axial 0.2% Yield Strength (MPa)
Ti β -21/SiC	238.58	0.28	194.24	85.22	330
Ti-Al3-V2.5/SiC	175.00	0.29	142.86	59.32	330
β 21-S+Ti$_{cp}$/SiC	208.25	0.28	169.18	72.38	330

3.2.2 Specimens Precracking

The values of the fracture toughness parameters characterize the fracture resistance of a material in the presence of a sharp crack under tensile loading [43]. In order to decrease the stress intensity factor at the onset of crack instability, the machined-in notch was fatigue pre-cracked so as to produce a sharper crack tip (notch root radius≈0).

Fatigue precrackings were conducted under force control at environment temperature (21±1℃). A thermocouple was used to record the environment temperature near the specimen.

The fatigue cycling force was in a sinusoidal waveform, with the frequency of 30 HZ. The fracture toughness of different material specimens varies significantly from each other to obtain valid precrack lengths ($0.45 \leq \frac{a_0}{W} \leq 0.55$), different loads and cycles (shown in Tab 3-4) were applied on different specimens for fatigue precrack. During fatigue precrack, a microscope was used to inspect the crack length.

Tab 3-4 Loads and cycles for fatigue precrack

Plate NO.	Matrix	Fibre volume fraction	Cycles(10^3cycles)	Load(N)
2-1	Ti β 21-s	45%	7	65±50
2-2	Ti β 21-s	45%	8	65±50
2-3	Ti β 21-s	45%	8	65±50
3-1	Ti β 21-s	45%	11	65±40
3-2	Ti β 21-s	45%	14	65±40
3-3	Ti β 21-s	45%	10	65±40
5-1	Ti-Al3-V2.5	25%	50	65±40
5-2	Ti-Al3-V2.5	25%	42	65±40
5-3	Ti-Al3-V2.5	25%	45	65±40
5-4	Ti-Al3-V2.5	25%	40	65±40
5-5	Ti-Al3-V2.5	25%	50	65±40
6-1	β21-S+Ticp	35%	17	65±40
6-2	β21-S+Ticp	35%	12	65±40
6-3	β21-S+Ticp	35%	13	65±40
6-4	β21-S+Ticp	35%	12	65±40
6-5	β21-S+Ticp	35%	12	65±40

10-1	Ti β 21-s	0	43	65±40
10-2	Ti β 21-s	0	40	65±40
10-3	Ti β 21-s	0	40	65±40
11-1	Ti-Al3-V2.5	0	65	65±50
11-2	Ti-Al3-V2.5	0	62	65±50
11-3	Ti-Al3-V2.5	0	55	65±50

The specimen was carefully monitored to ensure that a symmetrical crack growth on both sides; the plane of the fatigue precrack should be parallel to the plane of the starter notch to ±10°.

3.3 Test System and Fixture

3.3.1 Test System

Both the fatigue precrackings and tension tests were conducted on an INSTRON ElectroPlus E1000 all-electric test instrument, shown in Fig 3-3, at Cranfield University. A 2 kN load cell with 1% accuracy was used during precrackings and tension tests to measure the force.

A digital 3D correlation system Q-400, an optical non-contact 3-dimensional measuring instrument, was used to record the displacement on specimen, shown in Fig 3-1. The specimen was observed by two cameras from different directions, the position of each object point was focused on a specific pixel in the camera plane. Q-400 can record the live images and full field information of the specimen, and the 3-dimentional coordinates of any surface point can be calculated. The accuracy of Q-400 was within ±1% of the reading [41].

The thickness of specimens was measured by a micrometer; all the other dimensions and crack lengths of specimens were measured by a vernier calliper.

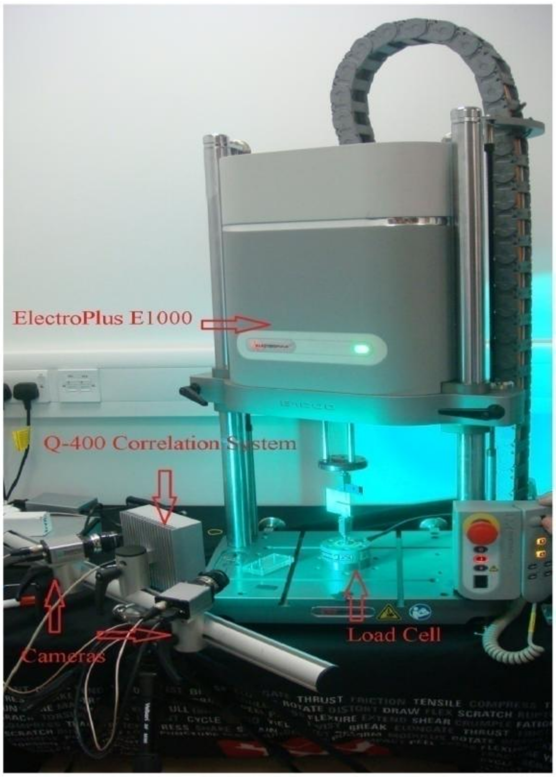

Fig 3-3 Test system

3.3.2 Loading Fixture

The loading fixture consisted of a pair of clevises and pins arrangement, shown in Fig 3-4.

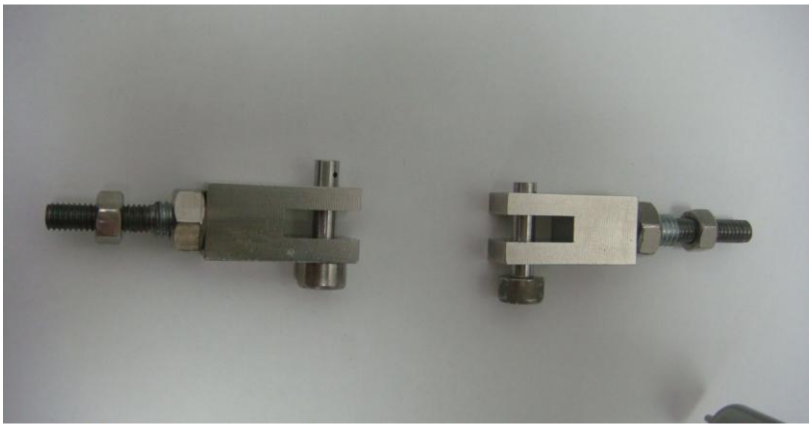

Fig 3-4 Loading fixture

3.3.3 Anti-buckling Plates

Stress and buckling analysis of the thin fracture toughness test specimens has confirmed that they are likely to buckle during testing. However, this buckling can be prevented by adding rigid plates to either side of the specimen (see Appendix A).

The fracture toughness test specimen was supported by close fitting plates as shown in Fig 3-5. These two plates were made of transparent plastic which would be helpful to inspect the initial crack and crack extension during test. The gap between the plates was 0.5 mm. The two pairs of bolts in the top and bottom sections were at slightly different heights to allow the specimen to open up as the crack propagates across the specimens.

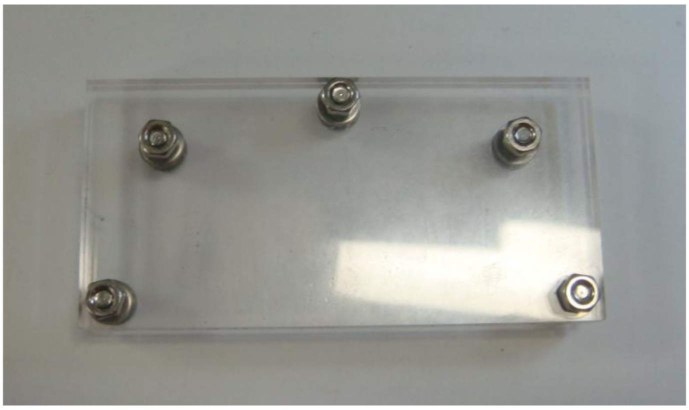

Fig 3-5 Buckling support plates for fracture toughness test specimens

3.4 Test Procedure

3.4.1.1 Dimensions Measurement

The dimensions of the specimens, effective width (W), thickness (B), total width (C) and crack length (a), were measured and recorded in Tab 3-5.

Tab 3-5 Dimensions of specimens and cracks

Unite: mm

Plate NO.	Matrix	Thickness (B)	Effective Width (W)	Total Width (C)	Crack length (a)	Initial Crack Length (a_0)
2-1	Ti β 21-s	0.456	37.76	47.83	18.07	20.13
2-2	Ti β 21-s	0.460	37.80	47.94	17.25	19.53
2-3	Ti β 21-s	0.458	37.45	47.92	18.00	20.14
3-1	Ti β 21-s	0.465	37.42	47.92	18.05	19.17
3-2	Ti β 21-s	0.458	37.23	47.93	17.39	18.80
3-3	Ti β 21-s	0.451	37.42	47.92	17.70	19.15
5-1	Ti-Al3-V2.5	0.552	37.15	47.95	17.64	20.31
5-2	Ti-Al3-V2.5	0.558	37.48	48.01	17.85	19.15
5-3	Ti-Al3-V2.5	0.557	37.50	47.95	17.10	18.50
5-4	Ti-Al3-V2.5	0.555	37.72	47.94	17.13	20.36
5-5	Ti-Al3-V2.5	0.558	37.34	47.93	17.26	21.67
6-1	β21-S+Ticp	0.522	37.98	47.96	18.19	20.37
6-2	β21-S+Ticp	0.514	37.96	47.94	18.00	19.53
6-3	β21-S+Ticp	0.516	38.15	47.90	17.10	19.29
6-4	β21-S+Ticp	0.504	37.96	47.95	18.30	20.16
6-5	β21-S+Ticp	0.512	37.95	47.85	18.30	19.18
10-1	Ti β 21-s	0.482	37.02	47.95	16.92	18.22
10-2	Ti β 21-s	0.485	38.15	48.02	17.65	18.95
10-3	Ti β 21-s	0.491	37.50	47.97	16.95	18.85
11-1	Ti-Al3-V2.5	0.495	37.86	47.98	17.64	18.65
11-2	Ti-Al3-V2.5	0.503	38.02	47.88	18.09	19.27
11-3	Ti-Al3-V2.5	0.508	38.12	47.97	17.78	18.88

3.4.1.2 Preparation

Prior to testing, the following preparations were made:

(1) One side of the specimen was painted with paint, which would be helpful to take clear images of the specimen.

(2) The loading fixture and specimen was located: the centreline of upper and lower loading rods should be coincident within 0.25mm, centre the specimen with respect to the clevis opening within 0.76mm, the anti-buckling plates were slipped onto the specimen.

(3) A thermocouple was used to record the environment temperature near the specimen.

3.4.1.3 Loading

Displacement control load was applied for fracture toughness test, different loading rates were used for different specimens for significant differences in fracture toughness, and the loading rates for different specimens were recorded in Tab 3-6. The Q-400 correlation system recorded the image of the specimen every 0.25 seconds, the test continued until the specimen could sustain no further increase in applied force.

Tab 3-6 Loading rate for specimens

Specimens series:	2	3	5	6	10	11
Loading Rate(mm/min)	0.25	0.25	0.25	0.25	0.5	0.5

After testing, ‘c’ and ‘d’ points in Fig 3-5 were chosen as the displacement reference points and the force and load-line displacement data was extracted from the images by using DANTEC DYNAMICS software. The force verse load-line displacement curve could be plotted.

3.4.1.4 Crack Measurement

A microscope was used to check the initial crack size and ductile crack extension. Fig 3-6 demonstrates the crack image of specimen 5-2, the flat ‘abcd’ area was the fatigue crack area.

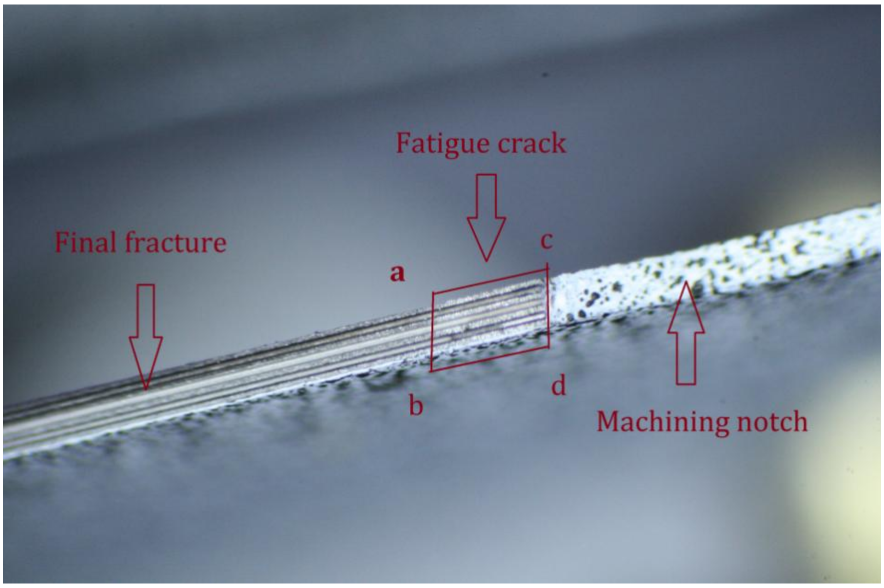

Fig 3-6 Crack image of Specimen 5-2

The length of original crack a_0 was measured from the fatigue crack line ‘ab’ (as shown in Fig 3-6) to load-line. The length of original crack a_0 was recorded in Tab 3-5.

3.4.2 Principles of Fracture Toughness Parameters Calculation

3.4.2.1 General

K_{Ic}, CTOD_c, and $\mathcal{J}_{Ic}$ values were calculated based on BS 7448-1:1991, but the standard test procedures should be modified for unidirectional reinforced titanium matrix composites which exhibit isotropic property in the plane transverse to the fibres. The force versus load-line displacement curves obtained from tests were used to determine the fracture toughness parameters.

3.4.2.2 Plane Strain Fracture Toughness K_{Ic}

To obtain a valid K_{Ic} value, the provisional fracture toughness K_Q was first calculated by applying the following equation:

$$K_Q = \frac{\mathrm{F_Q}}{\mathrm{BW^{0.5}}} \times \mathrm{f}\left(\frac{\mathrm{a_0}}{\mathrm{W}}\right) \qquad [3.2]$$

Where:

B is the thickness of the specimen; $\mathrm{a_0}$ is the initial crack length, W is the specimen width;

$\mathrm{F_Q}$ is the corresponding particular force, the method to determine $\mathrm{F_Q}$ is illustrated in Appendix C;

$\mathrm{f}\left(\frac{\mathrm{a_0}}{\mathrm{W}}\right)$ is geometric correction factor, a function of $\left(\frac{\mathrm{a_0}}{\mathrm{W}}\right)$ for compact specimens, shown in Equation 3.3.

$$f\left(\frac{\mathrm{a_0}}{\mathrm{W}}\right) = \frac{\left(2+\frac{\mathrm{a_0}}{\mathrm{W}}\right)\left[0.886+4.64\frac{\mathrm{a_0}}{\mathrm{W}}-13.32\left(\frac{\mathrm{a_0}}{\mathrm{W}}\right)^2+14.72\left(\frac{\mathrm{a_0}}{\mathrm{W}}\right)^3-5.6\left(\frac{\mathrm{a_0}}{\mathrm{W}}\right)^4\right]}{\left(1-\frac{\mathrm{a_0}}{\mathrm{W}}\right)^{1.5}} \qquad [3.3]$$

3.4.2.3 Critical Crack Tip Opening Displacement, $\mathbf{CTOD_c}$

To determine the value of $\mathrm{CTOD_c}$ in the traditional method, the force versus load-line displacement curve should be assessed to determine the forces of F as well as the corresponding value of plastic displacement $\mathrm{V_p}$.

The equation to calculate $\mathrm{CTOD_c}$ is [32]:

$$\delta = \left[\frac{\mathrm{F}}{\mathrm{BW^{0.5}}} \times \mathrm{f}\left(\frac{\mathrm{a_0}}{\mathrm{W}}\right)\right]^2 \times \frac{1}{\lambda\sigma_{\mathrm{ys}}\mathrm{E'}} + \frac{0.46(\mathrm{W}-\mathrm{a_0})\mathrm{Vp}}{0.46\mathrm{W}+0.54\mathrm{a_0}} \qquad \text{(E 3.4)}$$

Where:

B is the thickness of the specimen; $\mathrm{a_0}$ is the initial crack length, W is the specimen width;

F is the applied onset of fracture force, $\mathrm{V_p}$ is the plastic displacement; the method to determine the value of F and $\mathrm{V_p}$ is illustrated in Appendix D.

$\mathrm{f}\left(\frac{\mathrm{a_0}}{\mathrm{W}}\right)$ is geometric correction factor, a function of $\left(\frac{\mathrm{a_0}}{\mathrm{W}}\right)$ for compact specimens, shown in Equation 3.3.

λ is the stress state factor near the crack tip area, λ =2 for plane strain condition, λ =1 for plane stress condition, as the specimens were very thin, so they were probably closer to plane stress than to plane strain conditions, hence λ =1.

σ_{ys}, is the 0.2% yield strength.

E' is the 'apparent' elastic modulus in the accounted direction:

(1) for isotropic metallic materials; $\mathrm{E}' = \frac{\mathrm{E}}{1-\vartheta^2}$ [3.5];

(2) for transversely isotropic composite material [44]:

$$\mathrm{E}' = \frac{1}{\sqrt{\left(\frac{S_{11}S_{22}}{2}\right)[(\frac{S_{22}}{S_{11}})^{0.5}+\frac{2S_{12}+S_{66}}{2S_{11}}]}} \quad [3.6]$$

S_{11}, S_{12}, S_{22} and S_{66} are the compliance coefficients of composite material; Equation 2.5 shows the relationships between the engineering constants and the compliance coefficients; Tab 3-3 offers the engineering constants of the composite materials.

By using correlation system Q-400, Schwalbe δ_5 method also could be applied to determine the crack tip opening displacement at the same time with traditional method. 'm' and 'n' points, located at 2.5 mm each side from crack extension plane (shown in Fig 3-7), were selected as the reference measurement points to measure the displacement at the precrack tip $\delta_{5\mathrm{crack}}$; 'o' and 'p' points were selected as the reference measurement points to measure the displacement at the notch tip $\delta_{5\mathrm{notch}}$.

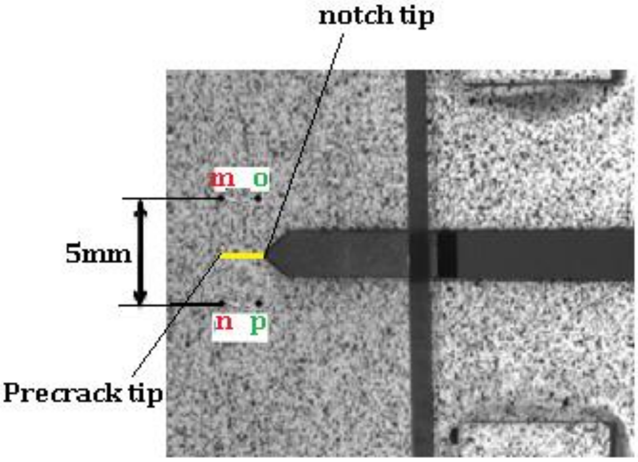

Fig 3-7 Schwalbe δ_5 method for $\mathrm{CTOD_c}$

3.4.2.4 Determination of $\mathcal{J}_{Ic}$

To obtain a valid $\mathcal{J}_{Ic}$ value, the provisional value $\mathcal{J}_Q$ was first calculated from the following equation:

$$\mathcal{J}_Q = \left[\frac{\mathrm{F}}{\mathrm{BW^{0.5}}} \times \mathrm{f}\left(\frac{\mathrm{a_0}}{\mathrm{W}}\right)\right]^2 \times \frac{1}{\mathrm{E'}} + \frac{\eta \mathrm{U_P}}{\mathrm{B(W-a_0)}} \qquad [3.7]$$

Where:

B is the thickness of the specimen; $\mathrm{a_0}$ is the initial crack length, W is the specimen width.

F is the applied onset of fracture force, $\mathrm{U_P}$ is the plastic work; the method to determine the value of F and $\mathrm{U_P}$ is detailed in Appendix D.

$\mathrm{f}\left(\frac{\mathrm{a_0}}{\mathrm{W}}\right)$ is the geometric correction factor, a function of $\left(\frac{\mathrm{a_0}}{\mathrm{W}}\right)$ for compact specimens, shown in Equation 3.3.

η is plastic work factor, $\eta=2+0.522\left(1-\frac{\mathrm{a_0}}{\mathrm{W}}\right)$. [3.8]

$\mathrm{E'}$ is the same as Equation 3.5 and Equation 3.6.

4 Result Validation, Analysis and Discussion

4.1 Force Versus Load-line Displacement Curves

The force versus load-line displacement curves obtained from tests were used to determine the fracture toughness parameters. The curves of force versus load-line displacement for series 2 and 3 specimens, series 5 specimens, series 6 specimens, series 10 specimens, series 11 specimens are shown in Fig 4-1, Fig 4-2, Fig 4-3, Fig 4-4, and Fig 4-5, respectively.

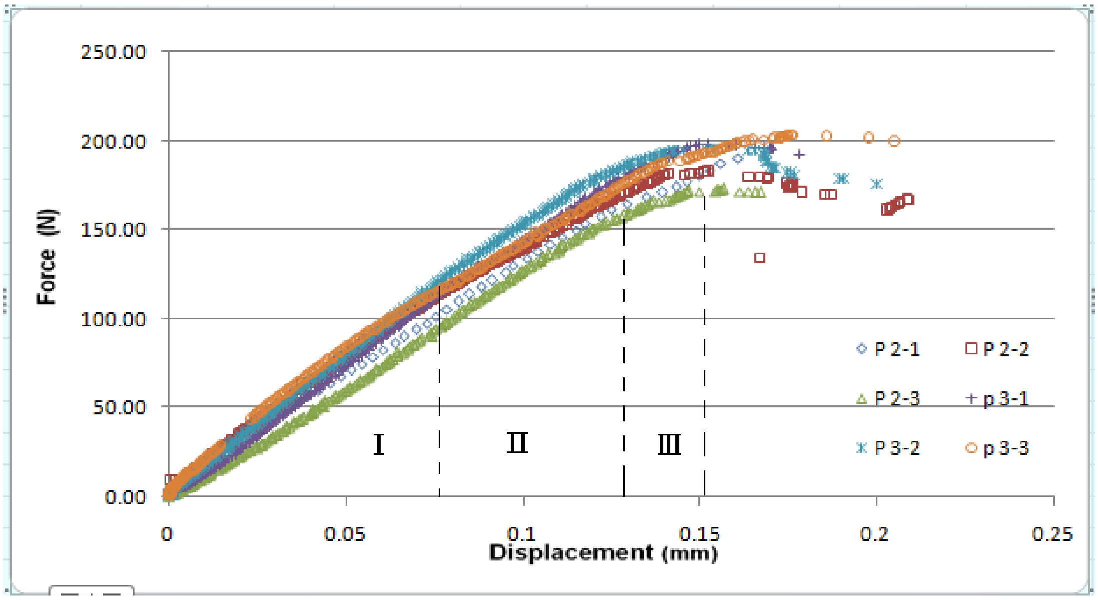

Fig 4-1 Force versus load-line displacement curves for series 2 and 3 specimens

Fig 4-1 shows the force versus load-line displacement response of Ti β 21-s/SiC specimens under transverse loading at room temperature. In region Ⅰ， the specimens behaved considerably elastic, the slopes of the curves were slightly different from each other, which was mainly induced by the inhomogeneous properties of the composite. With the increase of stress, the slope of the curves decreased gradually in region Ⅱ where debonding occurred. A significant decrease of slope in region Ⅲ indicated that fibre and matrix had separated. Finally, the specimens failed completely.

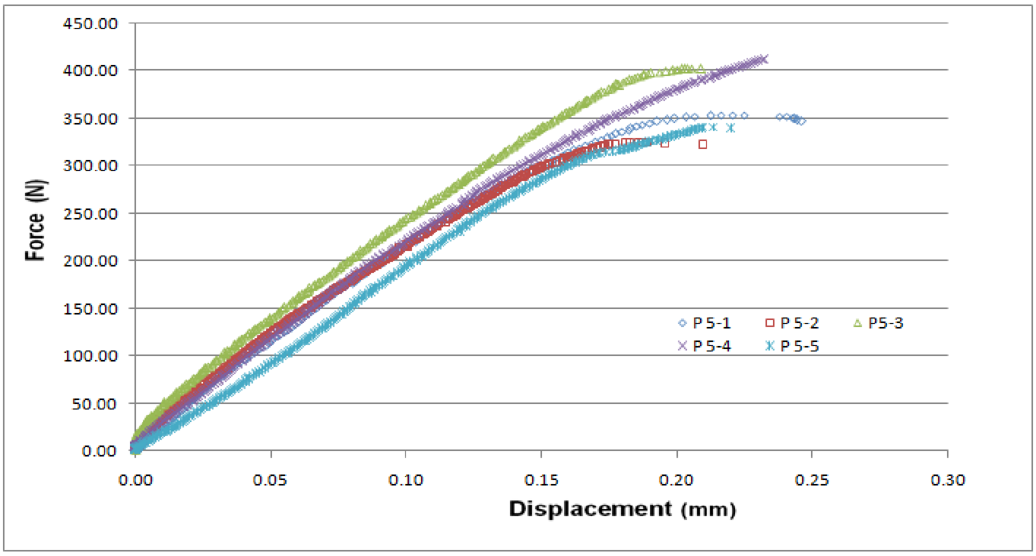

Fig 4-2 Force versus load-line displacement curves for series 5 specimens

The force versus load-line displacement response of Ti-Al3-V2.5/SiC specimens is shown in Fig 4-2. The maximum force before fracture for each Ti-Al3-V2.5/SiC specimen was between 325 N and 450 N, which was much larger than that for Ti β 21-s/SiC specimens shown in Fig 4-1. Thus the fracture resistance of Ti-Al3-V2.5/SiC specimens should be much better than the Ti β 21-s /SiC specimens.

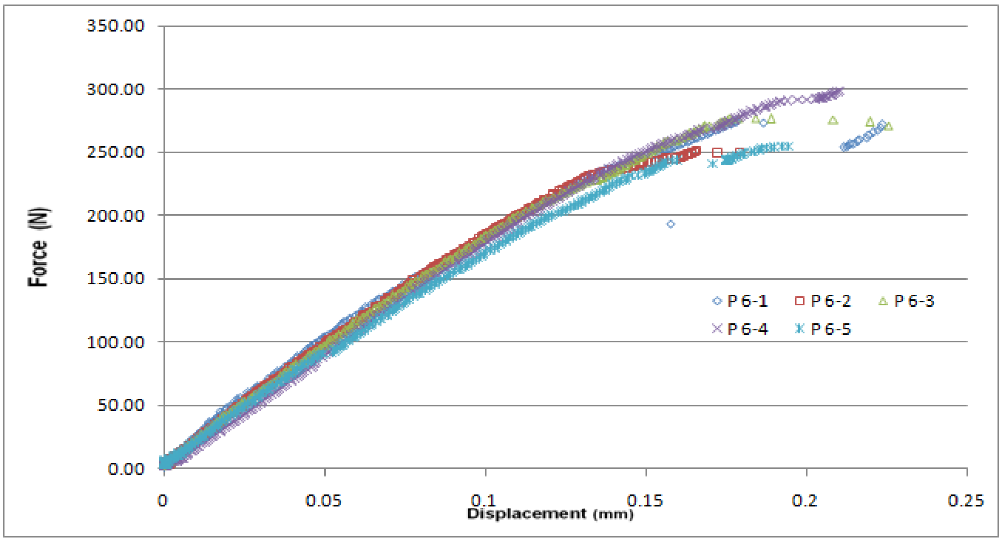

Fig 4-3 Force versus load-line displacement curves for series 6 specimens

The maximum force before fracture for each β21-S+Ticp /SiC specimen, shown in Fig 4-3, was between that for Ti-Al3-V2.5/SiC specimens and Ti β 21-s/SiC specimens, which indicated that the resistance to crack extension of β21-S+Ticp /SiC specimen should be between the other two kinds of material specimens. The curves of all the composites indicated that the fracture process of the composites were similar: at first the specimen behaved considerably elastic, then gradually fibre/matrix debonding occurred, followed by complete separation of fibre and matrix, at last failed catastrophically.

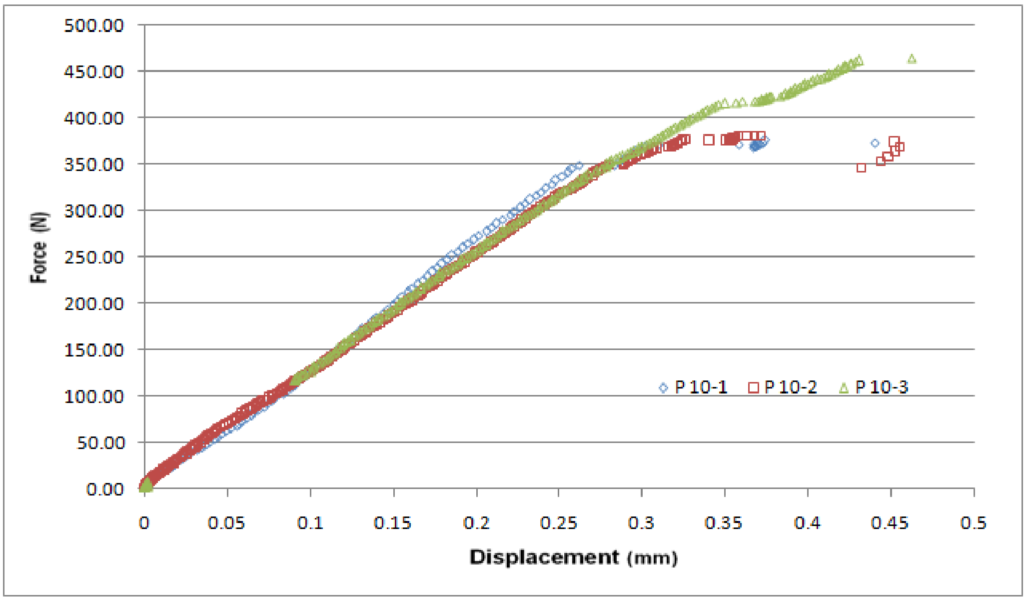

Fig 4-4 Force versus load-line displacement curves for series 10 specimens

Fig 4-4 demonstrates the force versus load-line displacement response of three Ti β 21-s alloy specimens. The curves clearly showed that the specimens behaved fully elastic before the sudden huge displacement with little force increased, the specimens broke in a brittle manner.

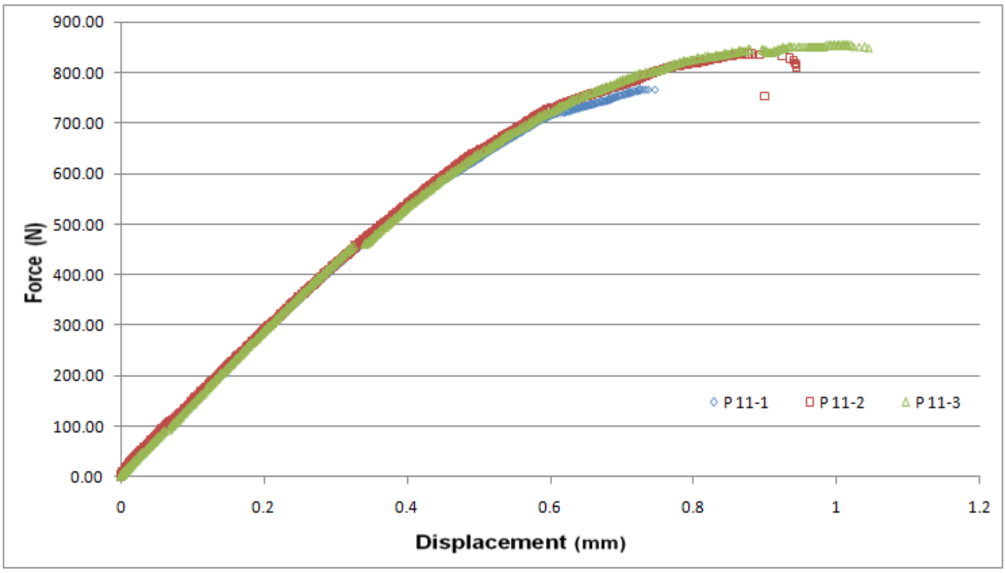

Fig 4-5 Force versus load-line displacement curves for series 11 specimens

The Ti-Al3-V2.5 alloy specimens behaved considerably plastic before fracture, shown in Fig 4-5, which indicates that the Ti-Al3-V2.5 alloy specimens were more ductile than Ti β 21-s alloy specimens. The curves of the monolithic titanium alloy specimens are distributed more closely to each other compared with composite specimens. The maximum force before fracture also indicated that Ti-Al3-V2.5 alloy specimens should resist crack extension better than Ti β 21-s alloy specimens

4.2 Result Validation

4.2.1 Plane Strain Fracture Toughness K_{Ic}

The provisional plane strain fracture toughness K_Q was calculated according to Chapter 3.4.4 and recorded in Tab 4-1.

Tab 4-1 K_Q for each specimen

Unit: (MPa$\sqrt{\mathrm{m}}$)

Plate series (Material)	NO.1	NO.2	NO.3	NO.4	NO.5	Average
2 (Ti β 21-s/SiC)	19.957	19.748	19.800			19.835
3 (Ti β 21-s/SiC)	20.708	19.237	21.616			20.520
5 (Ti-Al3-V2.5/SiC)	33.656	27.825	33.435	34.942	36.835	33.339
6 (β21-S+Ticp/SiC)	25.436	23.784	22.520	25.641	22.004	23.887
10 (Ti β 21-s)	35.510	37.077	41.172			37.920
11 (Ti-Al3-V2.5)	57.693	61.105	57.280			58.693

The procedure applied to the tests has strict validity criteria, including the form and shape of the force versus displacement curve, specimen size and crack geometry, so the results in Tab 4-1 are validated according to the following criteria；

Validation Keys [32]:

1. *The thickness of specimen B should be greater than* $2.5(K_Q/\sigma_{ys})^2$, *so that the stress state near the crack tip area corresponds for plane strain during testing.*
   Where:

K_Q is the provisional value of plane strain fracture toughness;

σ_{ys} is 0.2% yield strength of the material.

2. The original crack length should lie between the range $\mathbf{0}.45 \le \frac{a_0}{W} \le 0.55$, *so that the geometric correction factors are applicable.*

3. The ratio of F_{max}/F_Q *should be less than 1.10, so that the specimen behaves essentially elastic to ensure the test method is applicable.*

Where:

F_{max} *is the maximum applied force before fracture;*

F_Q *is the provisional force for the calculation of critical stress intensity factor.*

4. The plane of the fatigue precrack and 2% crack extension must always be within $\pm 10^{\circ}$ *of the plane of the starter notch.*

Tab 4-2 details the validation information of K_Q as K_{Ic} for all the specimens, and explains the reasons for disqualification.

Tab 4-2 Validation of K_Q as K_{Ic}

Plate NO.	B (mm)	B_{min} (mm)	$\frac{a_0}{W}$	F_Q	$\frac{F_{max}}{F_Q}$	K_Q (MPa$\sqrt{m}$)	Valid ?	Reasons (***Note***)
2-1	0.456	9.14	0.533	164.72	1.15	19.957	No	*1,3*
2-2	0.460	8.95	0.517	173.55	1.05	19.748	No	*1*
2-3	0.458	9.00	0.538	160.96	1.07	19.800	No	*1*
3-1	0.465	9.84	0.512	185.59	1.07	20.708	No	*1*
3-2	0.458	8.50	0.505	173.32	1.13	19.237	No	*1,3*
3-3	0.451	10.73	0.512	188.22	1.08	21.616	No	*1*
5-1	0.552	26.00	0.547	318.68	1.11	33.656	No	*1,3*
5-2	0.558	17.77	0.511	300.78	1.08	27.825	No	*1*
5-3	0.557	25.66	0.493	381.05	1.06	33.435	No	*1*

5-4	0.555	28.03	0.540	343.16	1.19	34.942	No	*1,3*
5-5	0.558	31.15	0.580	313.55	1.08	36.835	No	*1,2*
6-1	0.522	14.85	0.536	238.48	1.15	25.436	No	*1,3*
6-2	0.514	12.99	0.514	235.67	1.06	23.784	No	*1,3*
6-3	0.516	11.64	0.506	230.92	1.20	22.520	No	*1*
6-4	0.504	15.09	0.531	236.12	1.26	25.641	No	*1,3*
6-5	0.512	11.12	0.505	223.45	1.14	22.004	No	*1,3*
10-1	0.482	2.56	0.492	349.20	1.07	35.510	No	*1*
10-2	0.485	2.79	0.497	367.30	1.03	37.077	No	*1*
10-3	0.491	3.44	0.503	401.97	1.15	41.172	No	*1,3*
11-1	0.495	33.28	0.493	588.43	1.30	57.693	No	*1,3,4*
11-2	0.503	37.34	0.507	607.45	1.38	61.105	No	*1,3,4*
11-3	0.508	32.81	0.495	596.75	1.43	57.280	No	*1,3*

Note: the number represents the validation key which is not satisfied for each specimen.

Tab 4-2 shows that: all the specimens failed minimum thickness criterion, the specimens were not thick enough to maintain plane strain condition in the crack tip region; some composite specimens and all the titanium alloy specimens failed $\mathrm{F_{max}/F_Q}$ criterion for excessive plasticity, thus the Linear Elastic Fracture Mechanics approach was not applicable; for specimen 11-1 and 11-2, the plane of crack extension was out of $\pm 10^{\circ}$ of the plane of the starter notch. Therefore, the provisional K_Q values were not valid K_{Ic} for any tested material.

4.2.2 Critical Crack Tip Opening Displacement, $\mathbf{CTOD_c}$ and $\boldsymbol{\delta_5}$

The value of $\mathrm{CTOD_c}$ for each specimen was calculated based on BS7448 (shown in Chapter 3.4.4) and recorded in Tab 4-3.

Tab 4-3 $\mathrm{CTOD_c}$ for each specimen

Unit: mm

Plate series (Material)	NO.1	NO.2	NO.3	NO.4	NO.5	Average
2 (Ti β 21-s/SiC)	0.010	0.009	0.010			0.010
3 (Ti β 21-s/SiC)	0.007	0.009	0.011			0.009
5 (Ti-Al3-V2.5/SiC)	0.036	0.025	0.034	0.047	0.041	0.037
6 (β21-S+Ticp/SiC)	0.021	0.018	0.018	0.027	0.022	0.021
10 (Ti β 21-s)	0.019	0.020	0.034			0.024
11 (Ti-Al3-V2.5)	0.164	0.210	0.220			0.198

Crack tip opening displacement method can be used both for linear elastic behaviour materials and elastic-plastic behaviour materials, thus there is no requirement on excessive plasticity. $\mathrm{CTOD_c}$ was calculated under plane stress condition. The specimen 11-1 and 11-2 were not valid $\mathrm{CTOD_c}$, since the plane of crack extension was out of $\pm 10^{\circ}$ of the plane of the starter notch.

Tab 4-4 lists the $\mathrm{CTOD_c}$ values and δ_5 values measured at precrack tip and notch tip for each composite specimen, it is easy to find that the three values differ from each other significantly for most specimens, and $\mathrm{CTOD_c}$ value is much lower than the other two δ_5 values.

Tab 4-4 $\mathrm{CTOD_c}$ values and δ_5 values

Unit: mm

No.	$\mathrm{CTOD_c}$	$\delta_{5\mathrm{crack}}$	$\delta_{5\mathrm{notch}}$	Precrack length
2-1	0.010	0.0199	0.0298	2.06
2-2	0.009	0.0212	0.0295	2.28
2-3	0.010	0.0251	0.0387	2.14
3-1	0.007	0.0192	0.0251	1.12
3-2	0.009	0.0316	0.0406	1.41
3-3	0.011	0.0232	0.0289	1.45
5-1	0.036	0.0320	0.0628	2.67
5-2	0.025	0.0282	0.0365	1.30
5-3	0.034	0.0162	0.0239	1.40
5-4	0.047	0.0271	0.0442	3.23
5-5	0.041	0.0358	0.0541	4.41
6-1	0.021	0.0173	0.0324	2.18
6-2	0.018	0.0239	0.0301	1.53
6-3	0.018	0.0273	0.0382	2.19
6-4	0.027	0.0293	0.0439	1.86
6-5	0.022	0.0294	0.0367	0.88

Fig 4-6 shows a comparison between $\mathrm{CTOD_c}$ value and δ_5 values measured at precrack tip and notch tip for each composite specimen. It shows that $\mathrm{CTOD_c}$ values do not match the critical δ_5 values measured at the precrack tip $\delta_{5\mathrm{crack}}$ or measured at the notch tip $\delta_{5\mathrm{notch}}$ very well. For most specimens, $\delta_{5\mathrm{crack}}$ is relatively close to $\mathrm{CTOD_c}$. The differences between $\mathrm{CTOD_c}$ values and critical δ_5 values might be caused by: (1) the value of 0.2% yield strength to calculate $\mathrm{CTOD_c}$ was assumed to be the same as the fibre/matrix debonding strength of Ti-6Al-4V/SiC; (2) the specimens were very thin and the crack propagated rapidly along the fibre/matrix interface during precracking, so the real precrack length should be greater than the precrack length measured from the fatigue surface.

Therefore, it is better to measure δ_5 at the precrack tip for thin Ti/SiC composite specimens, the values of $\mathrm{CTOD_c}$ need to be refined.

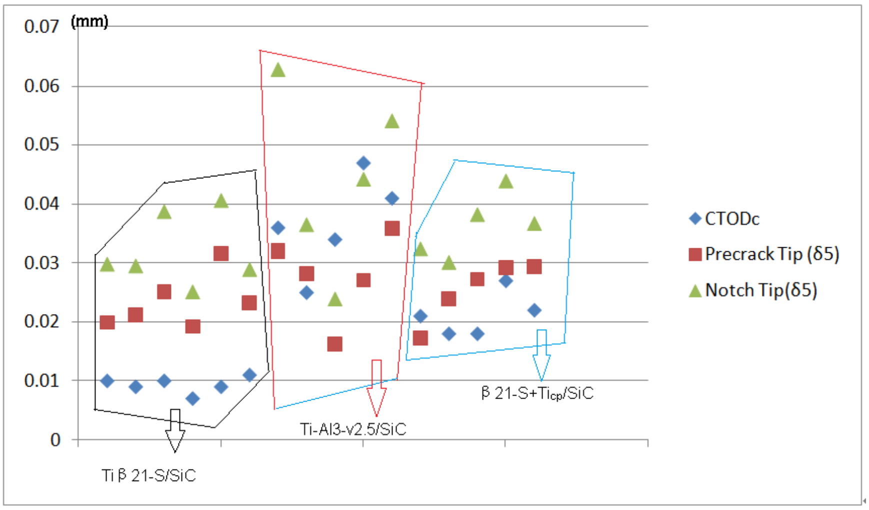

Fig 4-6 Comparison between $\mathrm{CTOD_c}$ values and δ_5 values

4.2.3 Critical $\mathcal{J}$-integral $\mathcal{J}_{Ic}$

The value of $\mathcal{J}_Q$, the provisional value of $\mathcal{J}_{Ic}$, for each specimen was calculated according to Chapter 3.4.4 and recorded in Tab 4-5

Tab 4-5 $\mathcal{J}_Q$ for each specimen

Unit: kN/m

Plate series (Material)	NO.1	NO.2	NO.3	NO.4	NO.5	Average
2 (Ti β 21-s/SiC)	3.617	3.191	3.143			3.317
3 (Ti β 21-s/SiC)	3.109	3.425	4.334			3.623
5 (Ti-Al3-V2.5/SiC)	12.547	8.207	11.408	15.134	13.583	12.176
6 (β21-S+Ticp/SiC)	6.499	5.221	5.655	8.423	5.790	6.318

10 (Ti β 21-s)	18.945	17.173	25.247			20.455
11 (Ti-Al3-V2.5)	81.970	113.036	123.489			106.165

The results in Tab 4-5 have to be checked to ensure that they satisfy the validity criteria of $\mathcal{J}_{Ic}$. It shows that ductile initiation toughness would be independent of thickness as long as the plane-strain state prevails in the centre of the specimens [35]. Therefore, the minimum thickness criterion is:

$$\mathrm{B}_{\min} > 25\frac{\mathcal{J}_Q}{\sigma_{\mathrm{ys}}} \quad [4.1]$$

All the minimum thickness for each specimen is listed in Tab 4-6, it shows that all the series 2 and 3 specimens met the thickness criterion, part of series 6 and 10 specimens met, none of series 5 or 11 specimens was thick enough for the thickness criterion for $\mathcal{J}_{Ic}$ tests.

Tab 4-6 Validation of $\mathcal{J}_Q$ as $\mathcal{J}_{Ic}$

Plate NO.	B (mm)	$\mathrm{B}_{\min}$(mm)	$\mathcal{J}_{\mathrm{Q}}$ (kN/m)	Valid?	Reasons (***Note***)
2-1	0.456	0.2740	3.617	Yes	/
2-2	0.460	0.2417	3.191	Yes	/
2-3	0.458	0.2381	3.143	Yes	/
3-1	0.465	0.2355	3.109	Yes	/
3-2	0.458	0.2595	3.425	Yes	/
3-3	0.451	0.3283	4.334	Yes	/
5-1	0.552	0.9505	12.547	No	*TC*
5-2	0.558	0.6218	8.207	No	*TC*
5-3	0.557	0.8642	11.408	No	*TC*

5-4	0.555	1.1465	15.134	No	*TC*
5-5	0.558	1.0290	13.583	No	*TC*
6-1	0.522	0.4924	6.499	Yes	*/*
6-2	0.514	0.3955	5.221	Yes	*/*
6-3	0.516	0.4284	5.655	Yes	*1*
6-4	0.504	0.6381	8.423	No	*TC*
6-5	0.512	0.4386	5.790	Yes	*/*
10-1	0.482	0.3971	18.945	Yes	*/*
10-2	0.485	0.3831	17.173	Yes	*/*
10-3	0.491	0.5686	25.247	No	*TC*
11-1	0.495	4.0985	81.970	No	*TC, CE*
11-2	0.503	5.6518	113.036	No	*TC, CE*
11-3	0.508	6.1744	123.489	No	*TC*

Note: 'TC' stands for the thickness criterion was not satisfied;

'CE' stands for the plane of crack extension criterion was not satisfied.

For specimen 11-1 and 11-2, the plane of crack extension was not within 10° of the plane of the starter notch.

Therefore, all the provisional $\mathcal{J}_Q$ values for Ti β 21-s/SiC were valid $\mathcal{J}_{Ic}$; $\mathcal{J}_{Ic}$ tests on specimen 6-1, 6-2, 6-3, 6-5 and 10-1,10-2 and were also valid; none of Ti-Al3-V2.5/SiC or Ti-Al3-V2.5 alloy specimens' provisional critical $\mathcal{J}$ values obtained from tests were valid $\mathcal{J}_{Ic}$.

4.3 Analysis and Discussion

4.3.1 Fracture Mechanisms of the Specimens

Fig 4-7 demonstrates two images of the specimen after tensile loading. Image (a) was the image of specimen 3-3, it shows that the crack extension was along the fibre direction; whereas, for the monolithic alloy specimen 11-3, image (b) shows that the crack plane was not very flat.

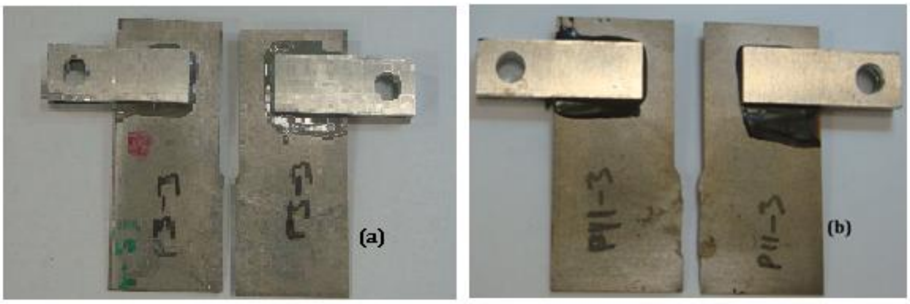

Fig 4-7 Specimens images after tensile loading

The fracture surface image of specimen 3-3, shown in Fig 4-8, shows that the specimens failed through the titanium alloy matrix and few broken SiC fibres was observed. It also could be found that the fibres completely separated with the matrix when crack extended and the fracture surface was along the fibre/matrix interface plane, which means fibre/matrix debonding occurred first, then with further loading, fibres bore no stress, finally matrix fracture catastrophically through the high stress distribution area (the red circle area shown in Fig 4-9).

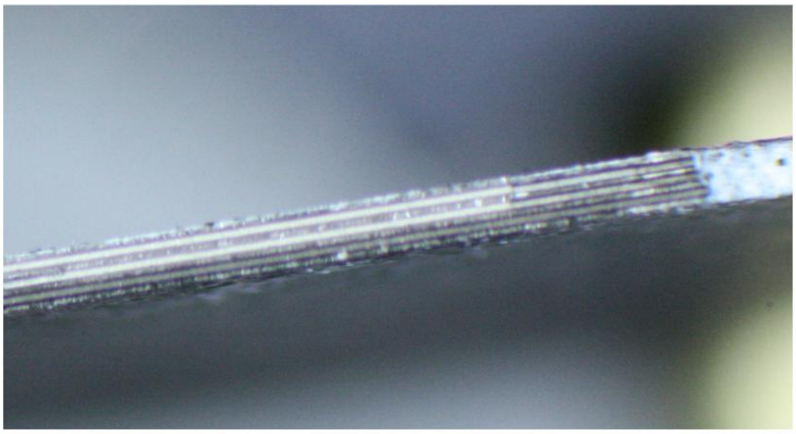

Fig 4-8 Fracture surface image of specimen 3-3

Fig 4-9 schematically shows the process of fracture of the Ti/SiC composites under transverse tensile loading.

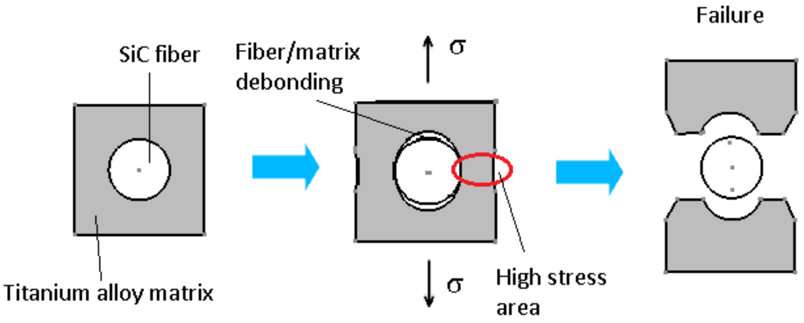

Fig 4-9 Schematic presentation of fracture process

In Fig 4-10, two pictures of a composite specimen taken in 0.25 seconds are illustrated; it is easy to see that the crack propagated rapidly and catastrophically through the specimen. Cleavage fracture occurred for all the composite specimens in this thesis, after fibre/matrix debonding the fibres took no loading, all the stress was taken by the matrix.

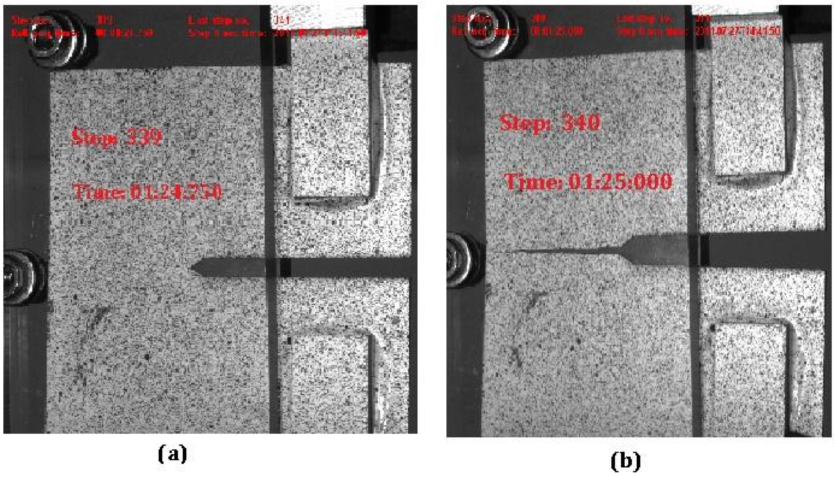

Fig 4-10 Crack extension image of Specimen 6-5

The matrix/fibre debonding changed the stress distribution on the matrix and fibres, which could cause the stress at the red circle area (shown in Fig 4-9) suddenly increased significantly. The increment of stress at the high stress distribution area is mainly determined by the fibre volume fraction, the stress is higher with higher fibre volume fraction. When the stress at that area exceeds the yield strength of the titanium matrix, matrix failure happens and crack propagates.

Therefore, it was the fibre/matrix interface strength that triggered the fracture of the composites under transverse loading, the final fracture behaviour of the composite was still mainly affected by the fibre volume fraction and the strength of the titanium alloy matrix.

4.3.2 Plane Strain Fracture Toughness K_{Ic}

The thickness of the specimens affected the validity of plane strain fracture toughness test in two major ways:

(1) For the thin specimens, the plane strain condition did not exist, so the equation applied to calculate plane strain fracture toughness could be not accurate.

(2) The Linear Elastic Fracture Mechanics approach was not applicable in some of the composite specimens and all the titanium alloy specimens tests, since the specimens was very thin, lacking of constraints from surrounding material, the specimens did not behave essentially elastic.

After checking the average ratio of $\mathrm{F_{max}/F_Q}$ in Fig 4-11, it could be found that:

(1) Ti β 21-s reinforced with 45% volume SiC fibre and monolithic Ti β 21-s alloy specimens exhibited essentially linear-elastic.

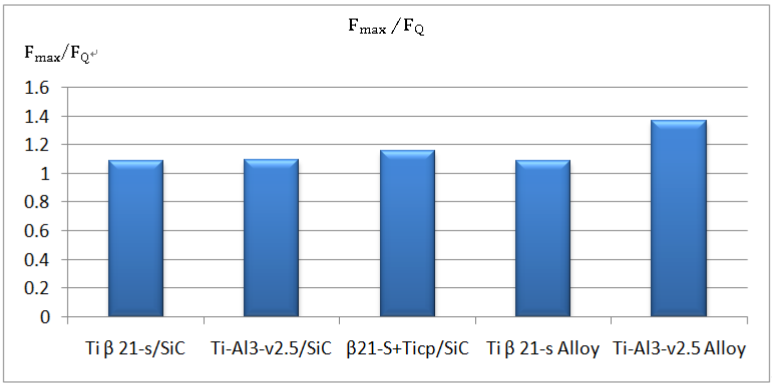

Fig 4-11 Average value of $\mathrm{F_{max}/F_Q}$ for each material

(2) The average value of $\mathrm{F_{max}/F_Q}$ for 25% volume SiC fibre reinforced Ti-Al3-V2.5 specimens and monolithic Ti-Al3-V2.5 was 1.10 and 1.37, respectively, which means that the plastic ability of Ti-Al3-V2.5 decreased considerably

after reinforced with SiC fibre.

(3) Ti-Al3-V2.5 alloy was more ductile than Ti β 21-s alloy for the same thickness structure.

The fracture toughness results obtained from the tests were not valid K_{Ic} for these materials, so they could not be widely used for other thickness structures. However, the results, shown in Fig 4-12, provide plenty of information about the properties and performance of these materials:

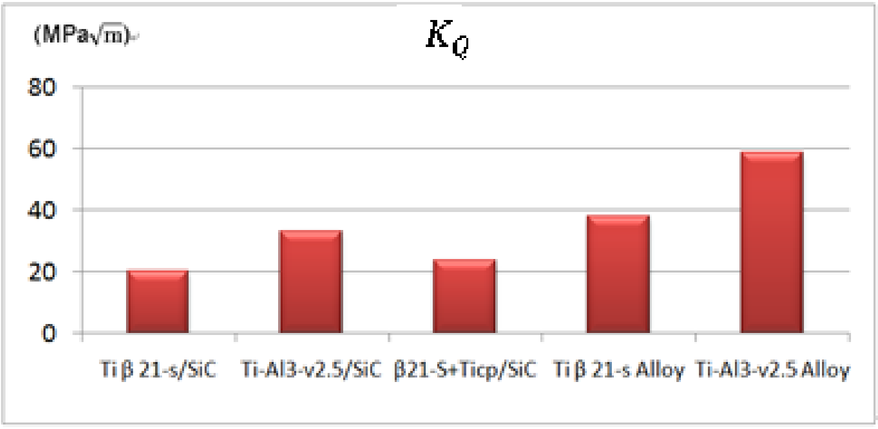

Fig 4-12 Average value of K_Q for each material

(1) The values of K_Q obtained from the tests could be used as particular fracture toughness for 0.5 mm thick structures of the materials.

(2) The values of K_Q could also be used to compare different composite materials of the same thickness.

(3) A summary of thickness effects on fracture toughness for cleavage fracture mode and ductile fracture mode for steel is schematically presented in Fig 4-13 [35]. The figure shows that the critical stress intensity factor K_c increases with decreasing thickness for cleavage fracture (red curve); for ductile fracture (blue curve), the maximum value of K_c is at a point where the thickness of the material is between the minimum critical thickness for $\mathcal{J}_{Ic}$ and the minimum critical thickness for K_{Ic}.

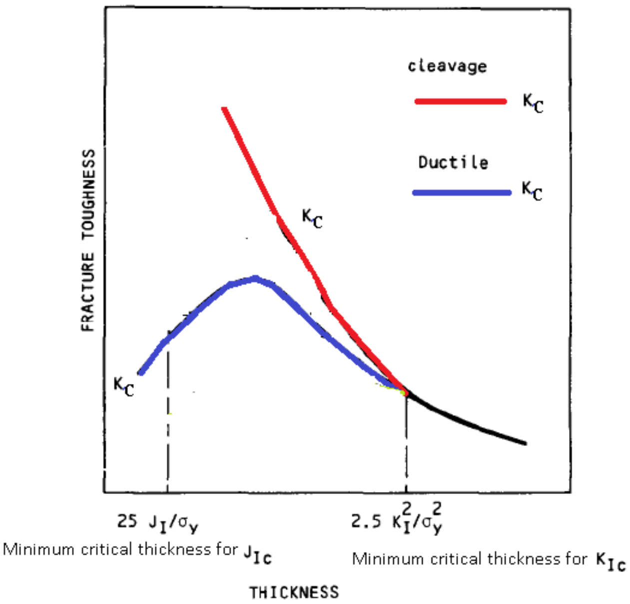

Fig 4-13 Thickness effects on cleavage fracture and ductile fracture [35]

All the composite specimens suffered cleavage fracture and the composites specimens are much thinner than the minimum critical thickness for K_{Ic}, thus the plane strain fracture toughness K_{Ic} of the composites should be less than the critical stress intensity factor K_{c}. By applying a simplified thickness correction model for cleavage fracture, shown in Equation 4.2, the plane strain fracture toughness K_{Ic} for the composite materials at minimum critical thickness are predicted and shown in Tab 4-7.

$$K_{Ic} = K_{\mathrm{c}} \times (\frac{\mathrm{B}}{\mathrm{B_{min}}})^{0.25} \quad [4.2]$$

Where:

K_{c}= the critical stress intensity factor of the specimen with the thickness of B;

$\mathrm{B_{min}}$ = the minimum critical thickness for plane strain fracture toughness K_{Ic}.

(4) The values of K_Q for titanium matrix composites are significantly lower than those for the titanium alloys, which means that the fracture toughness of the matrix alloy decreases dramatically after being unidirectional reinforced with

SiC fibres.

Tab 4-7 Predicted K_{Ic} at the minimum critical thickness

	Ti β 21-s/SiC	Ti-Al3-V2.5/SiC	β 21-S+Ti$_{cp}$/SiC
K_{Ic} (MPa$\sqrt{\mathrm{m}}$)	10.36	14.14	12.36

(5) Ti-Al3-V2.5 reinforced with 25% volume fraction SiC fibre performs better than the other two composites in fracture resistance, but the advantage is not significant.

(6) For Ti-Al3-V2.5 alloy, the critical stress intensity factor K_c in this thesis is 81.9 MPa$\sqrt{\mathrm{m}}$, the value of plane-stress critical stress intensity factor from NASGRO subroutine "material database" is 75 $\mathrm{MPa}\sqrt{\mathrm{m}}$. So, these two values are close to each other, which means that the tests in this research were considerably reliable.

4.3.3 Crack Tip Opening Displacement, $\mathbf{CTOD_c}$

Crack tip opening displacement method can be used both for linear elastic behaviour materials and elastic-plastic behaviour materials. The results shown in Fig 4-14 provide some properties and performance of these materials:

(1) The values of $\mathrm{CTOD_c}$ obtained from the tests could be used as fracture toughness parameter for all thickness structures of the materials, which would be useful for determining the Crack Opening Displacement (COD) design curve to assess failure [30].

(2) The values of $\mathrm{CTOD_c}$ for Titanium alloy matrix composites are significantly lower than those for the matrix alloys, which means that the fracture toughness of the matrix alloy decreases dramatically after being unidirectional reinforced with SiC fibre.

(3) Ti-Al3-V2.5 reinforced with 25% volume fraction SiC fibre performs better than the other two composites in fracture resistance.

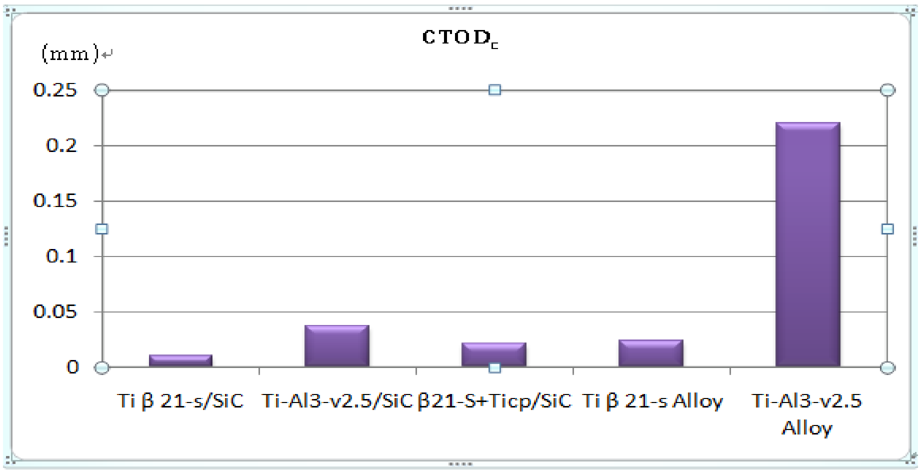

Fig 4-14 Average value of $\mathrm{CTOD_c}$ for each material

4.3.4 $\mathcal{J}$-integral $\mathcal{J}_{Ic}$

$\mathcal{J}_{Ic}$ can be used both for linear elastic behaviour materials and elastic-plastic behaviour materials to describe the material resistance to fracture. The results in Fig 4-15 offer some properties and performance of these materials:

(1) The values of $\mathcal{J}_{Ic}$ obtained from the tests could be used as fracture toughness parameter for all thickness structures of the materials, which would be useful for determining the Failure Assessment Diagram (FAD) [30].

(2) The values of $\mathcal{J}_Q$ obtained from the tests for Ti-Al3-V2.5/SiC and Ti-Al3-V2.5 alloy could be used as a particular fracture toughness parameter for 0.5 mm thick structures.

(3) The values of $\mathcal{J}_{Ic}$ $(\mathcal{J}_Q)$ for Titanium alloy matrix composites are significantly lower than those for the matrix alloys, which means that the fracture toughness of the matrix alloy decreases dramatically after being unidirectional reinforced with SiC fibre.

(4) Ti-Al3-V2.5 reinforced with 25% volume fraction SiC fibre performs better than the other two composites in fracture resistance.

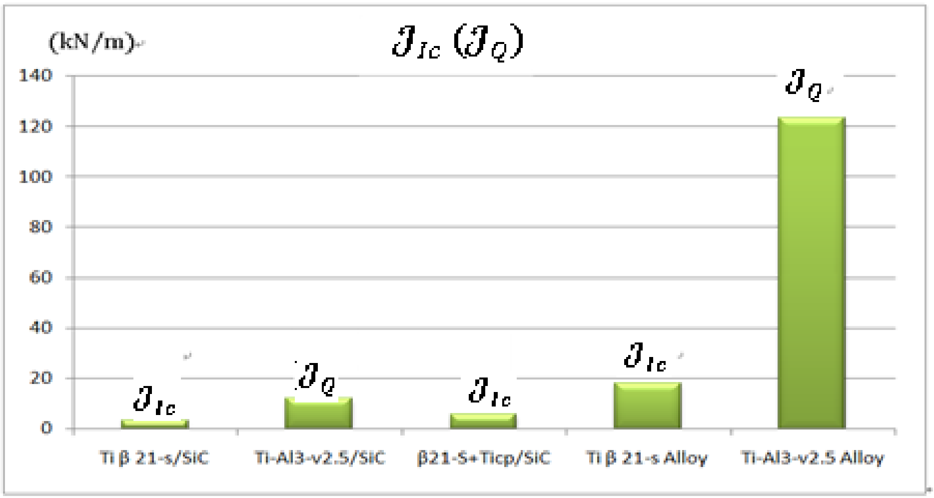

Fig 4-15 Average value of $\mathcal{J}_{Ic}\,(\mathcal{J}_Q)$ for each material

4.4 **Summary**

The fracture mode as well as the validity and discussions of the fracture toughness parameters are summarized below:

Fracture surface image shows that it is the fibre/matrix interface strength that triggered the fracture of the composites in the direction perpendicular to the fibre axis.

The values of K_Q were not qualified plane strain fracture toughness for any material; the $\mathcal{J}_Q$ values of Ti-Al3-V2.5/SiC and Ti-Al3-V2.5 were not qualified for $\mathcal{J}_{Ic}$, since the thickness of the specimens were thinner than the critical valid thickness.

Fig 4-16 shows that the conclusions drawn from K_Q, $\mathrm{CTOD_c}$ and $\mathcal{J}_{Ic}(\mathcal{J}_Q)$ were in accord with each other. Three fracture parameters all indicate that: the fracture toughness of the matrix alloy decreases dramatically after being unidirectional reinforced with SiC fibre; Ti-Al3-V2.5 reinforced with 25% volume fraction SiC fibre performs better than the other two composites in fracture resistance, but the advantage is not significant.

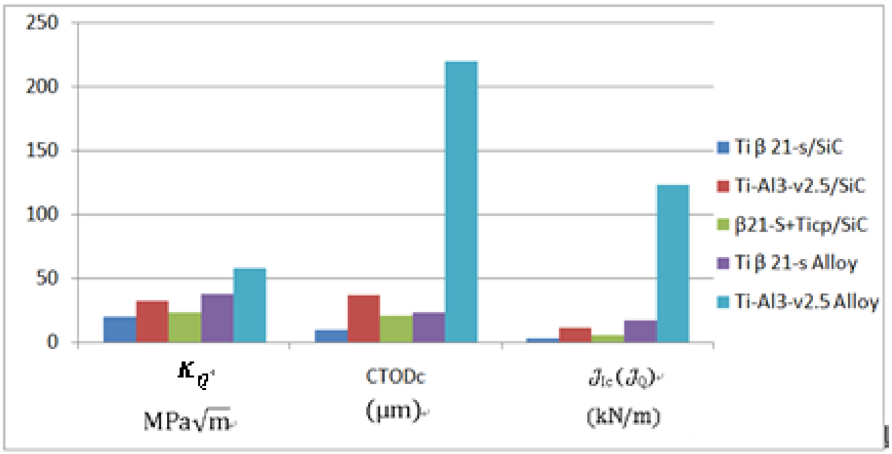

Fig 4-16 Comparison of K_Q, $\mathrm{CTOD_c}$ and $\mathcal{J}_{\mathrm{Ic}}(\mathcal{J}_Q)$ between different materials

5 Conclusion

The fracture toughness of three kinds of 0.5 mm thick composite specimens, Ti β21-S reinforced with 45% volume SiC fibre, Ti-Al3-V2.5 reinforced with 25% volume SiC fibre and β21-S+Ti$_{cp}$ reinforced with 35% volume SiC fibre were experimentally studied in the direction perpendicular to the fibre axis; fracture toughness tests were also conducted on monolithic Ti β21-S alloy and Ti-Al3-V2.5 alloy specimens; the fracture surface and the fracture toughness tests results show that:

(1) For all the titanium matrix composite specimens in this research, fibre/matrix debonding occurs before matrix deformation, leading to rapid fracture. It is the fibre/matrix interface strength that triggers the fracture of the Ti/SiC composite specimens. The fracture toughness of matrix alloys decreased significantly after being unidirectional reinforced with SiC fibre.

(2) The values of $\mathcal{J}_{Ic}$ and CTOD_c obtained from the tests could be used as fracture toughness parameter for all thickness structures of the materials.

(3) The values of K_Q were not qualified for all the materials, $\mathcal{J}_Q$ are not qualified for $\mathcal{J}_{Ic}$ for Ti-Al3-V2.5/SiC and Ti-Al3-V2.5 alloy. Therefore, they could not be widely used for other thickness structures. Nevertheless, the initial values could be used as a particular fracture toughness parameter for 0.5 mm thick structures of the materials.

(4) Ti-Al3-V2.5 reinforced with 25% volume fraction SiC fibre performs better than the other two composites in terms of fracture resistance.

6 Future Testing Recommendations

In this thesis, the material properties used for the calculation of $\mathrm{CTOD_c}$ and $\mathcal{J}_{Ic}$ were based on Halpin-Tsai equations and assumptions. The factors, processing-related fibre imperfect distribution, matrix/fibre bonding condition and residual stresses, were not accounted into consideration. Hence it is recommended that the engineering properties of the composites should be tested to refine the test results.

More investigations could be carried out to better correlate the δ_5 values with $\mathrm{CTOD_c}$ value for thin titanium composite materials.

Models could be built to predict the fracture toughness of thin Ti/SiC materials.

REFERENCES

[1] T.L. Anderson. Fracture mechanics fundamentals and applications. Third Edition, CRC Press, 2005.

[2] J.J. Duga, W.H. Fisher, A.R. Rosenfield, E.J. Honton and S.C. McMillan. The economic effect of fracture in the United States. NBS Special Publication 647-2, U.S. Department of commerce, Washington, DC, March 1983.

[3] M.M. Aghdam, S.R. Falahatgar, M. Gorji. Micromechanical consideration of interface damage in fiber reinforced Ti-alloy under various combined loading conditions. Composites Science and Technology, 68, 2008, p.3406 – 3411.

[4] Carl T. Herakovich. Mechanics of fibrous composites. 1998.

[5] S. Syngellakis, N. Cherukunnath. Boundary element analysis of symmetrically laminated plates. Engineering Analysis with Boundary Elements, 28, 2004, p. 1005–1016.

[6] D.B. Zahl, S. Schmauder. Transverse strength of continuous fiber metal matrix composites. Computational Material Science, 3, 1994, p. 293-299.

[7] S. Mukherjee, C.R. Ananth and N. Chandra. Effects of interface chemistry on the fracture properties of titanium matrix composites. Composites Part A, 29A, 1998, p. 1213–1219.

[8] Titanium Alloys-Physical Properties, Citing Internet resources (WWW document).http://www.azom.com/article.aspx?ArticleID=1341#_Tensile _Strength. (accessed 16th September 2011)

[9] S. Mall, T. Fecke, M.A. Foringer. Titanium matrix composites: Mechanical behavior (Eds: S. Mall, T. Nicholas). Technomic Publishing Co, Inc. Lancaster, Basel, 1998, p.1-22.

[10] C. Leyens, J. Hausmann, J. Kumpfert. Continuous fibre reinforced titanium matrix composites: fabrication, properties, and applications. Advanced Engineering Materials, Volume 5, issue 6, 2003, p. 399-410

[11] J. Frischbier, J. Hausmann. Assessment of failure mechanisms of aero engine TMC rotor disks at high rates of strain. Damage & Fracture Mechanics Ⅶ, edited by C.A. Brebbia and S-I. Nishida, 2003, p. 413-423.

[12] D.B. Gundel, S. G. Warrier and D. B. MircaleI. The interface debond stress in single and multiple SiC fiber/Ti-6Al-4V composites under transverse tension. Acta mater, Volume 45, No. 3, 1997, p. 1275-1284.

[13] D.B. Gundel, S.G. Warrier, D.B. Miracle. The transverse tensile behavior of SiC-fiber/Ti-6Al-4V composites 2. Stress distribution and interface failure. Composites Science and Technology, 59, 1999, p. 1087-1096.

[14] J.M. Yang, S. M. Jeng and C. J. Yang. Fracture mechanisms of fiber-reinforced titanium alloy matrix composites, Part I: Interfacial behavior. Material Science and Engineering, A138, 1991, p. 155-167.

[15] Akira Fukushima, Chikara Fujiwara, Yutaka Kagawa, Chitoshi Masuda. Effect of interfacial properties on tensile strength in SiC:Ti–15–3 composites. Materials Science and Engineering, A276, 2000, p. 243–249.

[16] C.J. Boehlert, B.S. Majumdar,S. Krishnamurthy, and D.B. Miracle. Role of matrix microstructure on room-temperature tensile properties and fibre-strength utilization of an orthorhombic Ti-Alloy-based composite. Metall. Mater. Trans. A, Volume, 28A, 1997, p. 309-323.

[17] B.S. Majumdar, T.E. Matikas, and D.B. Miracle. Experiments and analysis of fibre fragmentation in single and multiple-fibre SiC/Ti-6Al-4V metal matrix composites. Composites Part B: Engineering, Volume 29, Issue 2, 1998, p. 131-145.

[18] C. González and J. Llorca. Numerical simulation of the fracture behavior of Ti/SiC composites between 20 ℃ and 400 ℃. Metallurgical and Material Transactions A, Volume 38A, January, 2007, p.169-179.

[19] C.H. Weber, X. Chen, S.J. Connell, and F.W. Zok. On the tensile properties of a fibre reinforced titanium matrix composite—I. Unnotched behavior. Acta Metallurgica et Materialia, Volume 42, Issue 10, October 1994, p. 3443-3450

[20] C. González and J. LLorca. Micromechanical modelling of deformation and failure in Ti–6Al–4V/SiC composites. Acta Materialia, Volume 49, 2001, p. 3505-3519.

[21] Z.H. Xia and W.A. Curtin. Life prediction of titanium MMCs under low-cycle fatigue. Acta Materialia, Vol. 49, Issue 9, 25 May 2001, p. 1633-1646.

[22] J.C. Halpin and J. L. Kardos. The Halpin-Tsai Equations: A Review, Polymer Engineering and Science, 16(5), 1976, p. 344-352.

[23] B. Harris. Engineering Composite Materials. Second Edition, 1999, p. 45-89.

[24] M.M. Aghdam, S.R. Falahatgar, M. Gorji. Micromechanical consideration of interface damage in fiber reinforced Ti-alloy under various combined loading conditions. Composites Science and Technology, 68, 2008, p. 3406 – 3411.

[25] C. González, J. LLorca, A. Weck. Toughness of fibre-reinforced titanium as a function of temperature: experimental results and micromechanical modeling. Acta Materialia, 52, 2004, p. 3929 – 3939.

[26] N. Hansen, D. Juul Jensen, T. Leffers. Metal matrix composites-processing. microstructure and properties. 1991, p. 123-147.

[27] Z. Gurdal, R.l T. Haftka, P. Hajela. Design and optimization of laminated composite materials. 1999, p. 231-260.

[28] Isaac M. Daniel, Ori Ishai. Engineering mechanics of composite materials. Oxford University Press, 1994, p. 102-130.

[29] Chapter 2: Macromechanical analysis of a Lamina (Lecture 5). Retrieved from

http://www.southalabama.edu/engineering/mechanical/faculty/gou/Teaching/ME582/index.htm. (accessed 5th September 2011)

[30] M. Janssen, J. Zuidema and R. Wanhill. Fracture Mechanics, Second edition, Spon Press, 2004.

[31] NDT Resource Center, Fracture toughness. Retrieved from http://www.ndt-ed.org/EducationResources/CommunityCollege/Materials/Mechanical/FractureToughness.htm. (accessed 10th September 2011)

[32] British Standards Institution BS 7448-1:1991. Method for determination of K_{Ic}, critical CTOD and critical $\mathcal{J}$ values of metallic materials. BSI (2002): London.

[33] ASTM Standard E 1820-09. Standard test method for measurement of fracture toughness. ASTM Int'l, 2009.

[34] E.M. Castrodeza, J.M. Rodrigues Touça, J.E. Perez Ipiña, F.L. Bastian. Determination of $\mathrm{CTOD_c}$ in fibre metal laminates by ASTM and Schwalbe methods. Materials Research, Volume.5, No.2, 2002, p. 119-124

[35] Kim Wallin. The size effect in K_{Ic} results. Engineering Fracture Mechanics, Vol 22, No.1, 1985, p. 149-163.

[36] Castrodeza EM, Schneider Abdala MRW, Bastian FL. Crack resistance curves of GLARE laminates by elastic compliance. Eng Fract Mech, 2006, p. 2292–303.

[37] A.R. Shahani, M. Rastegar, M. Botshekanan Dehkordi, H. Moayeri Kashani. Experimental and numerical investigation of thickness effect on ductile fracture toughness of steel alloy sheets. Engineering Fracture Mechanics, 77, 2010, p. 646 – 659.

[38] R.A. Mirshams, C.H. Xiao, S.H. Whang, W.M. Yin. R-Curve characterization of the fracture toughness of nanocrystalline nickel thin sheets. Materials Science and Engineering, A315 ,2001, p. 21–27.

[39] J. Lord, Fracture Toughness test methods for PRM, MMC-Assess – thematic network, Volume 10, 2007.

[40] E.M. Castrodeza, J.E. Perez Ipiña, F.L. Bastian. Fracture toughness evaluation of unidirectional fibre metal laminates using traditional CTOD (δ) and Schwalbe (δ_5) methodologies. Engineering Fracture Mechanics 71, 2004, p.1107 – 1118

[41] DANTEC DYNAMICS Digital Image Correlation System (Q-400) Technical Data. Retrieved from http://www.dantecdynamics.com/Default.aspx?ID=855 (accessed 16th September 2011).

[42] ASTM Standard E 399-09. Standard test method for linear-elastic plane-strain fracture toughness K_{Ic} of metallic materials. ASTM Int'l, 2008.

[43] M. M. Ranjbaran. Experimental investigation of fracture toughness in Al 356-SiCp aluminium matrix composite. American journal of science and industrial research, 1(3), 2010, p.549-557.

[44] E.M. Castrodeza, J.E. Perez Ipiña, F.L. Bastian. Experimental techniques for fracture instability toughness determination of unidirectional fibre metal laminates. Fatigue & Fracture of Engineering Materials & Structures, Volume 25, Issue 11, 2002, p. 999-1008.

[45] J.R. Rice. A path independent integral and the approximate analysis of strain concentration by notches and cracks. Journal of Applied Mechanics, Volume 35, 1968, p. 379-386.

[46] R. Sinclair, M. Preuss, E. Maire, J.Y. Buffiere, P. Bowen, P.J. Withers. The effect of fibre fractures in the bridging zone of fatigue cracked Ti-6Al-4V/SiC fibre composites. Acta Materialia, 52, 2004, p. 1423 – 1438.

[47] M. N. Yuan, Y.Q. Yang, B. Huang, J.K. Li, Y. Chen. Evaluation of interface fracture toughness in SiC fiber reinforced titanium matrix composite. Trans. Nonferrous Met. Soc. China, 18, 2008, p. 925-929.

Appendix A -Specimen and Anti-buckling plates analysis

To prevent out-of-plane bucking and specimen crash during test, the static stress distribution and buckling analysis were conducted by Garry Voss of the Reaction Engines Limited. The analysis results and conclusions are listed in this Appendix.

A.1 Static Stress Analysis

The static stress distribution in the fracture toughness test specimen is shown in Fig A-1 and Fig A-2 for the homogenous titanium alloy sample and for the orthotropic Ti/SiC material. Both samples have a thickness of 0.44mm and were subjected to the same 400N axial load (z direction) applied to the top section of the upper pin hole. The sample is restrained at the bottom of the lower pin hole. The stress distributions are similar in both cases but the maximum deflection is lower for the Ti/SiC case due to its higher Young's modulus. Note that the LHS of the specimen is in axial compression and there is a small amount of compression along the upper and lower edges of the specimen. The contours of Von Mises stress are shown in Fig A-3 and Fig A-4 for the regions around the crack tip and around the pin hole.

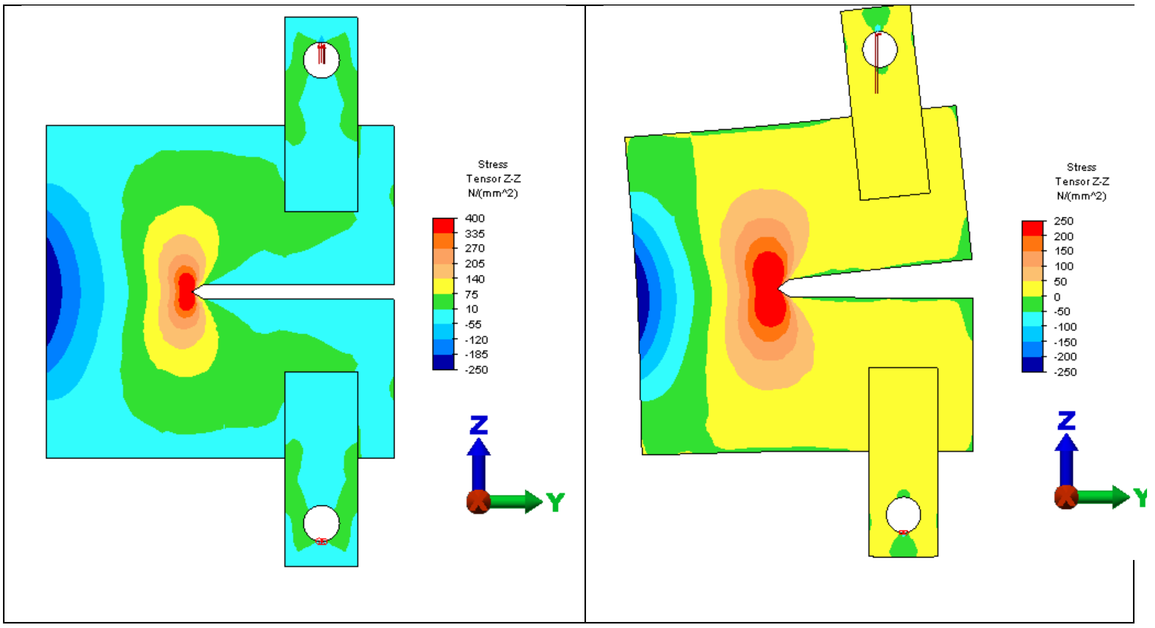

Fig A-1 Axial stress contours for isotropic titanium alloy Max defl = 0.45mm	**Fig A-2 Axial stress contours on deformed shape for Orthotropic Ti/SiC material. Max defl = 0.23mm (model name FTCRAN12)**
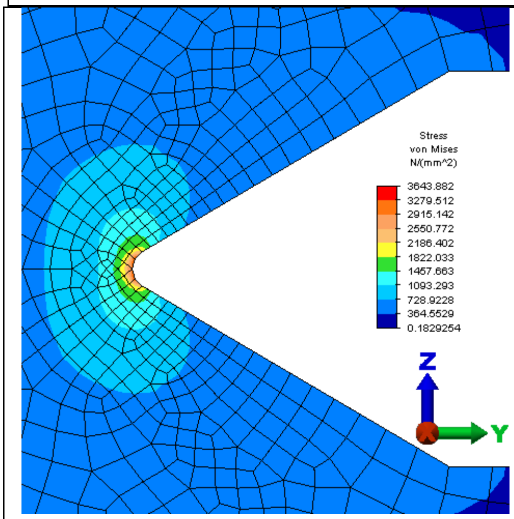	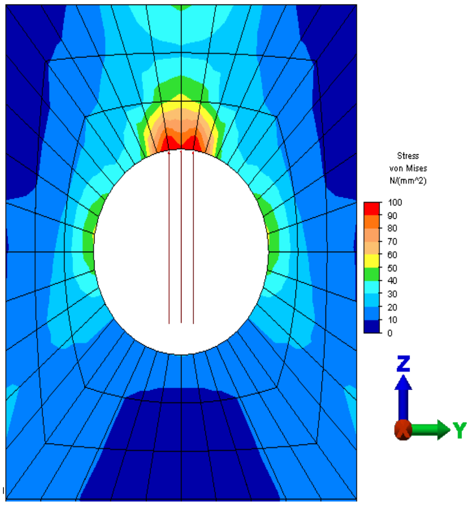
Fig A-3 Von Mises Stress contours at crack tip	**Fig A-4 Von Mises stress contours at pin hole**

A.2 Buckling Analysis

The 3D stress analysis model was used for the buckling analysis which calculates the critical buckling load factor for the first 10 modes. In this analysis the applied load was 400N and the results and deformed shapes are shown in Tab A-1. The left Figs of the table shows the fracture toughness test specimen with no guides or supports to control/prevent buckling. It shows that in the first buckling mode, the top and the bottom half of the specimen twisted with respect to each other at a load factor of only 0.69. Buckling occurred below the expected load. In the next mode the thin plate buckles at a load factor of 1.61 due to the compressive stress in the vertical section as shown in Fig A-1 & Fig A-2. This is also likely to occur when testing on homogenous titanium alloy specimens, since the expected load may about double that analysed. The third mode was a combination of the above two modes. Note that in the FEA model here the applied load is free to move as the plate buckles but in practice there will be a small restraining force applied as the load path is moved during buckling, which may offer some resistance to the first buckling mode.

Clearly this buckling issue is not acceptable and must be prevented by additional guides. A simple way to prevent the buckling is to support the vertical section of the specimen as shown in Fig A-5, the red circles indicate support from guide plates either side of the vertical section and extending over a length of 18mm. This length gives support to the lower buckling modes but still allows the crack tip to be observed. The buckling analysis for this supported configuration shows that the first buckling mode is now increased to a critical buckling load of over 9 and that the next two buckling modes occur due to buckling of the top and bottom edges of the sample but at load factors of 18 and 25 respectively.

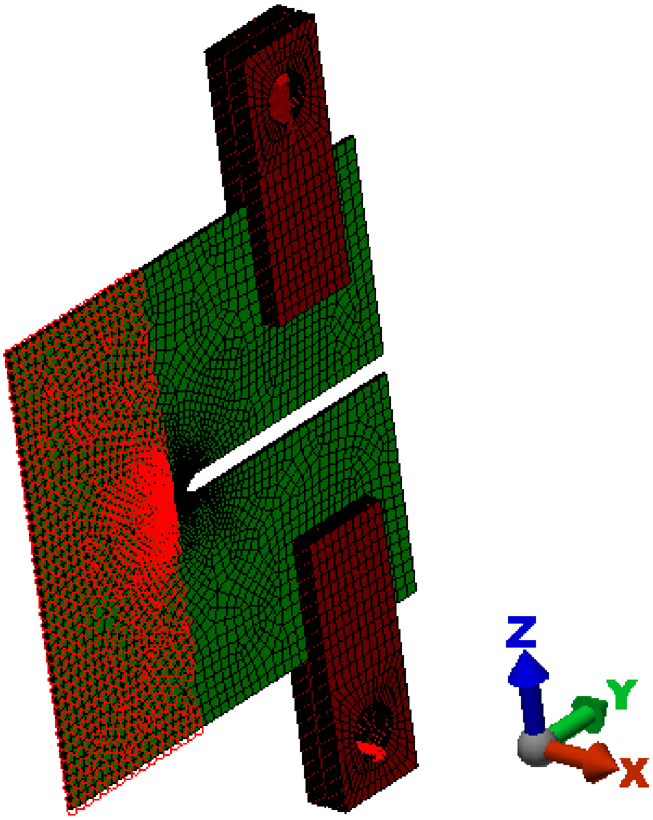

Fig A-5 Vertical section of sample is guided to prevent low buckling modes (FTCRAN14)

Table A-1 Buckling modes and critical buckling factors

	Comments		Comments
Mode 1 F_{crit}=0.69 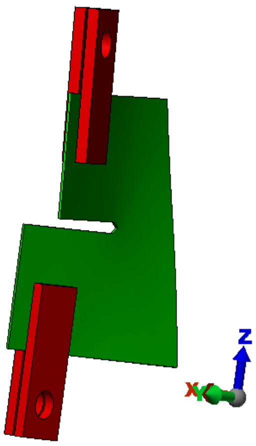 	Top and bottom half twist with respect to each other. This mode may be prevented by the attachments to some extent	Mode 1 F_{crit} = 9.19 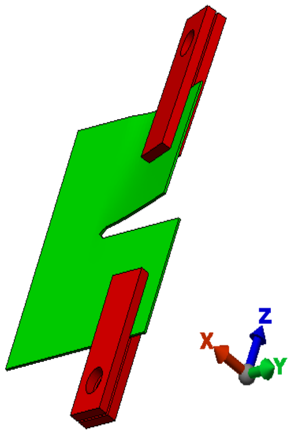 	Top and bottom twist.
Mode 2 F_{crit} =1.61 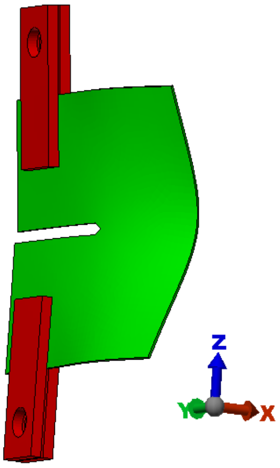 	Back section of specimen buckles due to compressive stress	Mode 2 F_{crit} =18.54 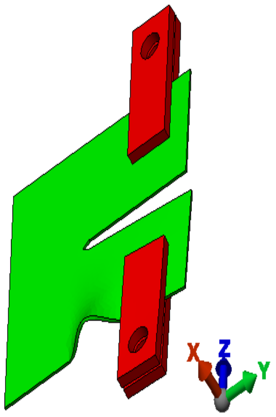 	Local edge buckling
Mode 3 F_{crit} =2.87 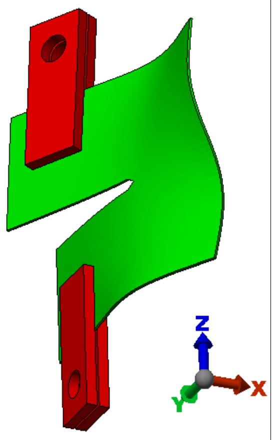 	Top and bottom half twist and back section buckles	Mode 3 F_{crit} =25.90 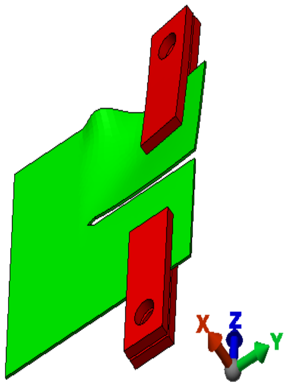 	Local edge buckling. Note this is not exactly the same as the previous mode due to different boundary conditions & loading

Orthotropic material props. No buckling supports (FTCRAN13)	Orthotropic material props. Buckling support dx=0 over 18mm (FTCRAN14)

A.3 Conclusion

The fracture toughness test specimens will require aluminium alloy tabs to be bonded to the top and bottom of the specimen on both sides to avoid the need for holes in the composite material which are likely to become damaged during loading.

The buckling analysis shows that the compressive stresses induced in the thin test sample will cause buckling failure below the expected loads needed for the fracture toughness testing.

If the vertical section of the sample is guided by fixed support plates over a length of about 18 mm then the buckling is suppressed sufficiently to allow the measurements to be made and so this guide will be required.

Appendix B -Crack plane identification

The system of crack plane identification described in this appendix shall be used in order to avoid ambiguous interpretation. Two-letter code was used to identify the crack plane [42]: the first letter defines the direction perpendicular to the crack plane; the second letter suggests the expected crack extension direction (see Fig B-1).

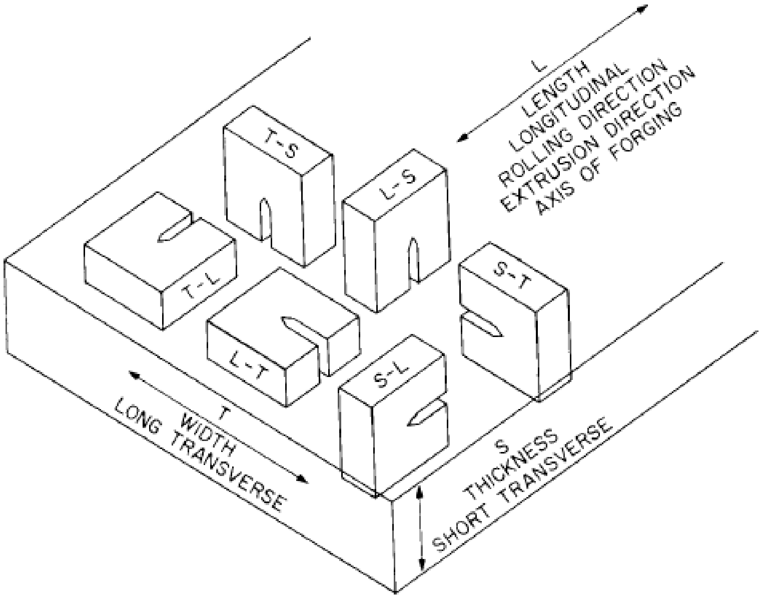

Fig B-1 Crack plane identification system [42]

Appendix C -Determination of $\mathrm{F_Q}$

This Appendix is used to determine the particular force $\mathrm{F_Q}$, which is used for the calculation of provisional plane-strain fracture toughness K_Q.

A line OF_d is drawn through the origin with a slope of 5% less than the tangent OA to the initial part of the record (see Fig C-1 [32]). The value of force F_Q is defined as follows: if there is a maximum force preceding F_d, and the force exceeds F_d, then this maximum force is F_Q, as shown in Fig 5-6 for the type Ⅰ and type Ⅱ； if the force at every point preceding F_d is lower than F_d, then F_d is F_Q, as shown in Fig C-1 for the typeⅢ.

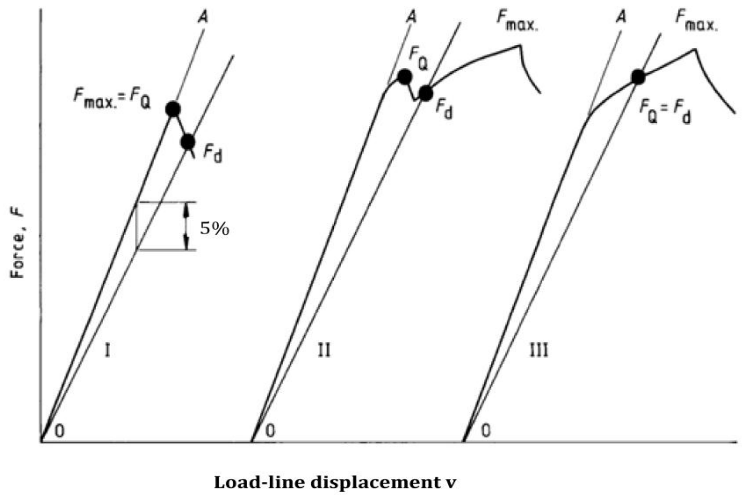

Note: the 5% offset slopes are exaggerated for clarity

Fig C-1 Definition of $\mathrm{F_Q}$ [32]

Appendix D -Determination of F, V_p and U_p

This Appendix is used to determine the onset of fracture force F, plastic displacement V_p and plastic area U_p, which are used for the calculation of critical crack tip opening displacement $CTOD_c$ and $\mathcal{J}_Q$.

In $CTOD_c$ testing, the value of F could be determined from force verse load-line displacement curve by the following methods, shown in Fig D-1:

(1) F is at the onset of unstable brittle crack extension or pop-in (see Fig D-1 ‘1’ and ‘2’).
(2) F is at the end of test for stable ductile crack extension (see Fig D-1 ‘3’)

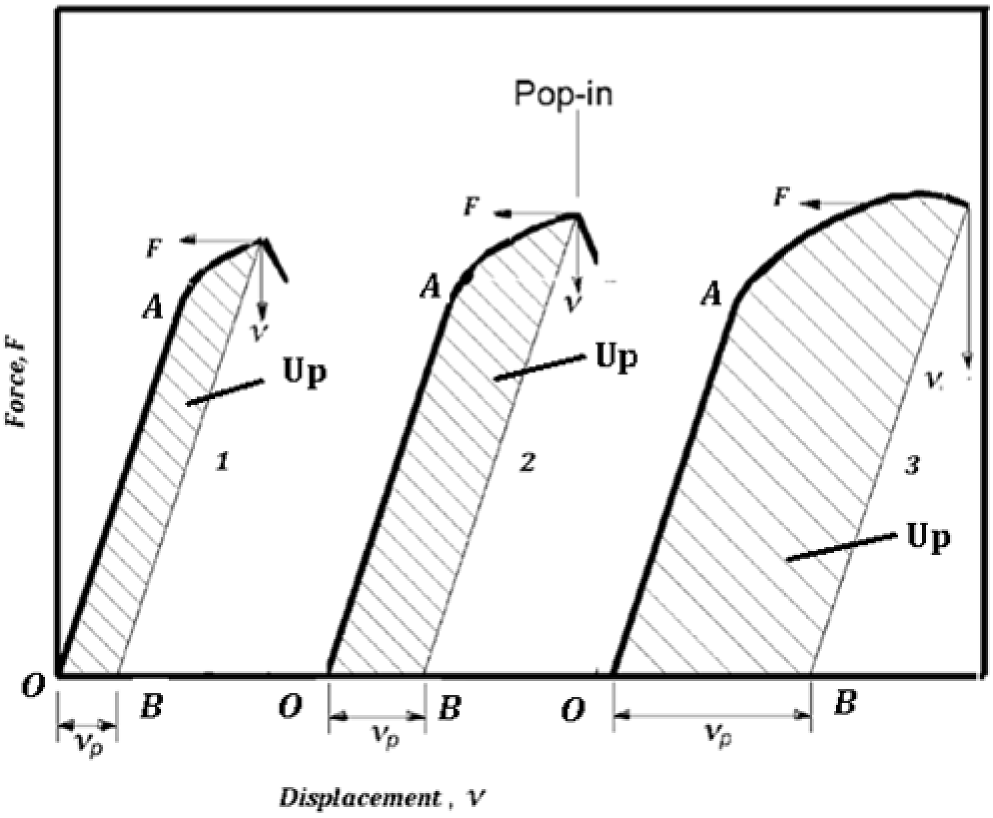

Fig D-1 Interpretation of force versus load-line displacement curve [32]

A line through the point of ‘F’ with the same slope as the tangent OA is drawn to the force versus load-line displacement curve [32], shown in Fig D-1, the length of OB was the plastic displacement V_p. The shadow area in Fig D-1 was the plastic component of the work done $\mathbf{U_p}$.

Appendix E –$\mathcal{J}$ Contour Integral

This Appendix illustrates a mathematical proof of the path independence of the $\mathcal{J}$ contour integral which was presented by Rice [45].

Fig E-1 shows $\mathcal{J}$ was evaluated along a closed contour $\mathcal{T}$

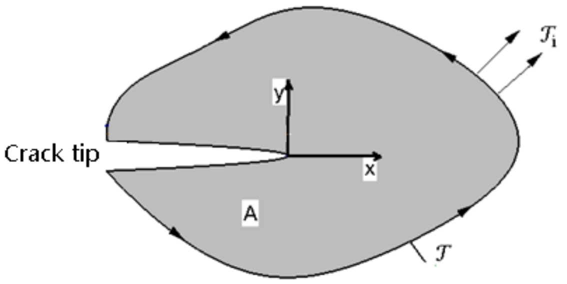

Fig E-1 A two-dimensional cracked body bounded by the contour $\mathcal{T}$

$$\mathcal{J} = \int_{\mathcal{T}} \left(\mathfrak{w}\, dy - \mathcal{T}_i \frac{\partial u_i}{\partial x}\, ds\right) \qquad [E\text{-}1]$$

Where:

$\mathfrak{w}$=strain energy density, $\mathfrak{w} = \int_0^{\varepsilon_{ij}} \sigma_{ij}\, d\varepsilon_{ij}$ [E-2], where, σ_{ij} and ε_{ij} are the stress and strain tensors;

$\mathcal{T}_i$ =components of the traction vector, $\mathcal{T}_i = \sigma_{ij} n_j$, where n_j are the components of the unit vector normal to $\mathcal{T}$.

u_i=displacement vector components

ds=length increment along the contour $\mathcal{T}$.

x, y=the coordinates defined in Fig E-1.

Rice converted the Equation E-1 into an area integral by invoking Green's theorem [45]:

$$\mathcal{J} = \int_{A} \left[\frac{\partial \mathfrak{w}}{\partial x} - \frac{\partial}{\partial x_j}\left(\sigma_{ij} \frac{\partial u_i}{\partial x}\right)\right] dxdy \qquad [E\text{-}3]$$

Where:

A is the area enclosed by contour $\mathcal{T}$;

By invoking Equation E-2, the first term in square brackets in Equation E-3 can be written as:

$$\frac{\partial \mathfrak{w}}{\partial \mathrm{x}} = \frac{\partial \mathfrak{w}}{\partial \varepsilon_{ij}} \frac{\partial \varepsilon_{ij}}{\partial \mathrm{x}} = \sigma_{ij} \frac{\partial \varepsilon_{ij}}{\partial \mathrm{x}} \qquad \text{[E-4]}$$

Applying the strain-displacement relationship (for small strains) to E. E-4 gives:

$$\frac{\partial \mathfrak{w}}{\partial \mathrm{x}} = \frac{1}{2} \sigma_{ij} \left[\frac{\partial}{\partial \mathrm{x}} \left(\frac{\partial u_i}{\partial x_j} \right) + \frac{\partial}{\partial \mathrm{x}} \left(\frac{\partial u_j}{\partial x_i} \right) \right] = \sigma_{ij} \frac{\partial}{\partial x_j} \left(\frac{\partial u_i}{\partial \mathrm{x}} \right) \quad \text{[E-5]} \quad \text{(since } \sigma_{ij} = \sigma_{ji} \text{)}$$

Invoking the equilibrium condition:

$$\frac{\partial \sigma_{ij}}{\partial x_i} = 0 \quad \text{[E-6]}$$

So,

$$\frac{\partial \mathfrak{w}}{\partial \mathrm{x}} = \sigma_{ij} \frac{\partial}{\partial x_j} \left(\frac{\partial u_i}{\partial \mathrm{x}} \right) = \frac{\partial}{\partial x_j} \left(\sigma_{ij} \frac{\partial u_i}{\partial \mathrm{x}} \right) \quad \text{[E-7]}$$

The first term in square brackets in Equation E-3 is identical to the second term. So, $\mathcal{J}$=0 for any closed contour.

Therefore, any arbitrary path around a crack will yield the same value of $\mathcal{J}$; $\mathcal{J}$ is path-independent.